Role of the Cochlear Nucleus Circuitry in Tinnitus and Hyperacusis

by

David T. Martel

A dissertation submitted in partial fulfillment
of the requirements for the degree of
Doctor of Philosophy
(Biomedical Engineering)
in the University of Michigan
2020

Doctoral Committee:

Professor Susan E. Shore, Chair
Professor Victoria Booth
Associate Professor Parag Patil
Assistant Professor Michael Roberts

David T. Martel

damartel@umich.edu

ORCID iD: 0000-0002-0165-6429

DEDICATION

This dissertation is dedicated to my Opa, Harry Hermann Blecker, PhD, a Professor Emeritus of Chemistry at the University of Michigan and continual source of inspiration in my life.

ACKNOWLEDGEMENTS

The studies carried out in this dissertation could not have been done without the help and support of many great people and funding organizations.

For Chapter Two, I thank Shaowen Bao for assisting with the development of the operant conditioning paradigm, Chris Ellinger and Dwayne Valliencourt for engineering assistance, Calvin Wu for technical and analytical assistance for single unit data, Liqin Zhang for assisting with behavioral data collection, and Michael Roberts for feedback and commentary on the manuscript.

For Chapter Three, I thank Calvin Wu for technical and analytical assistance and review of an earlier version of this manuscript, Adam Hockley and Mike Selesko for behavioral data collection and data analysis assistance, and Mr. Deepak Dileepkumar for technical support.

For Chapter Four, I thank Ray Meddis for providing code used in the model, Victoria Booth and Michael Roberts for insight and feedback on the modelling, Adam Hockley and Mike Selesko for behavioral data collection and data analysis suggestions, and Mr. Deepak Dileepkumar for technical support.

Studies in this dissertation were supported by funding from National Institutes of Health Grants R01-DC004825 (SES), RF1-MH114244-01 (SES), T32-DC00011 (DTM), the KHRI P30-DC05188, and the Wallace H. Coulter Translational Research Partnership.

PREFACE

Completing this dissertation has been the greatest accomplishment and rewarding challenge I have faced in my life thus far, and I am immensely grateful for the support I have received. My parents, Karen Blecker and Dr. Michael Martel, have been my biggest fans and supporters. Dr. Susan Shore, my advisor and soon to be business-partner, has been an amazing mentor. She has guided me to achieve more and improve myself more than I thought was possible. For that, I am forever grateful. Through lab, I met my fiancé and loving partner, Taylor Forrest. May we have many wonderful journeys together.

My utmost thanks go out to several utterly amazing people for starting me on this journey. To Dr. Erin Purcell, who first connected me to lab as a pre-medical undergraduate while taking her neural engineering course. My life would be radically different without the opportunities she arranged. Likewise, to Dr. Greg Basura, who first introduced me to Dr. Shore, and then again introduced me to Taylor; I am grateful for all you have done. To Dr. Seth Koehler, for showing me how an electrical engineer can do really-cool neuroscience research and solve real-world problems. Finally, to Dr. Calvin Wu, the pseudo-Mayor of Kresgeville, my one-time roommate and partner-in-shenanigans.

I especially would like to thank the rest of my thesis committee, Dr. Michael Roberts, Dr. Parag Patil and Dr. Victoria Booth, for your time and effort in making this dissertation happen.

It has been the greatest pleasure to connect with many talented scientists, who have provided me valuable professional advice and scientific insight. To Dr. Larry Roberts, for being a great researcher and greater friend. To Dr. Sandy Bledsoe, for asking insightful questions and providing a perfectionist's touch to proofreading. To Dr. Amarins Heeringa, Dr. Roxana Stefanescu, and Dr. Adam Hockley, for your help on tackling tough problems and making the lab atmosphere incredibly fun. To the audiologists, Dr. Kara Leyzac-Schwartz, Dr. Kendra Marks, Dr. Gerilyn Jones, Dr. Travis Riffle, Dr. Akshay Maggu and Dr. Jackie Kjolhede, for your skillful execution of our clinical trials and management of our tinnitus subjects.

As a student in the Shore lab, I have had the privilege to meet many pre-doctoral students. To my fellow graduate students, Thibaut Pardo-Garcia, Lorraine Horwitz and Liqin Zhang, I hope your projects and theses come to fruition. To the many incredibly talented undergraduates I have had the privilege of mentoring and working with, including Rebekah Weeks, Chris Chung, Daniel Xu, Emily Durie, Jake Katzman, and Michael West, I wish you the best of luck on your endeavors.

Finally, I thank the "unsung" heroes of academic research, the KHRI administrative staff, including Gary Dootz, Cassy Farvar, Sue Kelch, Diana Rausch, Jessica Odell, Debbie Stout, Jackie Blake, and Peggy VandeVoorde. Without your help and diligence, we would not be able to do what we do. I am grateful for the excellent technical and engineering support provided by Chris Ellinger, Dwayne Valliencourt, and Mr. Deepak Dileepkumar, without which none of our experiments would be possible. To the technicians that ran many of our experiments, including James Wiler, Mike Selesko, and Amber Clark, thank you for your hard work.

TABLE OF CONTENTS

LIST OF FIGURES

Figures

ABSTRACT

Tinnitus is the disorder of phantom sound perception, while hyperacusis is abnormally increased loudness growth. Tinnitus and hyperacusis are both associated with hearing loss, but hearing loss does not always occur with either condition, implicating central neural activity as the basis for each disorder. Furthermore, while tinnitus and hyperacusis can co-occur, either can occur exclusively, suggesting that separate pathological neural processes underlie each disorder.

Mounting evidence suggests that pathological neural activity in the cochlear nucleus, the first central nucleus in the auditory pathway, underpins hyperacusis and tinnitus. The cochlear nucleus is comprised of a ventral and dorsal subdivision, which have separate principal output neurons with distinct targets. Previous studies have shown that dorsal cochlear nucleus fusiform cells show tinnitus-related increases in spontaneous firing with minimal alterations to sound-evoked responses. In contrast, sound-evoked activity in ventral cochlear nucleus bushy cells is enhanced following noise-overexposure, putatively underlying hyperacusis. While the fusiform-cell contribution to tinnitus has been well characterized with behavioral and electrophysiological studies, the bushy-cell contribution to tinnitus or hyperacusis has been understudied.

This dissertation examines how pathological neural activity in cochlear nucleus circuitry relates to tinnitus and hyperacusis in the following three chapters.

In the first chapter, I characterize the development of a high-throughput tinnitus behavioral model, which combines and optimizes existing paradigms. With this model, I show that animals administered salicylate, a drug that reliably induces tinnitus at high doses in both humans and animals, show behavioral evidence of tinnitus in two separate behavioral tests. Moreover, in these same animals, I show that dorsal-cochlear-nucleus fusiform cells exhibit frequency-specific increases in spontaneous firing activity, consistent with the increased spontaneous firing observed in animal models of noise-induced tinnitus.

In the second chapter, I show that following noise-overexposure, ventral-cochlear-nucleus bushy cells demonstrate hyperacusis-like neural firing patterns, but not tinnitus-specific increases in spontaneous activity. I contrast the bushy-cell neural activity with established fusiform-cell neural signatures of tinnitus, to highlight the bushy-cell, but not fusiform-cell contribution to hyperacusis. These analyses suggest that tinnitus and hyperacusis likely arise from distinct neural substrates.

In the third chapter, I use computational modelling of the auditory periphery and bushy-cell circuitry to examine potential mechanisms that underlie hyperacusis-like neural firing patterns demonstrated in the second chapter. I then relate enhanced bushy-cell firing patterns to alterations in the auditory brainstem response, a sound-evoked electrical potential generated primarily by bushy cells. Findings in this chapter suggest that there are multiple hyperacusis subtypes, arising from separate mechanisms, which could be diagnosed through fine-tuned alterations to the auditory brainstem response.

CHAPTER I

Introduction and Background

Cochlear nucleus circuitry

The cochlear nucleus (CN) is the first nucleus in the auditory pathway and receives input from the cochlea via the auditory nerve (**Fig. 1.1**). The CN is divided into two principal sub-nuclei, the dorsal and ventral cochlear nuclei (DCN, VCN) (Osen, 1969). Fusiform cells are the principal-output neurons of the DCN, while the stellate cells and the bushy cells are the principal-output neurons of the VCN (Doucet and Ryugo, 2006). Two types of inhibitory interneurons provide inhibition to both the DCN and VCN principal output neurons (Nelken and Young, 1994). The glycinergic VCN d-stellate cell provides wideband inhibition to fusiform and bushy cells (Nelken and Young, 1994; Doucet et al., 1999; Arnott et al., 2004; Lomakin and Davis, 2008), while DCN vertical cells provide narrowband inhibition to fusiform and bushy cells (Young and Voigt, 1982; Wickesberg and Oertel, 1990; Doucet et al., 1999; Doucet and Ryugo, 2006; Campagnola and Manis, 2014).

In addition to auditory information, the CN receives glutamatergic, non-auditory input from multiple sources, including the somatosensory system (Itoh et al., 1987; Kanold and Young, 2001; Shore et al., 2003; Zhou and Shore, 2006). Fusiform cells receive somatosensory input indirectly, via granule cells on their apical dendrites (Osen

et al., 1995). Fusiform cells process multisensory input through the process of spike-timing-dependent plasticity, where the order and time interval between auditory and somatosensory input can alter cellular excitability *in vitro* and *in vivo* (Tzounopoulos et al., 2004; Koehler and Shore, 2013b). In contrast, bushy cells receive somatosensory input directly on their dendritic arbor (Zhou and Shore, 2004; Gomez-Nieto and Rubio, 2009, 2011), and these inputs can modulate bushy-cell firing (Heeringa et al., 2018b).

Neuroplastic changes in the cochlear nucleus underlie tinnitus and hyperacusis

Noise overexposure leading to cochlear damage can elicit homeostatic changes to neural circuitry at several levels of the auditory system, beginning in the CN (Bauer et al., 2008; Engineer et al., 2011; Kalappa et al., 2014a; Wu et al., 2016). Homeostatic increases in neural activity have been proposed to underlie tinnitus, or "ringing in the ears" (Shore et al., 2016b), which is generally characterized as a tonal sound or narrowly-tuned band of noise (Roberts et al., 2006; Roberts et al., 2010). Previous studies have shown that fusiform-cell plasticity is altered in animals with noise-overexposure induced tinnitus, reflecting a more excitable circuit (Koehler and Shore, 2013a). Fusiform cells exhibit narrowly-tuned increases in spontaneous firing rate (SFR) and cross-unit synchrony at frequencies associated with behavioral evidence of tinnitus (Wu et al., 2016), consistent with psychophysical measures of tinnitus.

Previous studies have shown that VCN bushy cells also exhibit increased SFR following cochlear damage (Bledsoe et al., 2009; Vogler et al., 2011). However, bushy cells show increased SFR across a wide range of best frequencies, including those not associated with the noise-overexposure spectrum. Moreover, putative bushy cells show

enhanced sound-evoked firing rates following noise-overexposure (Boettcher and Salvi, 1993). This discrepancy between bushy-cell neural patterns following noise-overexposure and the psychophysics of tinnitus suggest that bushy-cell firing is inconsistent with tinnitus. Instead, bushy-cell firing patterns following noise-overexposure appear more consistent with hyperacusis, an auditory disorder characterized by abnormal sound loudness growth (Baguley, 2003) that occurs across a wide frequency range (Tyler et al., 2014), including frequencies not associated with hearing-loss (Schecklmann et al., 2014; Sheldrake et al., 2015). However, no studies have directly analyzed bushy-cell firing following noise-overexposure and hyperacusis or tinnitus, nor assessed mechanisms underlying bushy-cells hyperexcitability.

In addition to their putative role in hyperacusis, bushy cells are major contributors to the auditory brainstem response (ABR), which is a sound-evoked, volume-conducted electrical potential arising from rapid-onset sounds (Melcher and Kiang, 1996; Dau et al., 2000). Rapid-onset sounds elicit highly synchronous activity originating in the auditory nerve, which is then transmitted up the auditory brainstem (Dau et al., 2000). The ABR waveform consists of five primary waves. The first wave (W1) arises from the auditory nerve, while bushy cells are the main contributor to waves 2 and 3 (W2, W3). The later waves (W4, W5) arise from higher centers in the brain that are driven by bushy cells. Bushy-cell excitability can be inferred by normalizing later wave amplitudes by W1 (Schaette and McAlpine, 2011; Gu et al., 2012). Enhanced bushy-cell excitability in tinnitus or hyperacusis could then be reflected through increased ABR wave amplitude ratios (e.g. W3:W1). Gu et al. (2012) demonstrated that humans with tinnitus show increased W3:W1 and W5:W1 amplitude ratios at high intensities, compared to

hearing-threshold-matched non-tinnitus controls. In a separate study, the same authors showed a greater prevalence of reduced sound level tolerance in tinnitus subjects compared to no-tinnitus controls, suggesting that the comorbidity of hyperacusis with tinnitus in the previous studies might explain the observed W5:W1 ratio increases (Gu et al., 2010). However, it is unclear how bushy-cells become hyperexcitable following noise-overexposure, and whether increases in bushy-cell excitability lead to ABR wave enhancements.

Investigating the role of cochlear nucleus circuitry in tinnitus and hyperacusis

In this dissertation, I have examined the role of altered cochlear-nucleus circuitry in the generation of tinnitus and hyperacusis through three studies. The first study, detailed in Chapter II, describes the development of a tinnitus-behavioral test using operant conditioning (Yang et al., 2011) along with a high-throughput variant of gap-prepulse inhibition of the acoustic startle (GPIAS) reflex test for tinnitus (Turner et al., 2006; Berger et al., 2013). To rapidly induce tinnitus to test the model, guinea pigs were administered salicylate, which induces tinnitus in high doses in humans and animals (Chen and Jastreboff, 1995; Yang et al., 2007; Turner and Parrish, 2008). Both behavioral tests independently diagnosed the same animals with tinnitus. In these same animals following salicylate administration, DCN-fusiform cells showed increases in spontaneous activity, cross-unit synchrony and altered stimulus-timing-dependent plasticity consistent with tinnitus-induction previously demonstrated using a noise-damage model (Koehler and Shore, 2013c; Wu et al., 2016; Marks et al., 2018).

The second study, detailed in Chapter III, assesses bushy-cell firing patterns following noise-overexposure and tinnitus/hyperacusis induction. I found that bushy cells exhibited hyperacusis-like neural firing patterns, consisting of increased firing rates at suprathreshold intensities across a wide range of frequencies compared to non-exposed control animals. Moreover, bushy cells exhibited wideband increases in SFR, consistent with other studies on bushy-cells following noise-overexposure (Bledsoe et al., 2009; Vogler et al., 2011) but inconsistent with the psychophysical characteristics of tinnitus (Roberts et al., 2006; Shore et al., 2016b). Interestingly, the finding that bushy cells showed hyperacusis-like neural firing patterns (with and without increases in SFR), suggested that multiple subtypes of hyperacusis might exist. In re-analyzing our existing data from DCN fusiform cells in animals with and without behavioral evidence of tinnitus (Wu et al., 2016), we found that fusiform cells did not exhibit neural firing patterns consistent with hyperacusis. Taken together, these findings suggest that hyperacusis and tinnitus may arise from separate neural substrates, where bushy cells putatively underlie hyperacusis, while fusiform cells underlie tinnitus and not hyperacusis.

In the third study, detailed in Chapter IV, computational models of the auditory periphery and bushy-cell circuitry (Brown et al., 2010; Clark et al., 2012) are utilized to examine several mechanisms contributing to bushy-cell hyperexcitability and thus putatively to hyperacusis. We find that multiple mechanisms, including glutamate-driven increases in excitability and glycine-driven reductions in inhibition, can explain neural firing patterns consistent with hyperacusis. However, no single mechanism alone can explain *in vivo* increases in sound-evoked activity with and without corresponding increases in SFR as demonstrated in Chapter III. Instead, both glutamate-driven

increases in excitability and reductions in glycine-driven inhibition are required. Moreover, each mechanism results in distinct alterations to the ABR, which could be used to differentially-diagnose putative hyperacusis subtypes.

Figure 1.1. Schematic of cochlear nucleus circuitry involved with tinnitus and hyperacusis. The cochlear nucleus is divided into two sub-nuclei, the dorsal and ventral cochlear nuclei (DCN, VCN). DCN principal output neurons, the fusiform cells (FC), receive auditory input on their basal dendrites (blue), non-auditory input on their apical dendrites (gold), and inhibitory input from narrowly-tuned vertical cells (dark red) and widely-tuned d-stellate cells (light red). In contrast, VCN output neurons, the bushy cells (BC), receive strong somatic input from the cochlea through endbulb-of-Held synapses, non-auditory input on their dendritic arbors, and inhibitory interneuron input from d-stellate and vertical cells. Following loss of input from the cochlea, FCs and BCs show homeostatic changes that appear to underlie tinnitus and hyperacusis, respectively.

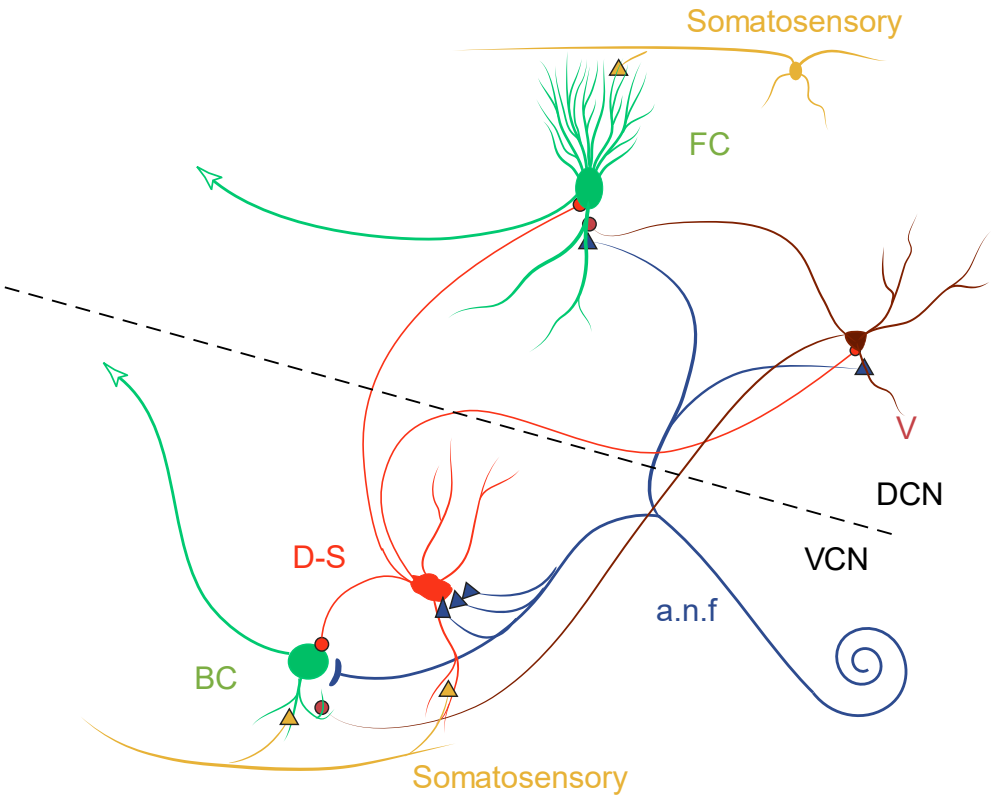

CHAPTER II

Dorsal Cochlear Nucleus Fusiform-Cell Plasticity is Altered in Salicylate-Induced Tinnitus

The study presented in this Chapter was co-first-authored with Thibaut Pardo-Garcia and published in Neuroscience (Martel et al., 2019).

Introduction

The mammalian dorsal cochlear nucleus (DCN) is a layered, cerebellar-like structure that receives input from both the cochlea and other sensory systems (Oertel and Young, 2004; Zhou and Shore, 2004). Fusiform cells, the principal output neurons of the DCN, receive input from the cochlea via auditory nerve fiber (ANF) synapses on their basal dendrites (Pfeiffer, 1966). In addition, fusiform cells receive somatosensory input via granule-cell axons, parallel-fibers (Mugnaini et al., 1980), which synapse on their apical dendrites (Ryugo et al., 2003; Haenggeli et al., 2005). This dendritic bipolarity allows fusiform cells to integrate somatosensory and auditory information for the processing of sound location and suppression of self-generated signals (Sutherland et al., 1998b; Sutherland et al., 1998a; May, 2000; Singla et al., 2017).

In vitro, fusiform cells exhibit spike-timing dependent plasticity (STDP) (Tzounopoulos et al., 2004): when EPSPs in parallel-fiber synapses are followed by

post-synaptic spikes in fusiform cells then long-term potentiation (LTP) occurs, while applying spike-eliciting stimulation to the basal dendrites that precedes parallel-fiber EPSP results in long-term depression (LTD). *In vivo* fusiform cells exhibit stimulus-timing-dependent plasticity (StDP) (Koehler and Shore, 2013b; Wu et al., 2015), the macroscopic equivalent of STDP in which LTP or LTD occurs depending on the order of auditory and somatosensory stimulation (Koehler and Shore, 2013b). *In vivo,* the apical dendrites of fusiform cells are activated through deep brain stimulation of somatosensory nuclei (Dehmel et al., 2012b; Koehler and Shore, 2013b), or transdermal activation of the face overlying the trigeminal ganglion or the neck overlying the C2 ganglion (Wu et al., 2015; Marks et al., 2018), while the basal dendritic synapses are activated with sound (Liberman, 1993). Thus, the combination of sound and somatosensory stimulation elicits StDP in fusiform cells (Koehler and Shore, 2013b; Wu et al., 2015).

Altered StDP has been demonstrated in animals with tinnitus, which show StDP timing-rule inversions, in which bimodal auditory-somatosensory stimuli that normally result in LTP now result in LTD, and those that would normally result in LTD, now result in LTP (Koehler and Shore, 2013c). StDP timing rules from animals with tinnitus also show enhancement, i.e. the timing rules show more bimodal time intervals eliciting LTP than LTD compared to exposed animals without evidence of tinnitus or non-exposed control animals with balanced LTP and LTD (Koehler and Shore, 2013c; Marks et al., 2018). Enhanced LTP biases the fusiform-cell firing rates toward excitation, contributing to increased SFR, increased bursting and increased pairwise synchrony, the physiological hallmarks of tinnitus (Wu et al., 2016; Marks et al., 2018).

While noise-induced tinnitus is the most common form of tinnitus in humans (Shore et al., 2016b), tinnitus can also be temporarily induced in humans through the acute administrations of high doses of aspirin (Sheppard et al., 2014). In many different species and behavioral models, administration of the active ingredient in aspirin, sodium salicylate, leads to tinnitus (Jastreboff et al., 1988; Bauer et al., 1999; Guitton et al., 2003; Ruttiger et al., 2003; Yang et al., 2007; Turner and Parrish, 2008). However, the mechanisms through which salicylate induced tinnitus occurs are not well understood and appear to be multifactorial. In the present study, we hypothesized that guinea pigs with salicylate-induced tinnitus would show inversions of fusiform-cell StDP timing rules as well as increases in fusiform-cell SFR and synchrony like those previously demonstrated with noise overexposure (Koehler and Shore, 2013c; Wu et al., 2016; Marks et al., 2018). Consistent with our hypotheses, animals with behavioral evidence of tinnitus assessed with GPIAS and operant conditioning, following salicylate administration, demonstrated tinnitus-frequency-specific StDP timing-rule enhancements. In addition, we also observed increased SFR and enhanced pairwise unit synchrony between fusiform cells. These findings highlight similarities in mechanisms of action in noise-induced and salicylate-induced tinnitus and suggest maladaptive timing-dependent plasticity is a necessary ingredient for tinnitus induction. Moreover, we demonstrated for the first time in guinea pigs, that animals administered salicylate show behavioral evidence of tinnitus with two independent behavioral assessments. The cross-validation of GPIAS and operant conditioning with a reliable tinnitus-induction process furthers our understanding of tinnitus by highlighting the

reliability of the behavioral paradigms, upon which further discoveries are made possible.

Methods

Ethical Treatment of Animals

All animal procedures were performed in accordance with protocols established by the National Institutes of Health (Publication 80-23) and approved by the University of Michigan Institutional Animal Care and Use Committee (IACUC). Seven juvenile female, pigmented guinea pigs were obtained from the University of Michigan colony at 2-3 weeks of age.

Experimental Design

Guinea pigs were tested for tinnitus using two behavioral paradigms (**Fig 2.1A**): GPIAS (**Fig 2.1B**), and a custom developed operant conditioning technique (**Fig 2.1C, D**). Baseline GPIAS results were collected for six experiment days (2 days per week, for three weeks), following which animals were administered salicylate for an additional six experiment days. After GPIAS testing, animals underwent the operant conditioning procedure. Learning rates were assessed until animals correctly demonstrated 65% success rates (between 2-6 experiment days) or were removed from further study if they failed to learn. Baseline crossing rates were measured for six experiment days. Saline then salicylate testing periods were also measured for six experiment days. Following behavioral assessments, DCN electrophysiology was assessed (**Fig 2.1E**). DCN was surgically accessed (**Fig 2.1F**), fusiform cells identified, and their activity

recorded with multichannel electrodes (**Fig 2.1G, H**). STDP learning rules, SFR, synchrony and ABRs were measured pre- and post-salicylate administration. At the end of the experiment, animals were killed by intraperitoneal injection of sodium pentobarbital (SomnaSol, 1mL) and decapitation.

Gap-prepulse inhibition of the acoustic startle (GPIAS).

Animals startle in the presence of a rapid-onset sound (the startle pulse), while the presentation of a stimulus (detectable above a background noise) before the startle pulse will reduce the resultant startle amplitude. Similarly, a gap placed in the background noise before the startle pulse will decrease the startle amplitude. Tinnitus that is spectrally similar to the background noise is thought to impair detection of the gap (**Fig 2.1B**) (Turner et al., 2006).

The guinea pig's pinna-reflex displacement was measured in response to the startle pulse (Berger et al., 2013). Pinna tips were marked with non-toxic, water-soluble green paint, manually applied by trained investigators. Green pixels were identified using a custom-written k-nearest neighbors classifier algorithm (Mathworks MATLAB) (Friedman, 1977; Altman, 1992). Frames where green points constituted less than 0.01% of pixels were excluded, as this indicated the animal's ears were not located in the frame. Pinna locations were identified by clustering green pixels and computing the centroids of a two-dimensional Gaussian mixture model (McLachlan and Chang, 2004). The Euclidean distance between (X^{ear} (t), Y^{ear} (t)) points was computed over the trial duration. Startle amplitudes were computed by fitting the Euclidean distance to a

Gaussian-windowed sine-wave cycle and computed as the resultant amplitude parameter.

To assess tinnitus, gaps in constant background noise (65 dB SPL; 50 ms with 5 ms rise/fall times) were presented 100 ms before a broadband noise startle pulse (90 dB SPL; 20 ms with 2 ms rise/fall times). At a given background frequency band (center frequencies of 9, 13, 17 kHz with 2 kHz bandwidths, or Gaussian broadband noise), a randomized series of 10 pre-pulse (either a gap of silence, or a pre-pulse of noise at 75 dB SPL) and 10 no-prepulse sounds were delivered. All testing was performed in sound-proof booths (Acoustic Systems, Inc), with greater than 100 dB acoustic isolation between testing chambers. Trials were randomly presented every 20 to 30 seconds, with prepulse and no-prepulse trials combined into a single per-frequency testing session, and randomly interleaved. Each per-frequency testing session lasted approximately 10 minutes due to random variation of intertrial intervals. Eight testing sessions (one gap and one prepulse noise testing session for each frequency band) were performed each testing day, for an average testing time of approximately 80 minutes. Animals were not kept in their restraints for more than two hours. Testing occurred twice per week, with at least two non-testing days in between each testing day (Mondays and Thursdays or Tuesdays and Fridays) to prevent habituation for a total of six experimental days. Per-background frequency testing session results were pooled over three weeks. Startle amplitudes greater than two standard deviations above the mean were identified and excluded. In each frequency band, a normalized startle ratio (R) was computed as the mean with pre-pulse conditions normalized by the mean without pre-pulse values. Tinnitus was assessed by measuring the amplitude of the

startle reflex at baseline (blue) and after salicylate treatment (red). An animal was defined as having tinnitus if, at a given frequency, the mean of the post-exposure distribution was significantly greater than the mean of the pre-exposure distribution (two-sample t-test; alpha = 0.05). The changes in gap *R* values from pre- to post-exposure were quantified by the standardized tinnitus index [$(x - \mu)/\sigma$] (Kalappa et al., 2014b), where x is the post-exposure gap *R* value, μ and σ are the mean and standard deviation of pre-exposure gap *R* value. A larger positive index indicates more impaired gap detection ("more tinnitus").

Operant Conditioning Paradigm

We modified operant conditioning tests previously developed for rats (Ruttiger et al., 2003; Yang et al., 2011) for use in guinea pigs. Guinea pigs are notoriously difficult to train through positive reinforcement. To increase learning rates, fear conditioning was used. Further, light-dark preference testing was not used as guinea pigs are generally non-responsive to classical operant conditioning paradigms (Anderson and Wedenberg, 1965; Crifo and Antonelli, 1972).

Seven guinea pigs were recruited for training. All operant behavioral testing was conducted in a double-walled soundproof booth (Acoustic Systems, Inc). These animals were trained to cross a custom-built operant chamber in response to sounds (**Fig 2.1C**). There were no distinguishing features on either side of the chamber (**Fig 2.1D**). The midpoint of the chamber was computed digitally, and dynamically switched from 35% away from the left side of the box to 65% away from the left on crossing, ensuring that an animal had to completely cross the box to advance the protocol. Animals were

tracked using custom-written MATLAB software and high-speed cameras (Point Grey, Inc). A single tracking camera was placed over the midline and two speakers (Pyle Wave PLX32 4 ohm speakers; Parasound Zamp Zone Amplifier) were fixed into the chamber ceiling two feet above the animal. The speakers were positioned in between the midline and the nearest side of the chamber. The system transfer function was measured using a ¼" microphone (B&K 4136 and Stanford Research Systems SR760 spectrum analyzer) and flattened in FFT space from 4 kHz to 30 kHz with custom written software. The sound field at the bottom of the chamber varied by 2 dB but was symmetric across the midline.

For each trial, the animal was required to remain still for a randomly-determined holding period (uniformly distributed from 5-45 seconds) followed immediately by a sound (2 kHz noise band with center frequencies at 8, 10, 12, 14, 16 kHz, or carriers as tones for 12 unique sounds; intensity range: 40-90 dBSPL in 10 dB steps for 6 unique intensities). Each sound- intensity pair was presented once for 72 trials per testing session, with ordering randomized per testing session. The animal had 30 seconds to cross from one side of the box to the other before electrical shocks were presented if the animal failed to cross in time (I = 1.25 mA; Med Associates ENV-414S with custom built Arduino controller; applied to front and hind paws by custom built electrode grid). Shocks were applied uniformly across the entire grid, for at most one minute after a failed trial to prevent harm to the animal. However, if the animal crossed before the end of sound presentation, the trial was considered a success and the next trial was immediately started. The non-learning animals demonstrating "freezing" behavior, where no electrical stimulus could elicit crossing. These animals were removed after

two weeks of testing. Four out of the seven guinea pigs successfully learned the operant conditioning.

After each animal achieved a success crossing rate of 65%, probe trials were introduced. Ten punishment-free silence probe trials were randomly interspersed with regular trials, with a duration of 2 minutes each. The average number of crossings per silence period was normalized by the average number of successful crossings to control for differences in animal learning and locomotion, as previous studies have shown this measure is independent of motor impairments, auditory masking and hearing loss (Ruttiger et al., 2003; Tan et al., 2007). An animal was defined as tinnitus-positive if its probe trial crossing rate during silence trials post-induction was greater than the baseline rate (Chi-square test of proportions; alpha = 0.05).

Tinnitus Induction

To induce tinnitus, animals received a daily dose of sodium salicylate dissolved in saline (intraperitoneal 300 mg/kg; concentration: 250 mg/mL, solution provided and used as-is by *Racehorse Meds*) (Norena et al., 2010), which reliably and rapidly induces tinnitus (Jastreboff et al., 1988). An equivalent volume of 0.9% saline was administered as a control. Behavioral and physiological assessments of tinnitus commenced within thirty minutes of injection and were completed within three hours, corresponding to the peak effect of salicylate (Norena et al., 2010). This duration provided adequate time to complete all behavioral tests as well as electrophysiology: GPIAS testing sessions lasted no more than two hours, operant conditioning sessions 1 hour, and electrophysiology recordings 2 hours.

Auditory Brainstem Responses

All electrophysiology testing occurred in a double-walled, soundproof booth (Acoustic Systems, Inc). Animals were anesthetized and auditory brainstem responses (ABRs) were measured pre-baseline and 30 minutes post-salicylate administration (**Fig 2.1A, E**) (tone pip, 1024 repetitions, 5ms duration, 0.5 ms rise/fall time, cos^2 gating; 8, 12, 16, 20, 24 kHz; TDT RX8 DAC, HB7 amplifier, and PA-5 attenuator). Sounds were presented close-field (DT770 Speaker) and were coupled to the ear through custom-built hollow ear bars. Calibration was performed using TDT SigCalRP and a ¼" microphone (B&K 4136 and Stanford Research Systems SR760 spectrum analyzer; RX8 and PA5). The system transfer function was flattened in FFT space from 200 Hz-32 kHz. Stainless steel needle electrodes were placed into the skin overlying the bullae and at vertex. Evoked potentials were digitized and filtered (TDT RA4LI headstage; PZ2-64 pre-amp; filtered between 300 Hz-3 kHz with a 60 Hz notch). Sound intensities were presented starting at 90 dB SPL and decreased in 10 dB steps to 0 dB SPL. Thresholds were identified by a trained experimenter as documented previously (Dehmel et al., 2012a). Threshold was defined as the one-step greater than lowest sound pressure level that did not elicit ABRs with at least three identifiable peaks and troughs.

Surgery

After ketamine/xylazine (40:10 mg/kg) anesthesia, animals were held in a Kopf stereotaxic frame with hollow ear bars. Fur overlying the head and neck was removed (while ensuring that whiskers were not affected) by clippers. Skin was cleaned with an alcohol wipe. Body temperature was kept constant (38 degree C) throughout the experiment by a custom-built heating pad with closed-loop controller. The state of the animal was checked, and supplemental anesthesia (0.15 mg of same ketamine/xylazine dose) was administered every 30 minutes by the experimenter. Tissue overlying the occipital ridge was removed without impacting the ear muscles, and a craniotomy and duratomy performed to expose the cerebellum. Surgical manipulations were performed consistently across all animals, and are similar to previous experiments performed in this lab (Dehmel et al., 2012b; Koehler and Shore, 2013c; Basura et al., 2015; Stefanescu et al., 2015; Wu et al., 2016; Marks et al., 2018).

Single Unit Electrophysiology

Multichannel recording electrodes (Neuronexus; 32 channels with 16 channels per 2 shanks; custom headstage) were used to record *in vivo* neural responses (**Fig 2.1F**). Voltages from each electrode site were digitized (PZ2-64 pre-amp) and bandpass filtered (300 Hz-3 kHz, with a 60 Hz and harmonic comb-filter). Spikes were identified when voltage amplitude crossed 2 standard deviations above the mean voltage arising from spontaneous activity. The fusiform cell layer was consistently found when the electrode was placed 25 degrees off the vertical, 3-4 mm lateral to the midline and 3-4 mm posterior to earbar zero, and from 5-6 mm ventral to the surface of the cerebellum. Units were identified using 65 dB SPL broadband search stimuli. Unit thresholds were

stable throughout the experiment. Fusiform cells were identified by their build-up and pause-build-up peri-stimulus time histograms (PSTH) and locations within the DCN (Stabler et al., 1996) (**Fig 2.1G**). Once a set of fusiform cells was identified, the electrode was not moved until the end of the experiment. Unit consistency was maintained by clustering all waveform PCA coefficients throughout the experiment. Neural spike data was imported into MATLAB and analyzed offline. Spike waveforms were projected into principle component space and clustered by the first three coefficients by a trained user. Timestamps were grouped by cluster into isolated units, and spiketrains constructed in MATLAB.

StDP Induction

StDP was elicited by applying non-invasive transdermal electrical stimulation (Rhythymlink Ag/AgCl electrodes; custom-built linear isolated current source; biphasic square wave; 100 us/phase, 1 kHz, 3 pulses) briefly before or after tone bursts (50 ms duration, 2 ms rise and fall times, Cos^2-ramps) 40 dB above unit threshold (SL) at a neuron's best frequency (Wu et al., 2015; Marks et al., 2018) (**Fig 2.1F, H**). Electrodes were applied to the skin after ABRs but before surgery. Current level was determined as 0.1 mA less than the level that elicited muscle contractions. Source electrodes were placed on the skin over the C2 dorsal ganglion, while sink electrodes were placed lateral to the spinal column. Timing rules were measured as the percent change in firing rate from pre- to post-pairing (Wu et al., 2015; Marks et al., 2018). Each bimodal interval recording session lasted 15 minutes, with six recordings per experimental condition for

a total of 90 minutes trial time. Two recording sessions were performed in the same experiment, without moving the electrode in-between sessions (Baseline, Salicylate).

Synchrony Analysis

Spontaneous activity (at least 150 seconds) was recorded prior to starting each STDP recording session. SFR was computed as the average spike rate during this trial. Cross-unit spatial synchrony was computed using cross-correlograms (Voigt and Young, 1990; Norena and Eggermont, 2003; Wu et al., 2016; Marks et al., 2018). Spikes co-occurring within 150 μs were removed. Cross-correlation coefficients ($p(\tau)$) were computed as a function of time lag for each pairwise combination of spike trains (Eq. 1).

$$p(\tau) = \frac{R_{AB}(\tau) - E}{\sqrt{N_A N_B}},\ E = \frac{N_A N_B}{n} \qquad (1\text{–}2)$$

$R_{AB}(\tau)$ is the unbiased cross-correlation of spike trains *A* and *B*; N_A and N_B indicate spike counts in the respective spike trains. *E* is the mean probability of coincident firing for Poisson-distributed data (Eq. 2), defined by the multiplication of N_A and N_B over the number of bins (*n*). Bin size was constant at 0.3 ms (Voigt and Young, 1990). A unit-pair was considered synchronous when the peak *p* value was greater than ±4 standard deviations from the mean $p(\tau)$.

Data Analysis

Linear correlations were computed using Pearson's linear correlation. Distribution differences were assessed for significance with ANOVAs or Kruskal-Wallis tests where appropriate (alpha = 0.05). Chi-square test of proportions was used to assess tinnitus status for the operant paradigm (alpha = 0.05).

Results

GPIAS and operant conditioning diagnose salicylate-induced tinnitus in guinea pigs

To first assess animals for tinnitus, we utilized a modified variant of the GPIAS paradigm, tracking an animal's pinna-tip, or Preyer's, reflex instead of a whole body amplitude startle (Berger et al., 2013) (**Fig 2.1B**)**. Fig. 2.2A** shows an example animal positive for tinnitus at 12-14 kHz and 16-18 kHz, but not at 8-10 kHz or broadband noise (BBN). For each animal, tinnitus strength was quantified through the tinnitus index (TI). Animals that completed both behavioral paradigms and data were recorded from (n=4/7) demonstrated evidence of tinnitus in at least one frequency band, but no animals showed evidence of broadband noise tinnitus (**Fig 2.2B**)**.** The animals demonstrated a high-frequency tinnitus, with the peak of the average tinnitus spectrum occurring at 12 kHz and consistent with other studies utilizing GPIAS to assess salicylate-induced tinnitus (Yang et al., 2007; Ralli et al., 2010). The mean TI was significantly greater within tinnitus frequency bands than outside tinnitus frequency bands (p=7.142e-4; two-sample t-test) (**Fig 2.2C**). Animals demonstrated tinnitus-positive TIs with a similar range and variance (current study: min=0.31, max=1.21, st.dev.=0.32) compared to animals tested in Marks et al. (2018) (min=0.33, max=2.01,

st.dev.=0.46). Further, the current TI distributions and the TI distributions from Marks et al. (2018) were not significantly different (two-way ANOVA, P=0.476).

To validate the presence of tinnitus, we modified operant conditioning procedures previously developed for use in rats. Guinea pigs were trained to cross from one side of the operant box to the other in the presence of sound, while remaining on the original side when no sound was present (**Fig 2.1C, D**). Four animals successfully demonstrated crossing rates greater than 65% within six experiment days (**Fig 2.3A**). Next, we presented silence trials interspersed with sound trials, and measured the animal's baseline crossing rate (**Fig 2.3B**). To control for differences in baseline locomotion for each animal, crossing rates in silence were normalized by the animal's crossing rate during sound, as previous studies have shown that normalization corrects for differences in mobility and learning rate (Ruttiger et al., 2003). Finally, we administered salicylate to the animals, and measured the crossing rate again. Intraperitoneal administration of salicylate (300 mg/kg) significantly increased the normalized crossing rate when compared to baseline or equivolume saline time points (**Fig 2.3B**) (p=5.03e-4, n=4 animals, Chi-Square test of proportions).

Animals with salicylate-induced tinnitus have increased SFR, synchrony and altered StDP timing rules in DCN fusiform cells.

Fusiform cells show increased SFR, increased synchrony and altered StDP timing rules following noise-overexposure induced tinnitus (Koehler and Shore, 2013c; Wu et al., 2016; Marks et al., 2018). In the present study, we wanted to explore the

possibility that the mechanisms by which salicylate induced tinnitus are like those of noise-overexposure-induced tinnitus. We measured the electrophysiological activity in animals that had been positively screened using GPIAS and operant conditioning tests (**Figs 2.1-2.3**). Prior to surgery, transdermal electrodes were placed ipsilateral to the neck region overlying the C2 dorsal root ganglion (**Fig. 2.1F**). Multichannel single-unit electrodes were stereotaxically implanted into the DCN of anesthetized guinea pigs (**Fig. 2.1F-H**). Fusiform cells were identified by their characteristic build-up and pause build-up PSTH, receptive fields and coordinates within the DCN (Stabler et al., 1996) (**Fig 2.1G**). Once stable fusiform cell responses were identified, electrodes were not moved throughout the remainder of the experiment. Units were found with BFs ranging from 2 kHz to 24 kHz, with a preponderance of units located between 6 kHz and 18 kHz (**Fig 2.4A**). Fusiform cells with BFs in a GPIAS carrier band showing evidence of tinnitus constituted 53.15% of recorded units, while fusiform cells with BFs outside tinnitus bands constituted 46.85% of units (**Fig. 2.4A**). Auditory brainstem responses (ABRs) indicate threshold shifts of approximately 10 dB after salicylate administration at frequencies at and above 12 kHz (**Fig 2.4B**), consistent with previous studies (Stolzberg et al., 2012).

Fusiform cell spontaneous activity was recorded before (blue) and after (red) intraperitoneal administration of salicylate (**Fig. 2.4C**). After salicylate administration, fusiform-cell SFR was increased significantly across animals when compared to baseline (ANOVA, p=1.79e-11, n=199; **Fig. 2.4C**). Increases in SFR were most pronounced in the 8-16 kHz regions, corresponding to frequencies with GPIAS-based evidence of tinnitus (purple tinnitus spectrum in **Fig. 2.4D**). Furthermore, cross-unit

synchrony was significantly increased over the geometric mean BF between sampled units (two-way ANOVA, p=7.26e-89, n=4404) (**Fig. 2.4E**). Importantly, salicylate administration significantly increased the correlation between SFR and synchrony (r-baseline=0.13; r-salicylate=0.38; Pearson's linear correlation), consistent with previous studies (Wu et al., 2016; Marks et al., 2018) (**Fig. 2.4F**).

To induce StDP in the fusiform cells (**Fig. 2.1H**), transdermal Ag/AgCl electrodes were placed on the skin overlying the C2 ganglion (Wu et al., 2015; Marks et al., 2018). These electrodes were not moved during the experiment. StDP timing rules were assessed using bimodal stimulation with variable auditory (orange sinewave in **Fig. 2.1H**) -somatosensory (blue pulse in **Fig. 2.1H**) stimulus intervals. Timing rules were assessed as previously described (Wu et al., 2015; Marks et al., 2018). At baseline, the guinea pigs exhibited StDP timing rules consistent with those obtained from non-tinnitus animals in previous studies (Blue line in **Fig. 2.5A**) (Wu et al., 2015; Marks et al., 2018). Post-salicylate administration, StDP timing rules were significantly enhanced and inverted compared to baseline (ANOVA, p=0.0036, n=199) (**Fig. 2.5A**). Interestingly, partitioning timing rules into groups based on whether the unit BF was in a tinnitus-band or not revealed a divergence in learning rule enhancement or suppression. Timing rules in a GPIAS-measured tinnitus band exhibited predominantly LTP, while those outside the tinnitus band exhibited LTD (**Fig. 2.5B**).

Figures

Figure 2.1. Experimental Design and Timeline. A) Animals were tested for tinnitus baseline using the adapted GPIAS paradigm (see METHODS) 6 days (Mon/Thurs, or Tue/Fri for three weeks) and with salicylate for 6 days. Following GPIAS, animals were trained to move when a sound was presented (2-6 days; Mon/Wed/Fri). Animals that successfully learned to cross the chamber in response to a sound underwent 6 days of baseline testing, followed by administration of saline and then salicylate, each for 6 days. After operant conditioning, DCN electrophysiology was performed. **B)** Tinnitus impairs gap-prepulse inhibition when spectrally like a background carrier band. Guinea pig pinna tips were painted green, tracked using high speed cameras and the pinna-startle displacement computed. **C)** If guinea pigs crossed the midline when a sound was introduced, no shock was given (Green). If they failed to cross the midline during a sound (Red), the guinea pig received a footshock until it crossed the midline (Yellow). **D)** Sample frame, with the adaptive midline (vertical red line) and guinea pig location (green, with red star on centroid). **E)** ABRs were recorded (20 min) followed by single unit recordings to identify DCN fusiform cells (30 min) and record spontaneous firing rates (SFR) and STDP learning rules (LR) (~90 min). Salicylate was then injected (i.p.), After 30 min, ABRs and single unit recordings were repeated. **F)** Schematic of multichannel recording electrode placements in the DCN and Ag/AgCl stimulating electrodes placement over the C2 DRG region for STDP evaluation. **G)** Fusiform cells were identified by their receptive fields and temporal response patterns (inset), and stereotaxic location within the DCN (See methods for coordinates). **H)** Somatosensory (Blue square waves) and auditory (yellow sine waves) stimulation was applied to assess StDP and quantified by learning rules (boxed inset).

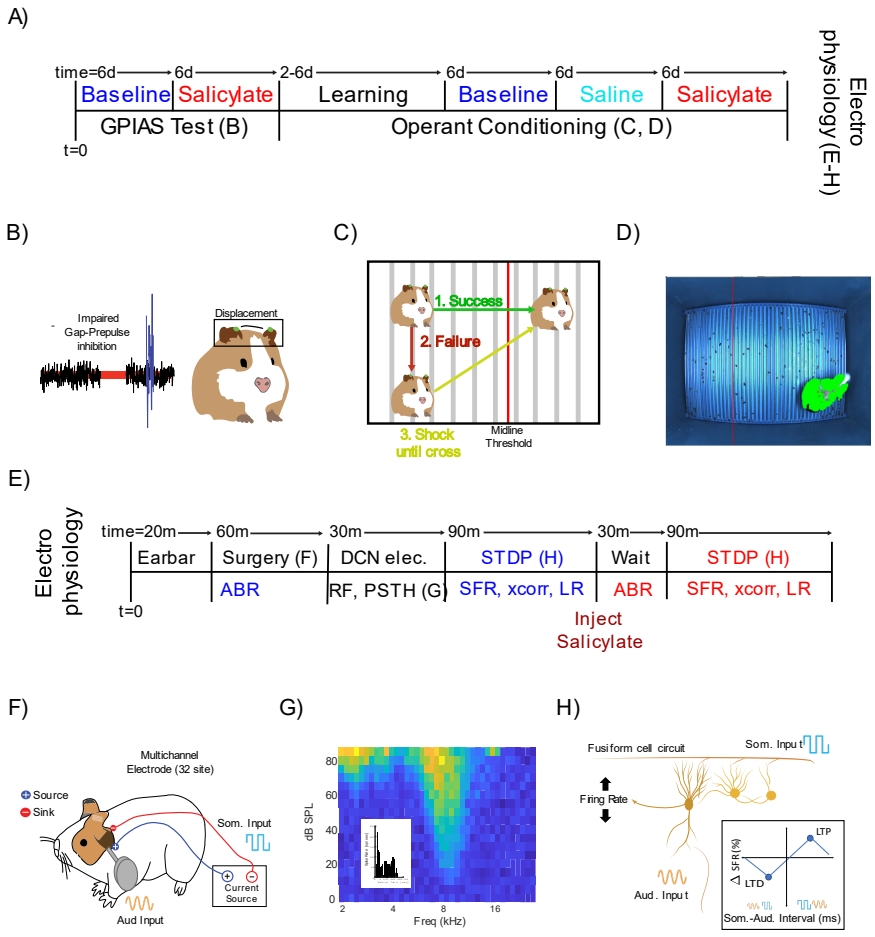

Figure 2.2. GPIAS identifies guinea pigs with tinnitus after salicylate. A) An example animal shows significantly increased normalized startle response ratios in the 12-14 and 16-18 kHz noise bands after receiving salicylate (red) compared to baseline (blue), but not in the BBN and 8-10 kHz bands. **B)** The left axis shows the percentage of animals having tinnitus within the band (pink), while the right axis shows the average tinnitus spectrum (dashed black lines; data are mean+/-SEM). **C)** Pooled TIs from all tested animals that went through GPIAS and operant testing (n=4/7) for within tinnitus frequency bands (red) and outside tinnitus frequency bands (blue) are not significantly different compared to TI distributions from Marks et al. (2018). Data shown are mean+/-SEM. Significance assessed using two-way ANOVA. Alpha = 0.05.

A

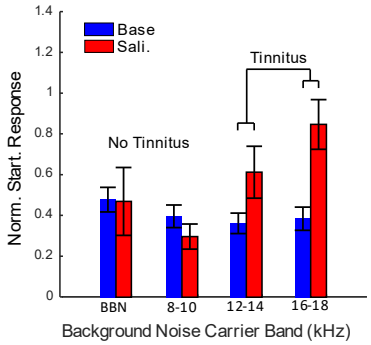

B

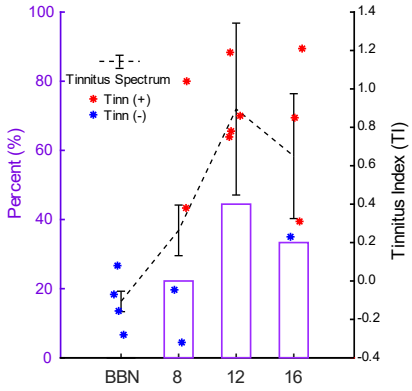

C

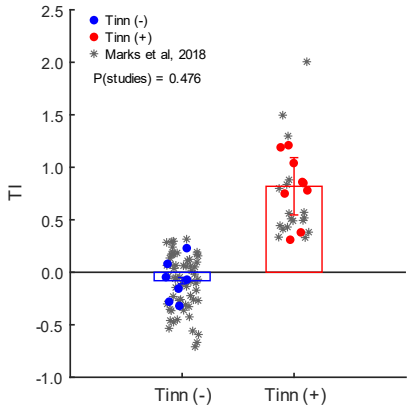

Figure 2.3. Operant conditioning identifies tinnitus in guinea pigs after salicylate, but not saline injections. A) Guinea pigs that consistently showed high learning rates moved onto tinnitus testing (dashed blue lines), while guinea pigs that failed to do so were removed from further study (solid red lines). **B)** When administered saline during silence trials, animals did not show significant changes from baseline in their normalized crossing rate (light blue). However, after salicylate administration, animals showed significantly increased crossing rates (red) (Chi-square test of proportions, p=5.03e-4, n=4).

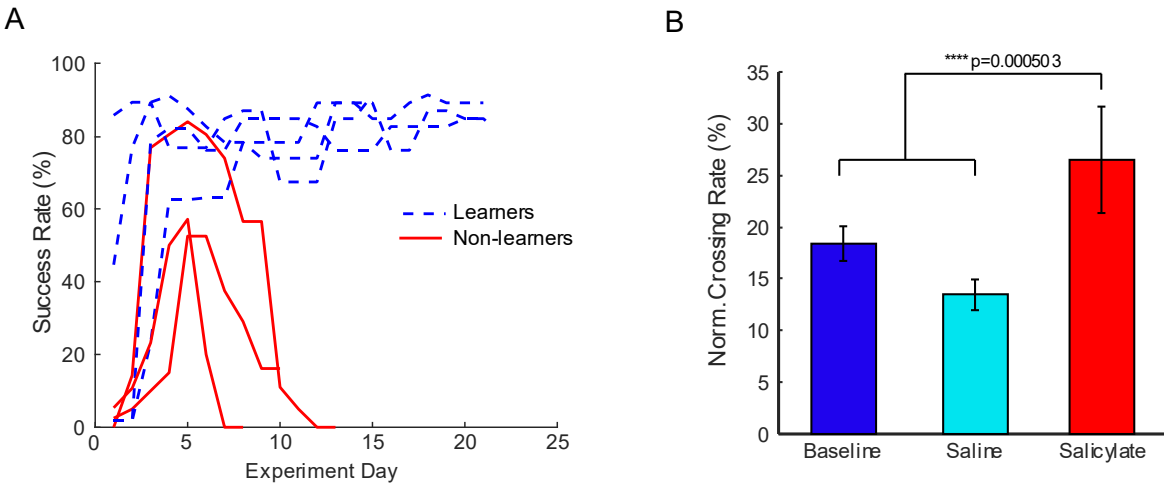

Figure 2.4. Salicylate induces increased ABR thresholds, increased SFR and synchrony in DCN fusiform cells. A) Fraction of units by best frequency, with no-tinnitus frequencies (blue bars) and tinnitus frequencies (red bars) indicated. 46.85% of units were within a no-tinnitus band, while 53.15% of units were in a tinnitus band. **B)** ABRs were measured before surgery (blue) and post-salicylate administration after 30 minutes had past (red). **C)** Fusiform cells in all test animals showed significant increases in SFR after salicylate administration (red circles) compared to baseline (blue stars). **D)** Change in SFR for each unit from baseline to salicylate (red stars; mean+/-SEM indicated by dashed black line). Most increases occurred in frequencies where GPIAS-measured tinnitus was confirmed (pink line). **E)** Cross-unit synchrony between pairs of spiketrains was computed at baseline (blue) and post-salicylate (red; see inset for sample cross-correlations) and significantly increased over the range of geometric mean BFs of sampled pairwise spiketrains (ANOVA2; p=7.26e-89, n=4404). **F)** Synchrony and SFR increased their correlation (r=0.3818) post-salicylate administration compared to baseline (r=0.127; Pearson's linear correlation). Data shown are mean+/-SEM; alpha = 0.05.

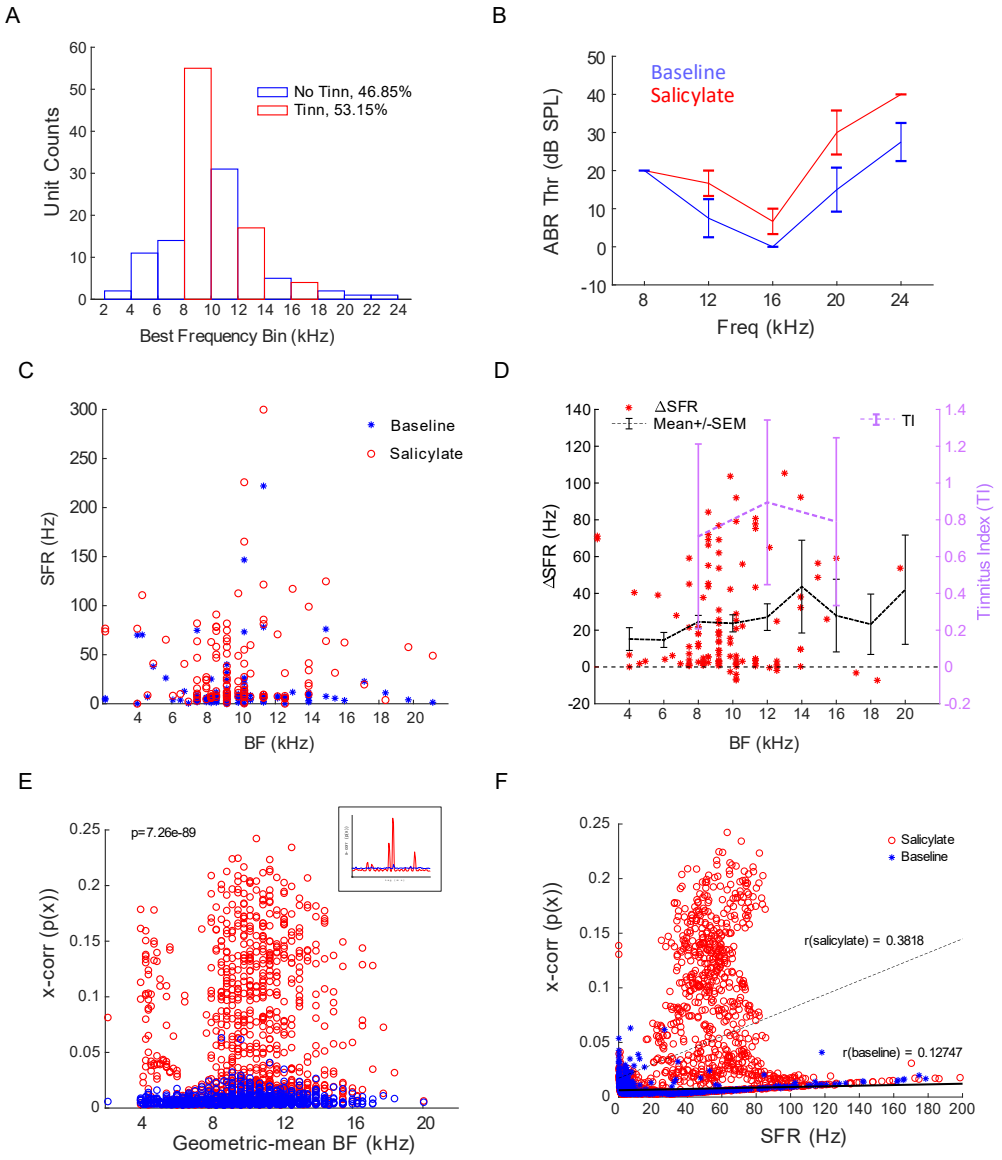

Figure 2.5. Salicylate induces frequency-specific enhancements of STDP timing rules in DCN fusiform cells. A) Mean StDP timing rules show inversion of the timing rules and LTP at more pairing protocol intervals after salicylate administration (red) compared to baseline (blue) (ANOVA, p=0.0036, N=199). Bimodal ordering (Aud-Som vs Som-Aud) indicated by yellow and blue symbols. Data shown are mean+/-SEM pooled across frequencies. **B)** Timing rules from units in a GPIAS-confirmed tinnitus band (dashed red line with square markers) show LTP, while timing rules from units outside GPIAS-confirmed tinnitus bands show mostly LTD (solid red line with circle markers).

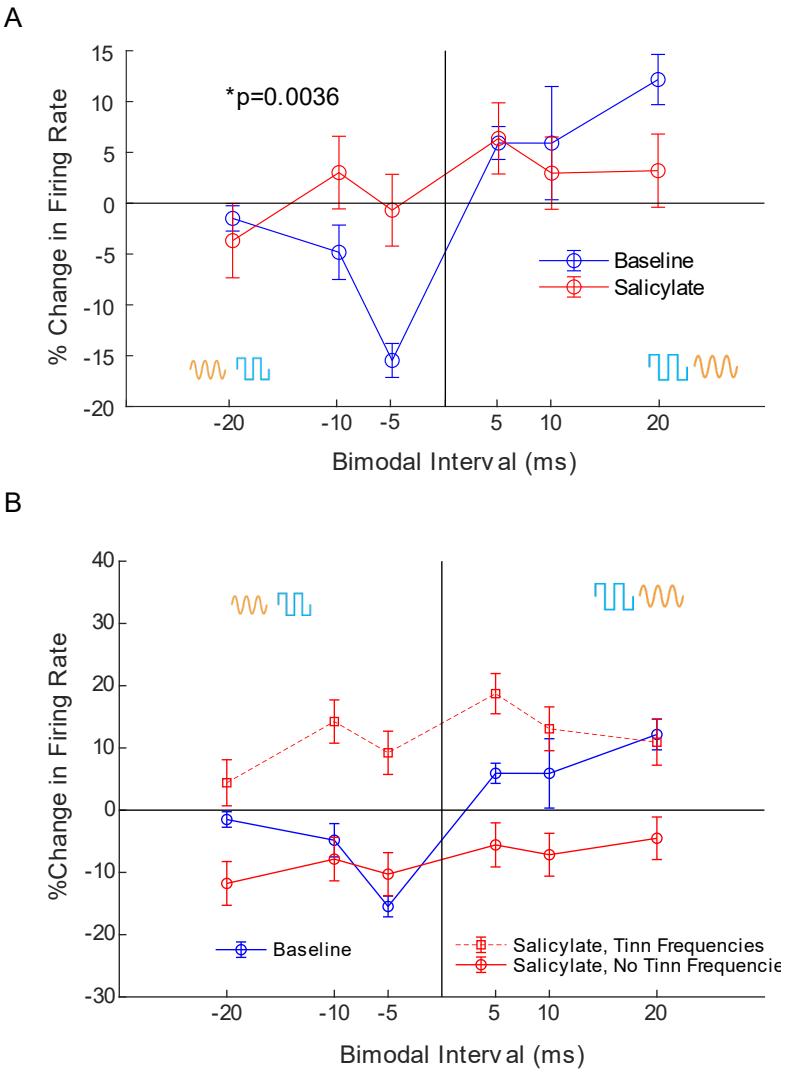

Discussion

In the present study, we demonstrate that guinea pigs administered salicylate, but not saline, show behavioral evidence of tinnitus using two behavioral tests, GPIAS and operant conditioning. Furthermore, we demonstrate that fusiform cells in these same animals show increased SFR and synchrony post-salicylate administration compared to baseline, as well as altered StDP timing rules that show tinnitus-related increases in LTP. This evidence suggests that like noise overexposure, salicylate triggers important tinnitus-related changes in fusiform cell plasticity.

Following salicylate administration, animals are reliably diagnosed with tinnitus by both GPIAS and our operant conditioning paradigm.

All mammals have a startle response, which consists of a contraction of major muscles in the presence of loud and unexpected noise (Holt and Koch, 1999). Furthermore, mammals also exhibit prepulse inhibition, wherein the startle response is reduced by presenting a weaker stimulus in the form of a background noise before the stronger stimuli (Fendt et al., 2001). Similarly, if a silent gap is inserted in the ongoing background noise before the stronger stimuli, then the animal will startle less. Therefore, any noise at the same frequency as the background noise that masks the gap will result in the animals exhibiting a full startle response. The GPIAS reflex test takes advantage of this “masking” effect to detect the presence of tinnitus (Turner et al., 2006; Yang et al., 2007) (**Fig 2.1B**). Further, GPIAS can be used to estimate the tinnitus spectrum and strength if multiple background frequency bands are presented (Kalappa et al., 2014b; Wu et al., 2016; Marks et al., 2018).

However, GPIAS has been criticized as a tinnitus assessment (Fournier and Hebert, 2013; Galazyuk and Hebert, 2015). Cross-validating GPIAS with another widely accepted behavioral paradigm is important for the tinnitus research field (**Fig. 2.1A**). To this end, we performed an operant conditioning test based on fear-conditioning, with modifications for guinea pigs (Ruttiger et al., 2003; Yang et al., 2011). Our operant conditioning test pairs an unconditioned stimulus (sound) to a conditioned stimulus (footshock), a well-established paradigm. Here, once the sound goes on, the animal must cross the chamber to avoid a footshock. In our paradigm, we used the phantom perception of sound to act as the unconditioned stimulus, given that the phantom perception of sound had a frequency found within the unconditioned stimuli. Therefore, if the animal had tinnitus, it would cross from one side of the chamber to the other to avoid the anticipated incoming shock, thereby increasing the crossing rate when compared to baseline. The data gathered with this test was consistent with other behavioral tests assessing salicylate- and noise-induced tinnitus (Guitton et al., 2003; Ruttiger et al., 2003; Turner et al., 2006; Yang et al., 2007; Stolzberg et al., 2013). For example, Guitton et al. (2003) created a behavioral model to test for tinnitus, where they conditioned rats to jump on to a pole whenever they heard a sound to avoid being shocked. Therefore, if they heard a phantom perception of sound after salicylate treatment, they would jump onto the pole to avoid being footshocked, even in the absence of an external stimuli. Like our test, this operant conditioning relied on the phantom perception of sound to avoid a footshock. Nevertheless, contrary to the operant conditioning task employed in our study, GPIAS allowed us to gather more information on the characteristics of the tinnitus by allowing us to measure the guinea

pig's tinnitus spectrum. To generalize operant conditioning, multiple tones at several intensities should be used to assess for the frequency and intensity of the tinnitus. Further, additional analyses, such reduced successful crossing rates for specific frequency bands, could be employed. Another major limitation of the operant paradigm compared to GPIAS is that many animals will not learn the crossing behavior. The non-learning animals exhibited freezing behavior, where an animal would huddle in a corner of the box and not leave it, regardless of electrical current levels applied to the animal. Further training periods could help improve our learning rates. Additionally, providing an additional sensory cue could help reduce freezing rates. Non-learning necessarily reduces testing throughput, as well as potentially selects for animals that are physiologically different from the non-learners. Further, operant conditioning outcomes are parameter sensitive. Increasing the sound duration and pre-sound holding period could potentially increase learning rates. Indeed, in several pilot animals, we found that using 5 second sound stimuli, with 10-20 second holding periods resulted in a lower success rate compared to the present results. In any case, further optimization of the protocol is essential to increase the usability of the test.

Salicylate is an important tool for assessing tinnitus behavior as it reliably induces tinnitus in both humans and non-human species (Guitton et al., 2003; Stolzberg et al., 2012). However, elevated auditory thresholds that arise following its administration complicate tinnitus testing (**Fig. 2.4B**), as impaired hearing can result in false-positive diagnoses of tinnitus. For example, GPIAS requires detection of a gap-prepulse; hearing loss at the same frequency as the background carrier will reduce the salience of the gap, increasing normalized startle ratios and indicating tinnitus.

However, not all hearing loss results in tinnitus (Roberts et al., 2008; Roberts et al., 2010), and neither cochlear synaptopathy nor ABR threshold shifts reliably distinguish tinnitus animals from no-tinnitus animals (Li et al., 2013; Li et al., 2015; Wu et al., 2016; Marks et al., 2018). Further, noise-overexposure is the most common cause of tinnitus in humans (Axelsson and Ringdahl, 1989; Shore et al., 2016b), making its study more relevant for understanding the pathophysiology in humans. Thus, while the present findings are an important proof-of-concept, future studies are essential to cross-validate operant conditioning and GPIAS with noise-induced tinnitus.

Increased SFR, synchrony and altered StDP timing rules in DCN fusiform cells following salicylate administration underlie tinnitus behavior

The present results suggest that salicylate-induced tinnitus may have a similar pathophysiology as noise-overexposure-induced tinnitus (Koehler and Shore, 2013c; Marks et al., 2018). Both salicylate and noise-overexposure result in enhanced StDP timing rules, increased SFR and synchrony in tinnitus animals compared to non-tinnitus animals (**Figs. 2.4, 2.5**). In the present study, these changes were specific to units with BFs within the tinnitus frequencies: salicylate induced increases in LTP from fusiform cells with BFs within the tinnitus frequencies, while inducing LTD outside the tinnitus frequencies. Furthermore, fusiform cells in tinnitus animals have been demonstrated to be hyperexcitable and hypersynchronous by several other groups, utilizing a variety of tinnitus assessment techniques (Middleton et al., 2011; Dehmel et al., 2012b; Pilati et al., 2012; Li et al., 2013; Li et al., 2015). Hypersynchronous fusiform cell firing could bind increased SFR into an auditory object that the brain interprets as a phantom sound

(Singer, 1999). This notion is consistent with the increased correlation between synchrony and SFR found post-salicylate administration (**Fig. 2.4E, F**), potentially increasing the salience of spontaneous neural activity. Thus, the present findings reinforce the link between tinnitus, fusiform cell hyperexcitability and pathologically enhanced LTP arising from reduced ANF output.

In contrast to the present findings, Wei et al. (2010) showed that *in vitro* bath application of salicylate to a fusiform cell culture reduced SFR through a reduction in membrane excitability. One factor to explain these differences is that *In vitro* preparations remove multisensory and other descending input into the fusiform cell circuit, and therefore may not fully reflect pathological processes that underlie salicylate-induced tinnitus. Furthermore, *in vitro* preparations necessarily remove afferent input to the fusiform cell. Many labs have shown that salicylate alters cochlear function through multiple, distinct mechanisms. Altered afferent input could in turn have complex effects on fusiform cell activity that are not accounted for *in vitro.* Alternatively, since the present findings show that salicylate induces increases in LTP from fusiform cells with BFs within the tinnitus frequencies, while inducing LTD outside the tinnitus frequencies, the Wei et al. (2010) study may have sampled from fusiform cells outside a tinnitus frequency region in DCN, and thus consistent with our present findings. Finally, Wei et al. only applied salicylate briefly, whereas our recordings were delayed until 30 minutes after salicylate injection and lasted for several hours. Treatment duration can change physiological responses to salicylate. Cazals et al. (1998) demonstrated that short-term application of salicylate can reduce ANF activity, while long-term, regular dosing reduces the magnitude of this effect.

There are several ways that salicylate could induce fusiform cell hyperexcitability. Following cochlear-damage, reduced ANF output triggers upregulation of excitatory somatosensory inputs to DCN fusiform cells and cartwheel cells (Shore et al., 2008; Zeng et al., 2009). At high doses, salicylate increases hearing thresholds and reduces ANF output, with a maximal reduction occurring between 2 to 4 hours after administration (**Fig. 2.4B**) (Cazals et al., 1998; Muller et al., 2003). Reduced ANF output caused by salicylate could therefore trigger an upregulation of excitatory inputs to DCN fusiform-cell apical dendrites and cartwheel cell dendrites, which could increase synchrony through enhanced parallel fiber input or by enhancing N-methyl-D-aspartate (NMDA) receptor activity. Alternatively, increased SFR and synchrony could result from disinhibition of the fusiform cell. In addition, salicylate is a glycine receptor antagonist (Lu et al., 2009), the application of which could result in increased SFR in fusiform cells. Reduced glycinergic inhibition has been observed in DCN fusiform cells from animals with noise-induced tinnitus (Wang et al., 2009). Salicylate could enhance fusiform cell firing through its activity on NMDA receptors since it acts as an NMDA receptor agonist (Guitton et al., 2003). NMDA receptors have been found on fusiform cells and have been shown to mediate StDP timing rules and firing rate changes (Stefanescu and Shore, 2015). Stefanescu and Shore (2015) demonstrated that antagonizing NMDA receptors led to reduced synchrony between fusiform cells. Blocking NMDA receptors results in less intracellular Ca^{2+} and leads to an inhibition of LTP and LTD (Magee and Johnston, 1997; Bi and Poo, 1998; Han et al., 2000; Tao et al., 2001). Thus, it is not surprising that by activating NMDA receptors, salicylate leads to increases in synchrony, SFR, enhanced LTP and thus, tinnitus.

CHAPTER III

Ventral Cochlear Nucleus Bushy Cells Exhibit Hyperacusis-like Neural Coding after Noise-exposure

To compare VCN bushy cell responses to DCN fusiform cell responses, data from fusiform cells gathered in previous experiments were provided by Dr. Calvin Wu (Wu et al., 2016; Marks et al., 2018). All figures featuring these data are clearly marked as such.

Introduction

Psychophysical studies characterize hyperacusis as increased loudness growth (Baguley, 2003) over a wide frequency band (Schecklmann et al., 2014; Tyler et al., 2014; Sheldrake et al., 2015), reduced behavioral response latencies (Lauer and Dooling, 2007) and decreased tolerance to loud sounds (Tyler et al., 2014).

Neurons that encode for hyperacusis should show hyperexcitable firing patterns that reflect the psychophysical characteristics of hyperacusis (Zeng, 2013; Brotherton et al., 2015). First, neurons encoding hyperacusis should show increased firing rates at high intensities. Second, firing rate enhancements should be not restricted to a frequency region, consistent with the wideband nature of hyperacusis. Third, first-spike

latencies should be shorter at high intensities, as spike latency reflects the faster reaction times seen in hyperacusis. Fourth, neural responses to sound are expected to be more synchronous, reflecting increased perceptual binding of stimuli.

Previous studies suggest that bushy cells of the ventral cochlear nucleus (VCN) are potential candidates for encoding hyperacusis-like neural activity following noise-overexposure (Boettcher and Salvi, 1993; Schrode et al., 2018). Compared to other VCN output neurons, bushy cells show increased phase-locking, a form of neural synchrony, at suprathreshold intensities (Bourk, 1976). Moreover, bushy cells show lower and less variable first-spike latencies than other VCN output neurons (Bourk, 1976; Spirou et al., 1990; Melcher and Kiang, 1996). Following cochlear damage, bushy cells show increased spontaneous firing rates (SFR) across a wide frequency range compared to other CN cell types (Bledsoe et al., 2009; Vogler et al., 2011). Following noise-overexposure and putatively in hyperacusis, we predict that bushy cells will show increased sound evoked responses and reduced latencies to higher-intensity sounds. However, no studies have examined bushy cell firing patterns as a function of suprathreshold sound intensity after noise damage with respect to hyperacusis.

While few studies have examined the neural basis of hyperacusis, many studies have examined the neural basis of tinnitus, or phantom sound perception (Roberts et al., 2010; Shore et al., 2016b; Shore and Wu, 2019). Tinnitus is frequently co-morbid with hyperacusis (Schecklmann et al., 2014; Shore et al., 2016a). Unlike hyperacusis, tinnitus occurs in silence and is spectrally similar to hearing loss profiles (Roberts et al., 2006). Previous studies show that principal output neurons of the dorsal cochlear nucleus (DCN), the fusiform cells, exhibit narrowband increases in SFR and cross-unit

spontaneous synchrony, a neural signature of tinnitus (Wu et al., 2016; Marks et al., 2018). As tinnitus and hyperacusis are frequently co-morbid, it is important to discover whether fusiform cells have a role in hyperacusis, or if bushy cells have a role in tinnitus.

Herein, we hypothesized that VCN bushy cells would exhibit hyperacusis-like neural firing patterns that are independent of the DCN-fusiform-cell neural signature of tinnitus. To test this hypothesis, we employed noise-overexposure and single-unit electrophysiology to study the contributions of bushy cells to hyperacusis neural coding. Following noise-overexposure, bushy cells exhibited hyperacusis-like neural firing patterns, consisting of 1) increased firing rates, 2) reduced and less variable first-spike latencies, and 3) increases in sound-evoked cross-unit synchrony as a function of intensity across a wide range of frequencies. Furthermore, we compared the hyperacusis-like neural firing patterns seen in bushy cells to the previously-established neural signature of tinnitus from fusiform cells. Unlike fusiform cells, bushy cells did not show an association between SFR, synchrony and tinnitus. Rather, bushy cells exhibited enhanced responses as a function of intensity across a wide best-frequency band, consistent with the psychophysics of hyperacusis.

Methods

Ethical Treatment of Animals

All animal procedures were performed in accordance with protocols established by the National Institutes of Health (Publication 80-23) and approved by the University of Michigan Institutional Animal Care and Use Committee (IACUC).

Experimental Design

N=29 female pigmented guinea pigs were obtained from the Elm-Hill colony at 2-3 weeks of age. Animals were noise-overexposed using a paradigm previously established in the lab (**Fig. 3.1A**). Baseline auditory brainstem responses (ABRs) were measured to establish normal hearing followed by four weeks of behavioral testing. All noise-exposed animals received two noise exposures separated by 4 weeks, followed by a second 4-week session of behavioral testing. Single-unit electrophysiology was performed within one week of the final behavioral testing session.

Gap-prepulse inhibition of the acoustic startle (GPIAS) for tinnitus assessment.

A rapid-onset sound (the startle pulse) (**Fig. 3.1B**) results in a startle response in guinea pigs, which can be reduced by presenting a prepulse stimulus (detectable above a background noise) before the startle pulse. Similarly, a gap placed in the background noise before the startle pulse will decrease the startle amplitude. Tinnitus that is spectrally similar to the background noise is indicated as impaired gap-detection ability (Turner et al., 2006).

Guinea-pig startle responses were assessed by measuring their pinna-reflex displacements in (Berger et al., 2013) in response to a 20 ms startle pulse (rise-fall 2 ms). Pinna movements were tracked by video capture of green ink dots, manually applied to both pinnae. Offline, green pixels were identified using a custom-written k-nearest neighbors algorithm (Mathworks MATLAB) (Friedman, 1977; Altman, 1992). Frames in which green points constituted less than 0.01% of pixels were excluded, as

this indicated the ears were not detectable by the camera. Pinna locations were identified by clustering green pixels and computing the centroids of a two-dimensional Gaussian mixture model fit using the Expectation-Maximization algorithm (McLachlan and Chang, 2004). Euclidean distance between (X^{ear} (t), Y^{ear} (t)) points was computed over the trial duration. Trajectory accuracy was verified by trained observers. Startle amplitudes were computed by fitting the trajectory trace to a Gaussian-modulated sine-wave cycle.

Gaps in background noise (65 dB SPL; 50 ms with 5 ms rise/fall times) were presented 100 ms before a broadband noise startle pulse (90 dB SPL; 20 ms with 2 ms rise/fall times). At a given background frequency band (center frequencies of 9, 13, 17 kHz with 2 kHz bandwidths, 25 kHz with a 10 kHz bandwidth, or high pass Gaussian broadband noise), a randomized series of 10 pre-pulses (either silent gap, or a noise pre-pulse at 75 dB SPL) and 10 no-prepulse control background noises were delivered. All testing was performed in sound-proof booths (Acoustic Systems, Inc), with greater than 100 dB acoustic isolation between testing chambers. Trials were randomly presented every 20 to 30 seconds, with prepulse and no-prepulse trials combined into a single per-frequency testing session, and randomly interleaved. Each per-frequency testing session lasted between 9 and 10 minutes. Eight testing sessions were performed each testing day, for an average testing time of approximately 80 minutes. Guinea pigs were tested twice per week, with at least two non-testing days in between each testing day (Mondays and Thursdays or Tuesdays and Fridays) to prevent habituation. Startle amplitudes from each test session were pooled over four weeks. Startle amplitudes greater than two standard deviations above the mean were excluded

from analysis. For each frequency band, a normalized startle ratio (R) was computed as the mean pre-pulse startle distribution divided by the mean of the non-pre-pulse distribution. The normalized amplitudes of the startle reflexes were compared at baseline and after noise-overexposure. An animal was defined as having tinnitus if, at a given frequency, the mean of the post-exposure distribution was significantly greater than the mean of the pre-exposure distribution (Mann-Whitney U-test; alpha = 0.05). The changes in gap R values from pre- to post-exposure were quantified by the standardized tinnitus index [(x – μ)/σ] (Kalappa et al., 2014b; Wu et al., 2016; Marks et al., 2018), where x is the post-exposure gap R value, μ and σ are the mean and standard deviation of pre-exposure gap R value. A significantly higher (positive) index value indicates worsened GPIAS performance and is assumed to indicate tinnitus.

Auditory Brainstem Responses

All electrophysiology testing was performed in a double-walled, soundproof booth (Acoustic Systems, Inc). Animals were anesthetized (40 mg/kg ketamine (Putney Inc.); 10 mg/kg xylazine (Lloyd Inc.)) and unilateral ABRs (**Fig. 3.1C**) were measured (tone pip, up to 1024 repetitions, 5ms duration, 0.5 ms rise/fall time, cos^2 gating; 8, 12, 16, 20, 24 kHz; TDT RX8 DAC, HB7 amplifier, and PA-5 attenuator). Sounds were presented closed field (DT770 Speaker) coupled to the ear canal through custom-built hollow ear bars. Calibration was performed using TDT SigCalRP, a custom MATLAB script and a ¼" microphone (B&K 4136 and Stanford Research Systems SR760 spectrum analyzer; RX8 and PA5; 0.5 mL volume). The system transfer function was flattened with a maximum sound intensity output of 90 dB SPL using FFTs from 200 Hz-

32 kHz. Stainless-steel needle electrodes were inserted into the skin overlying the bullae and at vertex. Evoked potentials were digitized (TDT RA4LI head stage; PZ2-64 pre-amp; and filtered between 300 Hz-3 kHz with a 60 Hz notch). Sounds were presented starting at 90 dB SPL and decreased in 10 dB steps to 0 dB SPL. ABR threshold for a frequency was defined as the lowest sound intensity that did not elicit ABRs with at least three identifiable peaks and troughs.

Noise Overexposure

22 Guinea pigs were noise-overexposed, twice, to narrow-band noise previously shown to induce a temporary threshold shift (Dehmel et al., 2012b; Koehler and Shore, 2013c; Wu et al., 2016; Heeringa et al., 2018c; Marks et al., 2018). A subset of guinea pigs (7) served as sham-exposed (anesthesia-only) controls. Guinea pigs were anesthetized with ketamine/xylazine (40:10 mg/kg). Sound-overexposures (7 kHz centered, half-octave noise at 97 dB SPL) were delivered via microphone inserts into the left ear for 2 hours. ABRs were recorded before and immediately after each noise exposure, as well as prior to single-unit recordings.

Surgical access of the cochlear nucleus

Animals were anesthetized with ketamine/xylazine (40:10 mg/kg) and placed in a hollow-ear-bar stereotaxic frame (Kopf). A custom-built heating pad with closed-loop controller was used to regulate body temperature (38 °C). Anesthetic depth was checked using a toe-pinch, and supplemental anesthesia (0.15 ml of same ketamine/xylazine dose) was administered ~ every 30 minutes. A craniotomy and

duratomy were performed to expose the cerebellum for electrode insertion. The AVCN was accessed using previously established stereotaxic co-ordinates (Heeringa et al., 2018b; Wu and Shore, 2018).

Single-unit Electrophysiology

In vivo unit responses were recorded using multichannel recording electrodes (Neuronexus; 32 channels with 16 channels per 2 shanks; custom headstage). Voltages were digitized (PZ2-64 pre-amp) and bandpass filtered (300 Hz-3 kHz, with a 60 Hz and harmonic comb-filter). Spike thresholds were identified when voltage amplitude crossed 2 standard deviations above the mean voltage arising from spontaneous activity. Units were identified by their responses to 65 dB SPL wideband (200 Hz-40 kHz) search stimuli. Neuron thresholds were stable throughout the experiment with thresholds varying between 40- and 50-dB SPL. Neural spike data was imported into MATLAB and analyzed offline. Spike waveforms were projected into principle component (PC) space and manually clustered by the first three coefficients by a trained user. Unit consistency was maintained by clustering all PC coefficients from a given recording location throughout the experiment. Timestamps were grouped by cluster into isolated units, and spiketrains constructed in MATLAB. Putative bushy-cell single units were identified by their receptive fields (10 dB steps from 0 to 90 dB SPL; frequencies logarithmically spaced from 2k to 24kHz in 0.25 octave steps) (colormap in **Fig. 3.1D**), and either primary-like or primary-like-with-notch peri-stimulus time histograms (PSTH) (lower inset of **Fig. 3.1D**) (Blackburn and Sachs, 1989; Winter and Palmer, 1990b; Ingham et al., 2016). Bushy cells can sometimes be identified by the presence of a pre-potential,

arising from the large, tightly coupled auditory nerve endbulb of Held input on the bushy-cell soma (Bourk, 1976; Keine and Rubsamen, 2015; Keine et al., 2017). Using silicon substrate electrodes, prepotentials can sometimes be identified on putative bushy cells due to low signal-to-noise ratios, as shown previously (Heeringa et al., 2018b). Thus, in a subset of units, pre-potentials were identified (upper inset in **Fig. 3.1D**). Once putative bushy cells were identified, spontaneous activity was collected (at least 150 sec) followed by unit responses to BF tones and broadband noise over a range of intensities (5 dB steps from 0 to 90 dB SPL) (rate-intensity function: filled symbols in **Fig. 3.1E**). 1111 putative bushy cells were identified for analysis, and non-bushy cells were excluded from further analysis. First-spike latency (FSL) was assessed by recording the first spike timestamp post-stimulus onset for each trial (n=100 trials) during rate-intensity function recordings, and the mean for all trials computed (latency-intensity function: open symbols in **Fig. 3.1E**). FSL jitter was assessed as the standard deviation of the FSL distribution.

Hyperacusis Index

A Hyperacusis Index (HI) was computed for each unit as the geometric mean of the unit's 1) average rate-intensity-function slope at intensities greater than 40 dB SPL (nearest base-10 multiple of the average population threshold; 42.1+/-0.48 dB SPL) and less than 90 dB SPL (the maximum calibrated system output for all tested frequencies) and 2) peak firing rate at best frequency from 40 dB SPL to 90 dB SPL.

$$HI = \sqrt{(\ RIF\ Slope * Max(Firing\ Rate))}$$

Synchrony and Spontaneous Firing Rate Assessments

Cross-unit synchrony was computed using cross-correlograms for evoked (Voigt and Young, 1990) and spontaneous activity (Norena and Eggermont, 2003; Wu et al., 2016; Marks et al., 2018). For spontaneous synchrony, 150 seconds of spontaneous activity was recorded. SFR was computed as the average spike rate during this trial. For spontaneous synchrony calculations, spikes co-occurring within a 0.15 ms window were removed. For evoked activity, spikes from frequency-intensity stimulus pairs between receptive fields were pooled. Cross-correlation coefficients ($p(\tau)$) were computed as a function of time lag for each pairwise combination of spike trains.

$$p(\tau) = \frac{R_{AB}(\tau) - E}{\sqrt{N_A N_B}},\ E = \frac{N_A N_B}{n}$$

$R_{AB}(\tau)$ is the unbiased cross-correlation of spike trains *A* and *B*; N_A and N_B indicate spike counts in the respective spike trains. *E* is the mean probability of coincident firing for Poisson-distributed data, defined by the multiplication of N_A and N_B over the number of bins (*n*). Bin size was constant at 0.3 ms (Voigt and Young, 1990). A unit-pair was considered synchronous when the peak *p* value was greater than ±4 standard deviations from the mean $p(\tau)$.

Statistical Analysis

Correlation coefficients were computed using Pearson's algorithm. Slope differences were tested for significance using Analysis of Covariance (MATLAB *aoctool*). Exponential fits were calculated using the least-squares algorithm (MATLAB *fit*). Gaussian-mixture models were fit using the Expectation-Maximization algorithm

(MATLAM *fitgmdist*). Distribution differences were assessed for significance with ANOVAs, Kruskal-Wallis or two-sample KS tests where appropriate (alpha = 0.05). Post-hoc corrections for multiple comparisons were done using the Bonferroni method. The experimenter was blinded as to the status of each animal regarding exposure of behavioral outcome.

Dorsal Cochlear Nucleus Fusiform Cell Data and Analyses

Tinnitus behavioral status in these animals was determined following the GPIAS paradigm presented earlier. SFR, spontaneous synchrony and HI analyses were performed identically between DCN and VCN data. Data were normalized by the control-animal SFR maximum where indicated.

Results

Noise-overexposure produces temporary threshold shifts

While hearing loss is the most common factor associated with hyperacusis, it is not essential for its production (Schecklmann et al., 2014). Thus, to induce hyperacusis while maintaining normal cochlear function, guinea pigs were noise-overexposed twice in a temporary-threshold shift induction paradigm (**Fig. 3.2A**) (Wu et al., 2016). Noise-exposed guinea pigs demonstrated an average threshold shift of 15.9+/-1.13 dB. Consistent with our previous studies utilizing the same noise-overexposure paradigm, ABR thresholds were not significantly different pre-recording compared to baseline (two-way ANOVA; p(group x time)=0.14). ABR wave 1 (W1) amplitude-intensity functions (AIFs), which are used to estimate cochlear function, were calculated. Noise-

overexposed animals showed no significant reduction in ABR W1 amplitude compared to controls across all frequencies and time points (**Fig. 3.2B**; two-way ANOVA; F=2.67; p=0.087), although there was a trend for W1 amplitudes to be smaller in noise-overexposed animals. Startle amplitudes showed no significant differences in noise-exposed animals compared to controls (**Fig. 3.2C**; two-way ANOVA; F=1.04, p=0.38), although a trend for larger startle amplitudes was seen in noise-exposed animals.

Ventral cochlear nucleus bushy cells exhibit hyperacusis-like firing patterns after noise-exposure

Hyperacusis is characterized by enhanced loudness growth at suprathreshold intensities for multiple frequencies (Baguley, 2003; Chen et al., 2013). In bushy cells, firing rate is generally proportional to sound intensity. Thus, we hypothesized that neurons contributing to hyperacusis would show greater firing rates at higher sound intensities and that these would occur over a wide range of BFs. To test this hypothesis, we recorded from putative bushy cells in the VCN across a wide range of BFs. Bushy-cells typically show either primary-like or primary-like-with-notch responses to tones at BF (Winter and Palmer, 1990a). No significant differences were seen between primary-like and primary-like-with-notch units in BF (Student's t-test; p=0.0531), threshold (two-way ANOVA; p(mean x freq) = 0.16) or SFR (two-way ANOVA; p(mean x freq) = 0.0531). Thus, data from both unit types were pooled for remaining analyses. We then measured bushy-cell RIFs to BF tone and broadband noise. Noise-exposed animals showed significantly greater RIF slopes at higher sound levels (inset dashed orange boxes) compared to controls for BF tones (**Fig. 3.3A**; filled symbols; ANOCOVA;

T=18.54, p=1.21e-75) and broadband noise (**Fig. 3.3B**; filled symbols; ANOCOVA; T=15.69, p=1.62e-54), consistent with an expected enhanced suprathreshold loudness growth seen in hyperacusis (Chen et al., 2013; Knudson and Melcher, 2016). Human psychoacoustic studies also demonstrate reduced reaction times in subjects with hyperacusis (Lauer and Dooling, 2007; Zhang et al., 2014), which are thought to arise from a hyperexcitable auditory pathway. To assess neural excitability, we analyzed bushy-cell first-spike latencies (FSL) as a function of intensity. Bushy cells in noise-exposed animals showed steeper FSL slopes as a function of intensity for BF tones at suprathreshold intensities compared to control animals (**Fig. 3.3A**; open symbols; ANOCOVA; T=-35.3, p<1.18e-257). The decrease in FSL was even more pronounced in response to broadband noise (**Fig. 3.3B**; open symbols; ANOCOVA; T=-27.46, p<2.76e-154). Bushy-cell excitability was further assessed by plotting firing-rate as a function of first-spike latency. More excitable neurons are expected to have greater firing rates and lower latencies than less excitable neurons. Inverse-exponential functions (firing rate = A*exp(-FSL / B)) were fit to the data using least-squares regression. Bushy cells in noise-exposed animals showed reduced first-spike latencies for a given firing rate than controls for both tones (**Fig. 3.3C**; B(exp) = 8.34+/-0.42 ms, B(cont) = 11.17+/-1.48 ms) and BB noise (**Fig. 3.3D**; B(exp) = 10.38+/-0.53 ms, B(cont) = 12.29+/-1.43 ms). Neural excitability can also be assessed by spiking reliability, or spike jitter, in response to a stimulus. More excitable neurons should more reliably produce spikes at stimulus onset compared to less excitable neurons. We quantified the bushy cell spike jitter by measuring FSL standard deviation. Bushy cells in noise-exposed animals exhibited reduced FSL jitter to BF tones (**Fig. 3.3E**; ANOCOVA; T=-

32.45, p<7.34e-213) and to broadband noise (**Fig. 3.3F**; ANOCOVA; T=-34.54, p<9.67e-241) compared to control animals.

Next, we examined the relationship between bushy-cell evoked firing rate patterns and hyperacusis characteristics by constructing a neural “Hyperacusis Index” (HI) for each neuron. The HI is equal to the geometric mean of 1) the RIF slope in response to sounds from 40 dB SPL to 90 dB SPL (dashed black line in **Fig. 3.4A**) and 2) the peak firing rate of the RIF (orange stars in **Fig. 3.4A**). Neither primary-like nor primary-like-with-notch units exhibited significant differences in HI (two-way ANOVA; p(mean x freq) = 0.75), and so data from both unit types were pooled for the following analyses. To determine whether an animal had hyperacusis, an unsupervised cluster analysis was performed by fitting HI with a two-member Gaussian-mixture model. A unit was defined as a *Hyperacusis Unit* if the probability of assignment to the elevated HI cluster was greater than 0.5, which corresponded to HI = 35.5 (Hyperacusis threshold) (**Fig. 3.4B**). 25.5% of units were classified as *Hyperacusis Units* (right half of 4B), while the remaining 74.8% of units were *Non-Hyperacusis Units* (left half of 4B). Noise-exposed animals had more units with HIs above the Hyperacusis threshold compared to non-exposed control animals (dashed orange line in **Fig. 3.4C**). The elevated HIs were not restricted to a frequency band, consistent with the reported wideband characteristics of hyperacusis (Baguley, 2003; Sheldrake et al., 2015) (**Fig. 3.4C**). The *Hyperacusis Units* also showed significantly elevated SFR across all frequencies (left panel in **Fig. 3.4D**; two-way ANOVA; p(SFR) = 5.38e-87, p(freq) = 0.26) compared to the non-Hyperacusis units (right panel in **Fig. 3.4D**). A Gaussian mixed model fit to HI and SFR data revealed that the *Hyperacusis Units* could be separated into two clusters, one of

which demonstrated elevated HI (cluster 1 in **Fig. 3.4E**), while the second showed elevated HI and elevated SFR (cluster 2 in **Fig. 3.4E**).

As synchronicity of firing can reflect perceptual binding of stimuli (Singer, 1999), we hypothesized that bushy-cell evoked firing might be more synchronous in hyperacusis. To test this hypothesis, we computed cross-correlations between unit-pair evoked responses (Voigt and Young, 1990) acquired during receptive field measurement. Cross-correlation coefficients (evoked x-corr coef) were then averaged from 40-90 dB across frequencies. Each unit-pair average p-value and HI were binned by BF (9, 13, 17, 21 kHz +/- 4kHz). Evoked synchrony correlation coefficients significantly correlated with HI for noise-exposed animals (**Fig. 3.4F;** Pearson's correlation; r=0.43, p=0.021), but not for controls (Pearson's correlation; r=-0.32, p=0.29). These findings suggest that following noise exposure, bushy cells show a neural signature comprised of steepened RLFs across BFs and increased evoked synchrony, consistent with hyperacusis.

Hyperacusis and tinnitus have distinct neural substrates

Tinnitus and hyperacusis are frequently, but not always, co-morbid (Schecklmann et al., 2014; Sheldrake et al., 2015). Since our data suggested that some noise-exposed animals show neural signatures of hyperacusis, we considered that some of the noise-exposed animals might also show neural and behavioral evidence of tinnitus. Animals were tested for tinnitus using gap-prepulse inhibition of the acoustic startle (GPIAS) (Turner et al., 2006; Berger et al., 2013; Wu et al., 2016), in which animals are diagnosed with tinnitus if they exhibit impairments in gap-prepulse

detection. Ten out of twenty-two noise-exposed animals demonstrated impaired gap-prepulse detection in at least one tested frequency-band, while no control animals demonstrated gap-prepulse impairments at any frequency-band. To control for potential frequency-specific temporal-processing deficits, noise-PPI was also assessed (Shore and Wu, 2019). No animals showed significant deficits in noise-PPI, consistent with previous studies utilizing the same paradigm (Wu et al., 2016; Heeringa et al., 2018c; Marks et al., 2018; Martel et al., 2019).

To assess whether bushy-cell spontaneous activity contributed to evidence of tinnitus, frequency-specific SFR and cross-unit spontaneous synchrony (X-corr coef), two neural hallmarks of tinnitus (Norena and Eggermont, 2003; Kalappa et al., 2014b; Wu et al., 2016), were examined. We found that mean SFR was increased in bushy cells in tinnitus animals compared to exposed, no-tinnitus animals and controls (exposed, tinnitus=30.18 Hz; exposed, no-tinnitus=22.42 Hz; control=18.89 Hz). Further, bushy-cell SFR was increased across all BFs (two-way ANOVA; p(mean)=3.04e-2; p(freq) = 0.18). Wideband increases in bushy cell spontaneous activity may be more reflective of hyperacusis than tinnitus. When binned by BF and tinnitus-carrier-band frequency, bushy-cell SFR did not significantly correlate with tinnitus behavioral measures (**Fig. 3.5A**; Pearson's correlation; r=0.06, p=0.14) compared to that of DCN fusiform cells (**Fig. 3.5B**; Pearson's correlation, r=0.21, p=1.7e-8) (Wu et al., 2016). Furthermore, best-frequency-specific increases in cross-unit spontaneous synchrony did not correlate with tinnitus behavior (**Fig. 3.5C**; Pearson's correlation; r=6.7e-4, p=0.87). In contrast, fusiform cell cross-unit spontaneous synchrony highly correlated with tinnitus behavior (**Fig. 3.5D**; Pearson's

correlation; r=0.21, p=0.026). These findings suggest bushy-cell spontaneous activity does not contribute to tinnitus.

Previous studies have demonstrated that synchronous activation of neurons contributes to perceptual binding (Singer, 1999; Engel and Singer, 2001). In tinnitus, enhanced cross-unit spontaneous synchrony would thus signal the presence of sound in the absence of sound (Uhlhaas and Singer, 2006; Womelsdorf et al., 2007; Wu et al., 2016; Shore and Wu, 2019). However, synchrony measurements should control for baseline spontaneous activity, as more spiking can create more opportunities for correlations. Thus, when correlation coefficients are normalized by the number of spikes in each spike train (Voigt and Young, 1990; Wu et al., 2016), enhanced correlations between synchrony and SFR indicate that spiketrains are more similar than predicted by chance. While bushy-cell SFR significantly correlated with synchrony in tinnitus animals (**Fig. 3.5E**; Pearson's correlation; r=0.049, p=3.38e-5), the correlation was 4x smaller than the correlation between SFR and synchrony previously shown in fusiform cells (**Fig. 3.5F**; Pearson's correlation; r=0.21, p=0.026) (Wu et al., 2016). These findings suggest that, while bushy cells may be more spontaneously active in animals with tinnitus, unlike fusiform cells, their spontaneous activity is not synchronously bound into a phantom sound percept.

To relate tinnitus behavior to hyperacusis in bushy cells, we binned HI by carrier frequencies used in the GPIAS tests. HI in a tinnitus frequency-band did not correlate with the corresponding tinnitus index (**Fig. 3.6A**; Pearson's correlation, p=0.43, r = 0.12). Furthermore, evoked cross-unit synchrony, a measure of stimulus binding potentially reflective of hyperacusis, did not correlate with the corresponding frequency-

matched TI (**Fig. 3.6B**; Pearson's correlation, r=-0.23, p=0.11). However, HI significantly correlated with the percent change in startle amplitude from baseline to pre-recording (**Fig. 3.6C;** Pearson's correlation, p=0.05, r=0.35). Further, evoked synchrony correlation coefficients significantly correlated with binned HI (**Fig. 3.6D;** Pearson's correlation, r=0.43, p=0.021). These findings suggest that bushy-cell evoked activity unlikely contributes to tinnitus, but instead is more consistent with hyperacusis.

We then asked how bushy-cell evoked activity compared to fusiform-cell evoked-activity. The most striking difference between bushy cells and fusiform cells is the order-of-magnitude greater evoked firing rates in bushy cells compared to fusiform cells, suggesting that bushy cells contribute to loudness coding, but fusiform cells do not. HIs and RIFs from bushy cells and fusiform cells were grouped by tinnitus-status. Bushy-cell RIFs showed greater suprathreshold increases in firing in tinnitus animals compared to non-tinnitus animals and controls (upper dashed purple arrow in **Fig. 3.7A**). In contrast, fusiform cell RIFs were not enhanced at suprathreshold intensities (upper dashed purple arrow in **Fig. 3.7B**) in animals with tinnitus compared to either exposed, no-tinnitus animals or controls. Moreover, bushy cells in both tinnitus and no-tinnitus animals had HIs above the previously established Hyperacusis threshold (orange line in **Fig. 3.7C**), while fusiform cells did not show any distinct elevations of HI over BF in noise-exposed animals compared to controls (two-way ANOVA; p(freq) = 0.81, p(mean) = 0.31). Furthermore, less than 1% of fusiform-cell HIs were above the bushy-cell Hyperacusis threshold (orange line in **Fig. 3.7D**). As shown in Fig 3.7, bushy cells show distinct clusters when plotting HI versus SFR. But, while most of the data points in each cluster were from animals with tinnitus, both tinnitus and no-tinnitus animals contributed

data points to each cluster (**Fig. 3.7E**). In contrast to bushy cells, there were no distinct clusters of HI versus SFR in fusiform cells, which instead showed large increases in SFR compared to control animals (**Fig. 3.7F**). These findings reiterate that fusiform-cell firing patterns following noise-overexposure and tinnitus induction are reflective of tinnitus, as previously shown, and are inconsistent with the neural signature of hyperacusis found in bushy cells.

Figures

Figure 3.1: Experimental paradigm. A) Animals underwent four weeks of baseline behavioral testing (time = 0 weeks to t = 4 weeks), followed by two separate noise-exposures, each four weeks apart (t(1,2) = 4, 8 weeks). Auditory brainstem responses (ABRs) were measured before and immediately after each noise-exposure. After another four weeks, behavioral testing was resumed (t = 12 weeks) for four weeks, after which electrophysiology experiments were performed (t = 16 weeks). **B)** Guinea pigs startle in response to loud, unexpected sounds (blue pulse embedded in black carrier band; top half of panel), and startle less when a gap in the background noise precedes the loud sound (bottom half of panel). This phenomenon is termed gap-prepulse inhibition of the acoustic startle (GPIAS) and is reduced in animals with tinnitus. **C)** Representative ABR waveform with symbols indicating wave 1 peak and trough (teal stars) and measured W1 amplitude. **D)** Sample receptive field (colormap; cool color reflects low firing rates while warm reflects high firing rates), primary-like peri-stimulus time histogram (PSTH; bottom inset) and averaged spike with prepotential (top inset) from a putative bushy cell. **E)** Rate- and latency-intensity functions (RIF: filled symbols, left axis; LIF: open symbols, right axis), from a putative bushy cell, were measured in response to the best-frequency tones (BF; black) and to broadband noise (orange).

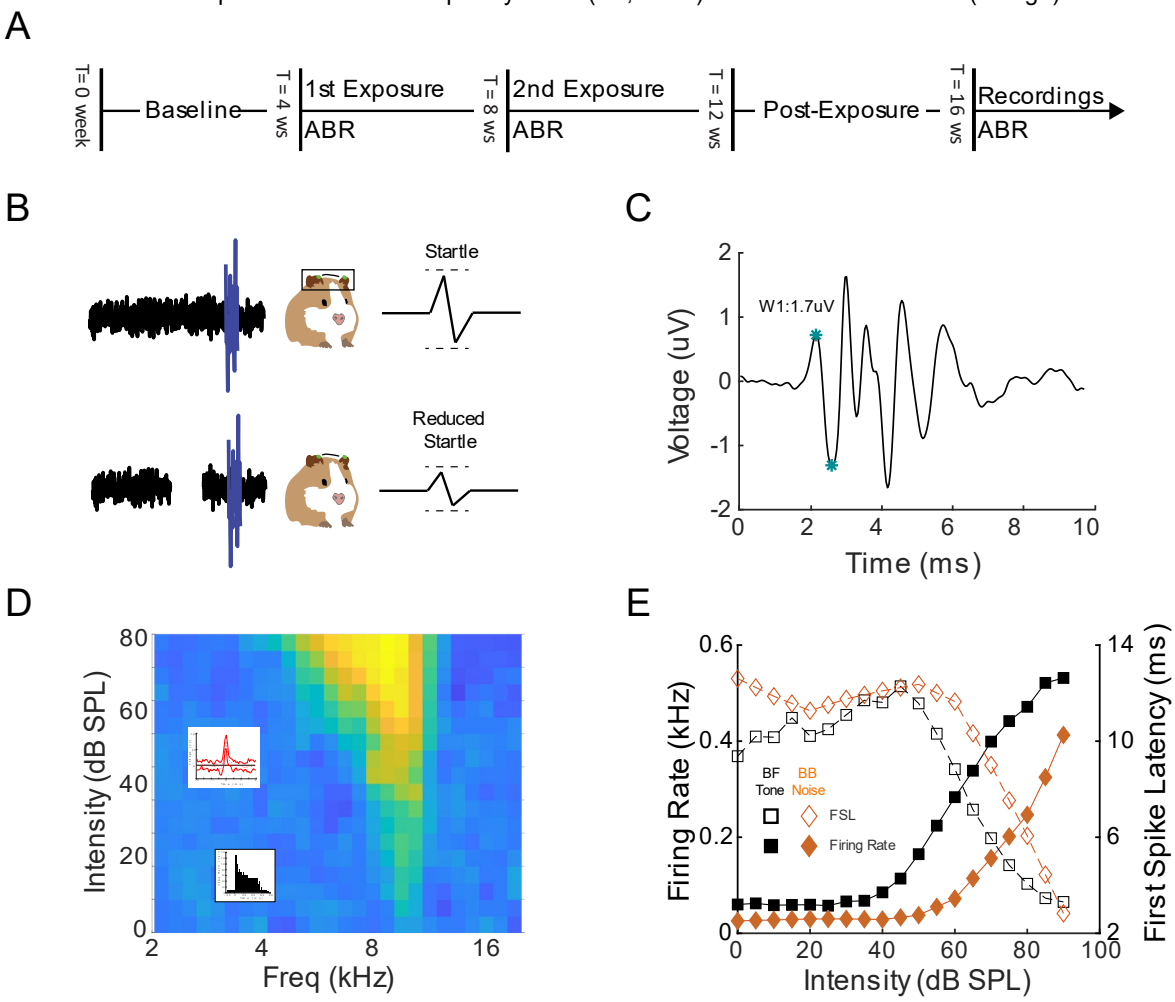

Figure 3.2: Noise-overexposure results in temporary threshold shifts. **A)** Following noise-overexposure (spectrum: green triangle), hearing thresholds for exposed animals were elevated immediately post-exposure (filled pink squares) compared to baseline (filled symbols with solid lines) and prior to surgery (open symbols with dashed lines). Hearing thresholds at baseline and prior to single-unit recordings were not significantly different between noise-exposed animals (purple squares) or non-exposed controls (black diamonds). **B)** ABR W1 amplitude-intensity functions (AIFs) for noise-exposed (purple) and control (black) guinea pigs at baseline (filled symbols with solid lines) and pre-recording (open symbols with dashed lines). **C)** Mean percent-change in startle amplitude from baseline to post-exposure for each GPIAS carrier band for noise-exposed (purple squares) and control (black diamonds) animals. Data shown are mean+/-SEM.

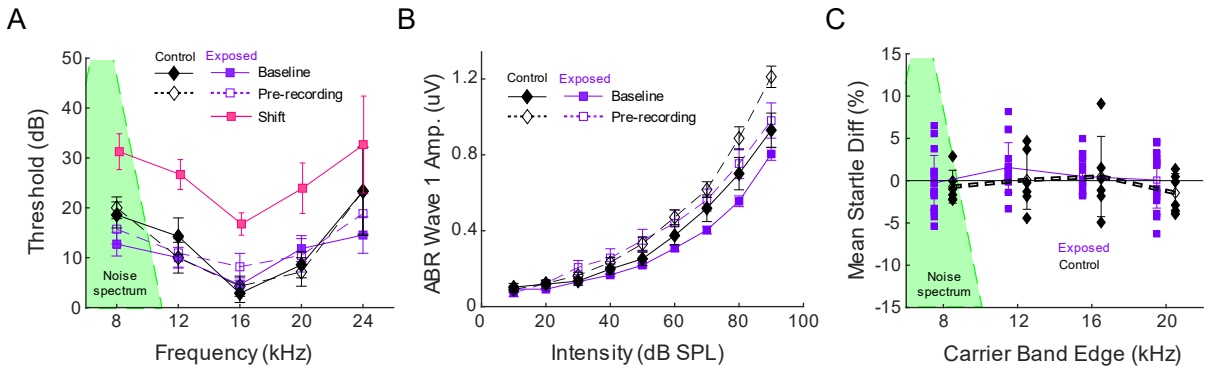

Figure 3.3: Bushy cells in noise-exposed animals show hyperacusis-like firing patterns. RIFs (filled symbols; left axis) and LIFs (open symbols; right axis) from bushy cells in noise-exposed animals (purple squares with dashed lines) and non-exposed controls (black diamonds with solid lines) in response to **A)** tones at unit BF and **B)** broadband noise. Group suprathreshold intensity range indicated by dashed orange boxes. Firing rate versus first-spike latency and fit exponential functions for **C)** BF tones and **D)** broadband noise. FSL jitter, measured as the standard deviation of the FSL, is shown for **E)** BF tones and for **F)** broadband noise. Data shown are mean+/-SEM.

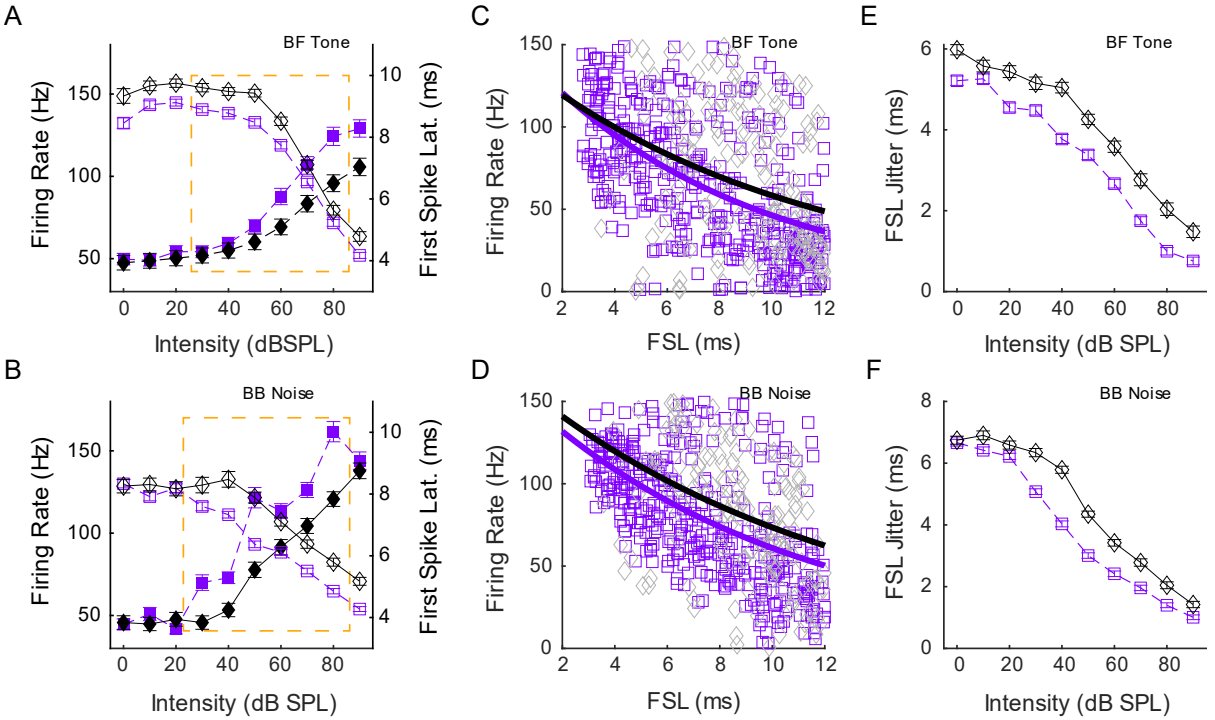

Figure 3.4: Noise-exposed animals show elevated Hyperacusis Indices (HI) compared to controls. A) HI, shown for two example RIFs, was calculated from the geometric mean of: 1) the average RIF slope from 40-90 dB (dashed black line) and 2) peak firing rate over the same intensity interval (orange star). **B)** Probability (Gaussian-mixture model) of classifying a bushy cell as a *Hyperacusis Unit*, with Pr(Hyperacusis) greater than or equal to 0.5 (dashed vertical line) for *hyperacusis units* and less than 0.5 for *non-Hyperacusis Units*. The HI-value at Pr=0.5 point is 35.5, which served as the hyperacusis threshold. **C)** HI vs BF for noise-exposed animals (purple squares) and non-exposed controls (black diamonds) relative to the noise-exposure spectrum (green triangle). Hyperacusis threshold line shown in orange. **D)** Left panel: SFR by BF for *Hyperacusis units*, with distribution mean (orange line). Right panel: SFR by BF for *non-Hyperacusis units*, with distribution mean (orange line). **E)** HI versus SFR, with *Hyperacusis-unit* clusters indicated by orange ellipses. Hyperacusis threshold line shown in orange. **F)** Evoked synchrony, quantified through the cross-correlation coefficient of unit-pair receptive field PSTHs, significantly correlates with the mean HI for exposed animals (purple dashed line) but not for control animals (black dashed line).

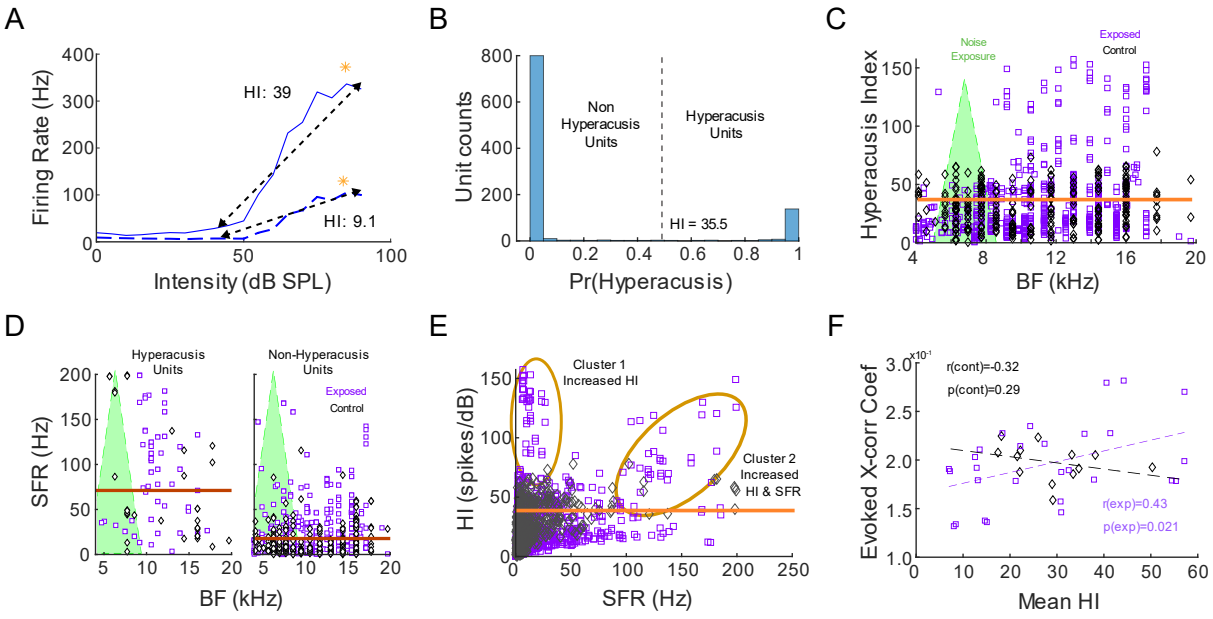

Figure 3.5: Bushy cell spontaneous firing does not relate to tinnitus behavior compared to fusiform cells. Data colored based on tinnitus-status (tinnitus in red, no-tinnitus in blue, and non-exposed controls in black). **A)** Bushy cell SFR, when binned by BF for each Tinnitus Index (TI) carrier-band, does not significantly correlate with TI. **B)** Fusiform cell SFR strongly correlates with frequency-matched TIs. **C)** Bushy cell cross-unit spontaneous synchrony (Spont. X-corr coef), binned by BF per TI-carrier bands, does not significantly correlate with TI. **D)** Fusiform cell X-corr coef significantly correlate with frequency-matched TI. **E)** Bushy cell X-corr coef weakly correlates with geometric mean SFR of contributing unit-pair. **F)** Fusiform cell X-corr coef strongly correlates with geometric mean SFR in animals with tinnitus. Panels B, D and F republished with permission from authors in Wu et al. (2016).

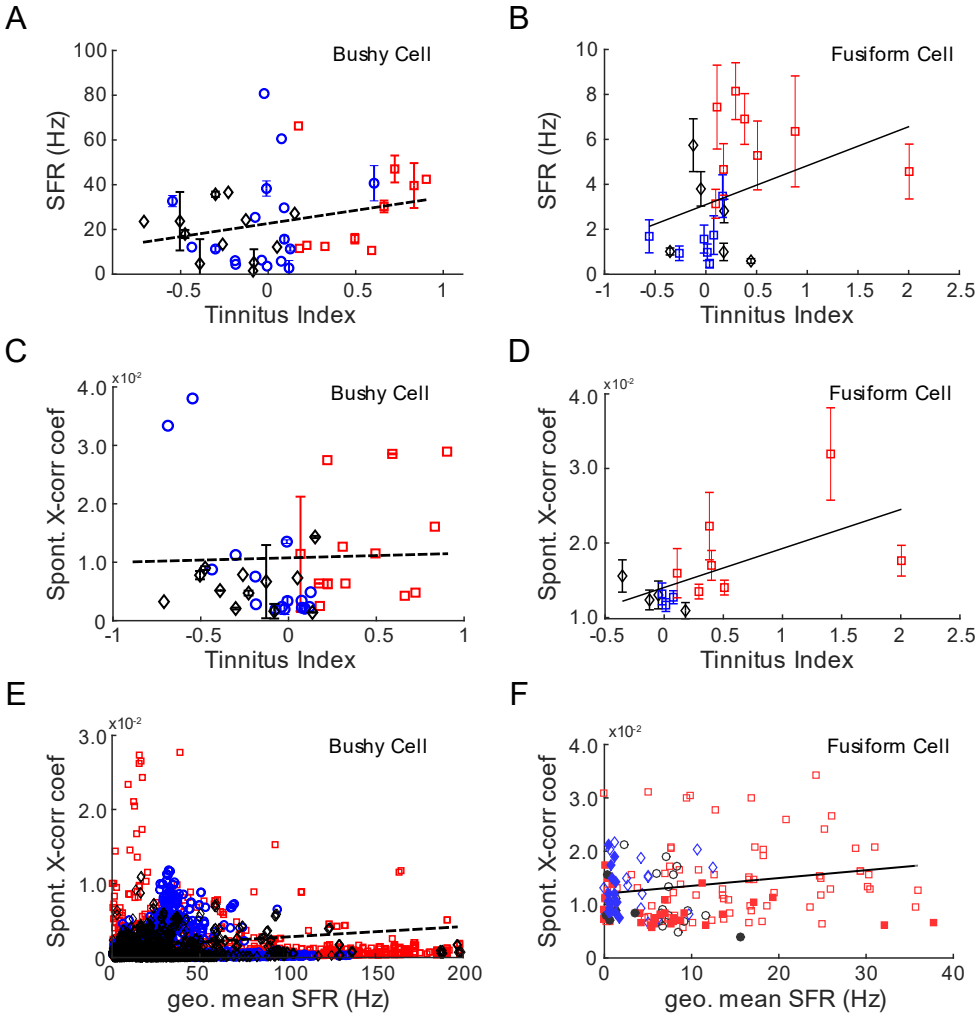

Figure 3.6: Bushy cell sound-evoked activity relates to hyperacusis and not tinnitus. A) Bushy cell mean HI, when binned by BF using TI carrier-bands, does not correlate with TI. **B)** Evoked synchrony, binned by geometric BF of each unit-pair relative to TI carriers, does not significantly correlate with TI. **C)** Mean HI correlates with the percent change in non-prepulse startle amplitudes. **D)** Evoked synchrony correlates with mean HI.

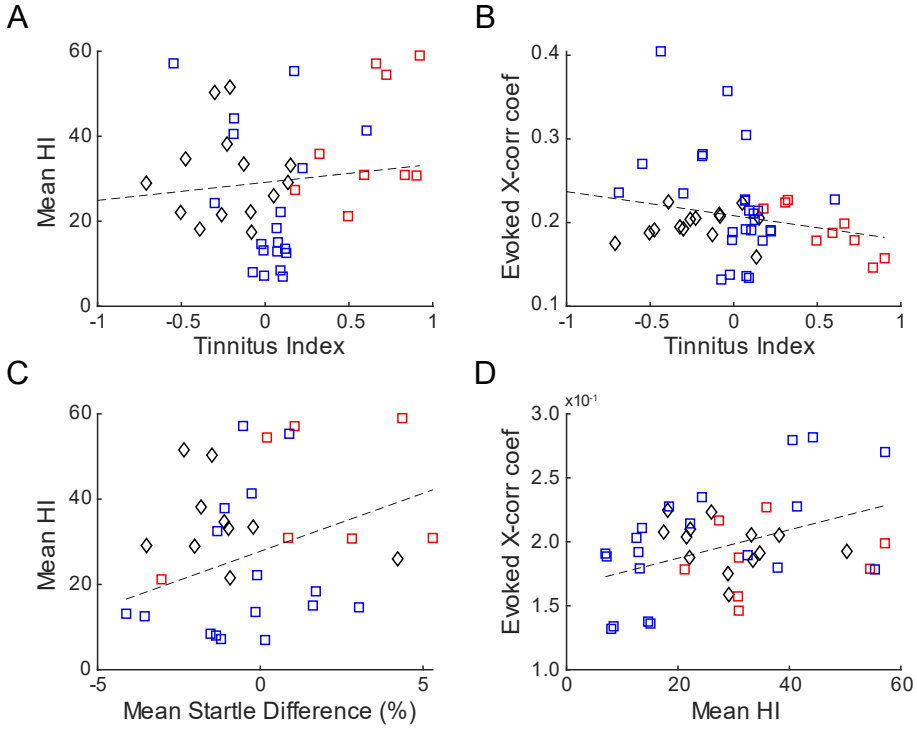

Figure 3.7: Bushy cell neural signature of hyperacusis distinct from fusiform cell measures of hyperacusis. A) Bushy cells in tinnitus animals show suprathreshold RIF slope increases from 40 dB to 90 dB (dashed purple lines). **B)** Rate-intensity functions in FCs do not show suprathreshold slope increases in tinnitus animals from 40 dB to 90 dB (dashed purple lines). **C)** Elevated HIs occur predominantly, but not exclusively, in noise-exposed animals. Hyperacusis threshold line computed from bushy-cell HI distribution shown in orange. **D)** HI is not increased in fusiform cells in noise-exposed animals compared to controls or to bushy cells. **E)** Bushy cell elevated HI-SFR clusters not-exclusively linked to tinnitus-status. **F)** FCs do not show distinct clusters of elevated HI but do show enhanced SFR.

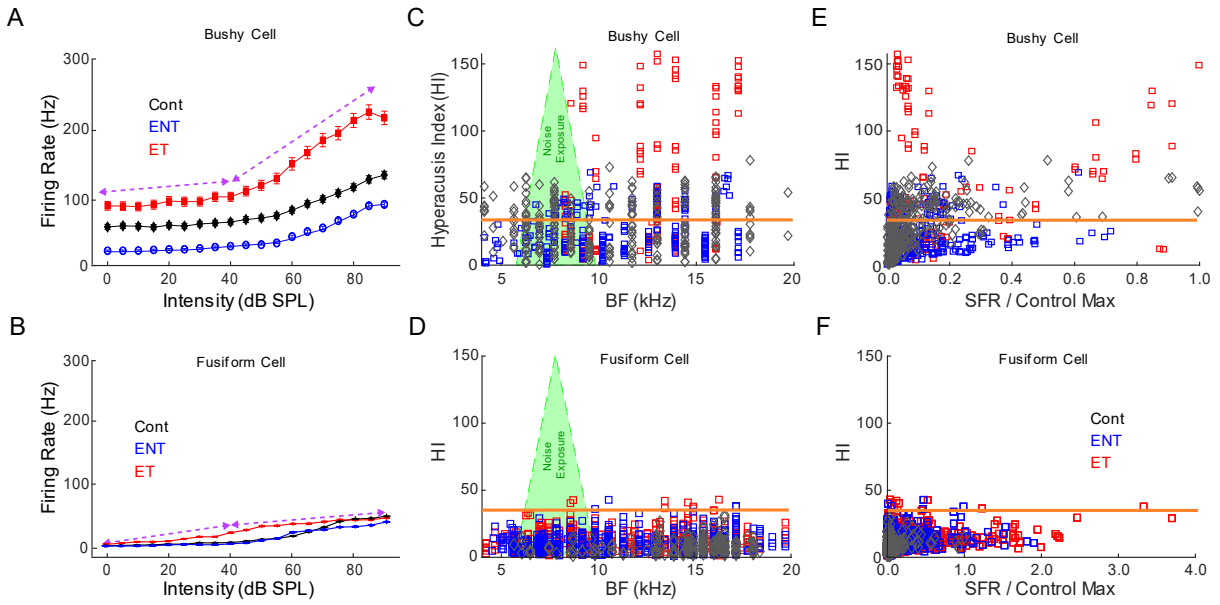

Discussion

In the present study, we showed that VCN bushy cells show hyperacusis-like neural firing patterns following noise-overexposure consisting of steepened rate-intensity functions, reduced and less variable first-spike latencies, and increases in sound-evoked cross-unit synchrony across a wide BF range. Consistent with human studies, in which there is significant co-morbidity between hyperacusis and tinnitus, some putative hyperacusis animals also showed behavioral evidence of tinnitus. Consistent with previous studies, analysis of data from fusiform cells indicated that they do not exhibit hyperacusis-like firing patterns, in contrast to bushy cells.

Mechanisms underlying enhanced bushy-cell excitability

There are several possible mechanisms by which bushy cells could become more excitable after noise exposure, resulting in hyperacusis-like firing. Bushy cells receive somatosensory input on their dendrites which can modulate bushy-cell firing sensitivity (Heeringa et al., 2018c; Wu and Shore, 2018). Following noise-exposure, the anterior VCN receives increased glutamatergic input from non-auditory structures (Heeringa et al., 2018c). Increased glutamatergic somatosensory input (Zhou et al., 2007) could potentially reduce the threshold for bushy cell spiking, resulting in enhanced firing rates and reduced latencies, consistent with the present findings.

In addition to somatosensory input, cholinergic signaling is altered in VCN following noise-exposure (Jin and Godfrey, 2006; Jin et al., 2006) indicated by increases in choline acetyltransferase (ChAT) and muscarinic ACh receptors in the CN. These studies propose that cochlear damage triggers homeostatic increases in ACh-mediated excitability to compensate for reduced auditory nerve output. Interestingly, cochlear insult with carboplatin, a ototoxic anticancer drug, was shown to enhance VCN, but not DCN, expression of Growth Associated Protein (GAP) 43 (Kraus et al., 2009). Increases in GAP-43, reflecting axon growth and synaptogenesis, could result in enhanced synchronization of bushy cells through putative increases in collateralization of bushy-cell dendritic arbors. Increases in VCN neural excitability could also arise through local disinhibition, as measured through reductions in glutamic acid decarboxylase 65 (GAD65) expression (Schrode et al., 2018), a GABA-terminal marker. In that study, reductions in GAD65 co-occurred with increases in startle amplitude and

ABR wave 2:1 amplitude ratio, both measures which are predicted to correlate with hyperacusis.

However, reductions in cochlear output does not need to be permanent to produce increases in CN excitability. Transient reductions in auditory nerve input can also elicit homeostatic increases in CN excitability. Ear plugging can result in increased AMPA receptors expression in the post-synaptic density (PSD) of bushy cells, making them cells more excitable (Clarkson et al., 2016). This increase is sustained after the ear canal is re-opened. Animals with increased AMPA receptor expression and thicker PSDs also showed enhanced later ABR wave amplitudes compared to controls. ABR waves 2 and 3 are predominantly generated by the synchronous firing of bushy cells while waves 4 and 5 are generated by bushy-cell targets in the auditory pathway (Melcher and Kiang, 1996), suggesting that the bushy cell pathway becomes more excitable as a result of enhanced AMPA receptor expression. Other studies have shown that following conductive hearing loss, contralateral inputs to the VCN become more excitatory, resulting in increased SFR and enhanced sensitivity to broadband noise (Sumner et al., 2005). These findings suggest that transient insults to the auditory pathway can have long-lasting changes resulting in a hyperexcitable auditory pathway.

Hyperacusis-like firing patterns could also arise from bushy-cell network changes beyond cellular changes. Bushy cells are part of an electrotonically-coupled network that may allow for the rapid spread of excitation (Gomez-Nieto and Rubio, 2009; Rubio et al., 2014). Enhanced network connectivity could allow bushy cells to fire more rapidly in response to sound with increased synchrony and reduced latency, consistent with the present findings. A similar mechanism has been proposed to account for perceived

brightness in visual cortex: increases in synchrony of stimulus-evoked firing rates correlated with enhancements in perceived brightness (Biederlack et al., 2006; Uhlhaas et al., 2009).

Bushy cells receive inhibitory interneuron input, including wideband inhibition from VCN d-stellate neurons, and narrowband input from DCN vertical cells (Wickesberg and Oertel, 1990; Nelken and Young, 1994; Rhode, 1999; Arnott et al., 2004). In normal-hearing animals, inhibitory input onto bushy cells is essential for maintaining phase-locking in the presence of background noise (Xie and Manis, 2013; Keine and Rubsamen, 2015). By transiently raising bushy-cell spike thresholds, out-of-phase subthreshold membrane summation is prevented from eliciting spikes. Disinhibition of d-stellate or vertical-cell input would result in more, less-precisely timed spikes being generated from bushy cells in response to auditory nerve input, consistent with the present results. Moreover, reduced d-stellate cell input onto bushy cells would also result in enhanced bushy-cell sensitivity to off-BF sounds, consistent with the wideband nature of hyperacusis. Future studies should investigate the roles of d-stellate and vertical cells in hyperacusis.

Co-morbidity of Hyperacusis and Tinnitus

Tinnitus and hyperacusis are frequently co-morbid, with an average co-incidence rate across studies of 60% (Baguley, 2003; Tyler et al., 2014; Sheldrake et al., 2015). Consistent with this observation, we found that a subset of noise-exposed animals shows electrophysiological evidence for both hyperacusis and tinnitus. However, not all hearing loss leads to either tinnitus or hyperacusis; moreover, hyperacusis and tinnitus

can occur independently of each other (Schecklmann et al., 2014). In the present study, all unique combinations of hyperacusis and tinnitus were seen. We found that 50.8% of *Hyperacusis Units* come from animals with tinnitus (tinnitus-with-hyperacusis), while 27.3% of *non-Hyperacusis units* were from tinnitus animals (tinnitus-without-hyperacusis). These proportions suggest that tinnitus-with-hyperacusis is the most common condition resulting from our noise-exposure, which is also consistent with human studies, as the average coincidence rate of tinnitus and hyperacusis is greater than 50%. Further, 25.1% of *Hyperacusis units* came from exposed, non-tinnitus animals (hyperacusis-without-tinnitus), suggesting that some of the non-tinnitus animals might also have hyperacusis.

Behavioral Models of Hyperacusis

While several behavioral tests for hyperacusis have been proposed (Chen et al., 2013; Hayes et al., 2014; Hickox and Liberman, 2014; Salloum et al., 2014; Zhang et al., 2014; Radziwon et al., 2017), there are no widely-adopted behavioral tests for hyperacusis (Eggermont and Roberts, 2015; Brozoski and Bauer, 2016). Current paradigms utilize either enhanced startle amplitudes or reduced reaction times as hyperacusis-measures. As bushy-cells in noise-exposed animals showed both increases in firing rate and reductions in first-spike latency, we propose that a combined measure of both reaction times and startle amplitudes will measure hyperacusis. We predict that animals with hyperacusis will show enhanced startle response amplitude slopes as well as reduced startle reaction time slopes as a function of stimulus intensity, as suggested by the bushy cell RIF enhancements and LIF reductions seen in noise-

exposed animals. Further, because bushy cells in noise-overexposed animals show greater absolute RIF and LIF slopes in response to broadband noise than to BF tones, we predict that animals with hyperacusis will show stronger responses to broadband noise, as wideband sounds are perceived to be louder than SPL-equivalent narrowband sounds (Wagner et al., 2004).

In the present study, noise-exposed animals showed a trend for increases in startle amplitude at several frequency bands. This trend is consistent with another hyperacusis study, which showed that suprathreshold startle enhancements, reflective of hyperacusis, were seen only in response to startle pulses greater than 100 dB (Chen et al., 2013), but not in response to the 90 dB SPL stimulus used in the present study. Future studies should measure startle-amplitude-intensity functions, with peak sound outputs greater than utilized in the present study, to assess hyperacusis-behavior.

We show, for the first time, that VCN bushy cells demonstrate neural firing patterns consistent with hyperacusis, while DCN fusiform cells demonstrate an independent neural signature of tinnitus that is inconsistent with hyperacusis. Future studies should combine DCN and VCN recordings in the same animal, along with combined tinnitus and hyperacusis behavioral tests, to conclusively attribute each disorder to its generating neural population. Moreover, the role of CN inhibitory interneurons in hyperacusis and tinnitus remains to be investigated.

CHAPTER IV

Multiple Mechanisms are Required to Produce Hyperacusis-like Neural Firing Patterns in Ventral Cochlear Nucleus Bushy Cells

Introduction

Bushy cells, a principal-output neuron type in the ventral cochlear nucleus (VCN), exhibit a neural-firing profile consistent with the psychophysical characteristics of hyperacusis (Chapter III) following noise-overexposure. This neural profile consists of steeper rate- and latency-intensity functions (RIFs, LIFs), where the firing rates and first-spike latencies of neurons are measured in response to increasing sound intensities. Bushy cells might contribute to hyperacusis because they demonstrate increased firing rates and lower first-spike latencies at lower sound intensities than in normal animals (Chapter III). Enhanced RIFs and LIFs are consistent with enhanced loudness growth and reduced reaction-times observed in humans with hyperacusis (Lauer and Dooling, 2007). Moreover, RIF and LIF enhancements in bushy cells in noise-overexposed animals occur at all measured frequencies, consistent with the broadband nature of hyperacusis in humans (Schecklmann et al., 2014; Sheldrake et al., 2015).

Bushy-cell hyperacusis-like firing patterns *in vivo* can be clustered into two groups: one group with increases in spontaneous firing rate (SFR) and one without. There are several putative mechanisms that can result in increased bushy-cell excitability following a reduction in cochlear output. Following hearing loss, bushy cells can show increased amino-hydroxy-methyl-isoxazolepropionic acid (AMPA) receptors counts in the endbulb of Held post-synaptic density (Clarkson et al., 2016), directly enhancing bushy-cell excitability. In addition, bushy-cells receive glutamatergic, non-auditory input on their dendrites, which can influence bushy-cell sound-evoked responses (Heeringa et al., 2018a), and is upregulated following auditory damage (Zeng et al., 2009; Heeringa et al., 2018c). Moreover, glycine-driven, sound-evoked inhibition is essential for normal bushy-cell firing patterns (Caspary et al., 1994; Kanold and Manis, 2005; Kuenzel et al., 2011; Nerlich et al., 2014), and disinhibition has been demonstrated after noise-overexposure and age-induced hearing loss (Boettcher and Salvi, 1993; Francis and Manis, 2000). However, it is unclear which mechanisms explain *in vivo* findings in hyperacusis.

In addition to their putative role in hyperacusis, bushy cells are major contributors to the auditory brainstem response (ABRs; Melcher and Kiang, 1996). The ABR is a sound-evoked potential consisting of several sequential waves, which reflect the summed firing of their neural generators. ABR wave 1 (W1) reflects auditory-nerve firing, wave 2 (W2) reflects bushy-cell firing, and the later waves (W3-W5) reflect activity from the targets of the bushy cells (Melcher and Kiang, 1996). Later ABR wave amplitudes are increased in in humans with tinnitus and/or hyperacusis. ABR wave amplitude enhancements are thought to reflect increased central nervous system

activity arising from hyperacusis and/or tinnitus (Schaette and McAlpine, 2011; Gu et al., 2012). As bushy-cells show neural firing patterns that could reflect hyperacusis, including steeper RIFs and LIFs (Chapter III), we hypothesize that animals with hyperexcitable bushy cells will also demonstrate increased ABR-wave 2-5 amplitudes and reduced latencies. However, no studies have shown how enhanced ABR wave amplitudes, putatively linked to hyperacusis, relate to a bushy-cell neural profile of hyperacusis.

In this study, we utilize mathematical models of the auditory periphery and bushy-cell circuitry to examine several mechanisms of increases in excitability consistent with a hyperacusis profile. We also measured ABRs from noise-overexposed animals showing hyperacusis-like neural firing patterns and compare them to simulated model ABRs. Simulated bushy-cell firing patterns were validated against *in vivo* data from guinea pigs (Chapter III). We find that multiple mechanisms of bushy-cell hyperexcitability are required to explain the *in vivo* findings. Moreover, we find that ABR wave amplitudes and latencies from noise-overexposed animals reflect increased bushy-cell excitability, which can be modeled by increased glutamatergic excitation but not glycinergic disinhibition.

Methods

Ethical Treatment of Animals

All animal procedures were performed in accordance with protocols established by the National Institutes of Health (Publication 80-23) and approved by the University of Michigan Institutional Animal Care and Use Committee (IACUC).

Experimental Design

Data collected in Chapter III were used in this study. Full methods are described therein. In brief, 2-3-week-old female pigmented guinea pigs (N=29) were obtained from the Elm-Hill colony. Baseline auditory brainstem responses (ABRs) were measured to establish normal hearing (thresholds, input-output functions). Tinnitus and hyperacusis were induced using a previously established noise-overexposure paradigm (Wu et al., 2016). Neural recordings were performed within one week of the cessation of a second period of behavioral testing. Mathematical simulations were performed using the Matlab Auditory Pathway (MAP) model (Meddis, 2006; Lecluyse et al., 2013) with parameters informed by animal experiments and previously published work in guinea pigs (Sumner et al., 2003; Heeringa et al., 2018c; Heeringa et al., 2018b).

Auditory Brainstem Responses

All electrophysiology testing was performed in a double-walled, soundproof booth (Acoustic Systems, Inc). Animals were anesthetized (40 mg/kg ketamine (Putney Inc.); 10 mg/kg xylazine (Lloyd Inc.); K/X) and unilateral ABRs were measured (tone pip; up to 1024 repetitions; 5 ms duration, 0.5 ms rise/fall time, cosine-squared gating; 8, 12, 16,

20, 24 kHz; TDT System 3). Sounds were presented closed field (DT770 Speaker) coupled to the ear canal through custom-built hollow ear bars. Calibration was performed using a ¼" diameter microphone (0.5 mL volume). The maximum sound intensity was limited to 90 dB SPL (200 Hz-32kHz). Needle electrodes (26 gauge; stainless steel with oxide-coating removed) were used to record potentials and placed at vertex and underneath the bullae. Recorded ABR signals were digitized (TDT System 3; bandpass Butterworth FIR filter, 300 Hz-3kHz, 60 Hz notch). Sounds were presented starting at 90 dB SPL and decreased in 10 dB steps to 0 dB SPL or threshold, whichever came first.

Noise Overexposure

Twenty-two guinea pigs were noise-overexposed, twice (Dehmel et al., 2012b; Koehler and Shore, 2013c; Wu et al., 2016; Heeringa et al., 2018c; Marks et al., 2018), while 7 animals served as sham-exposed (4:1 K/X anesthesia) controls. Noise-overexposures (7 kHz, ½-octave, 97 dB SPL; two hours) were applied to the animal's left ear through hollow ear-bars.

Surgical access of the cochlear nucleus

Animals were anesthetized (4:1 K/X) and placed in a hollow-ear-bar stereotaxic frame (Kopf). Body temperature was regulated (custom-built controller; 38 °C). Anesthetic depth was checked using a toe-pinch, and supplemental anesthesia (0.15 mg of K/X) was administered as required. The AVCN was accessed using established stereotaxic coordinates (Heeringa et al., 2018b).

Single-unit Electrophysiology

In vivo data were recorded using multichannel electrodes (Neuronexus). Voltages were digitized (PZ2-64 pre-amp) and bandpass filtered (300 Hz-3 kHz). Spikes were identified when voltage amplitude crossed 2 standard deviations above the mean. Units were identified by their responses to 65 dB SPL wideband (200 Hz-40 kHz) search stimuli. Neural spike data was analyzed offline using custom-written scripts (Mathworks MATLAB). Spike waveform principle components (PC) were calculated, and single units identified manually by clustering the first three coefficients. Unit-electrode consistency was maintained by clustering all PC coefficients from a given recording location. Timestamps were grouped by cluster into isolated spiketrains.

Putative bushy-cells (N=1111) were identified by their Type 1 or Type 1/3 receptive fields (10 dB steps from 0 to 90 dB SPL; frequencies logarithmically spaced from 2 to 24 kHz in 0.25 octave steps), and primary-like or primary-like-with-notch peri-stimulus time histograms (PSTH) (Blackburn and Sachs, 1989; Winter and Palmer, 1990b; Ingham et al., 2016). Spontaneous activity (>=150 sec) and rate-intensity functions (RIF) to BF-tones and broadband noise (5 dB steps from 0 to 90 dBSPL) were assessed for each bushy cell. Average first-spike latency (FSL) was computed by recording the first-spike timestamp post-stimulus onset for each trial (n=100) during RIFs.

MATLAB Auditory Periphery Model

The Meddis MATLAB Auditory Pathway (MAP) model was used to simulate the conversion of sound pressure into neural spiking by the auditory periphery, auditory nerve and brainstem neurons (Meddis, 2006; Lecluyse et al., 2013). Full technical details of the MAP model are available elsewhere (Meddis et al., 2013). In brief, the MAP model uses a parallel, nonlinear filter bank to simulate ear and basilar membrane sound processing. Filter center-frequencies and tuning were parameterized using guinea pig values (Sumner et al., 2002; Sumner et al., 2003). 150 auditory channels were utilized, with best frequencies (BFs) logarithmically spaced from 200 Hz to 32 kHz. Inner hair cells were modeled as a multistage cascade of coupled differential equations, where the first station converts basilar membrane motion into IHC calcium concentration, while the second relates calcium concentration into release of glutamate vesicles. Auditory nerve fibers (ANFs) fire when a vesicle is released from an IHC, with a 1 ms refractory period. Vesical release rates, and thus ANF firing rates, are related to the calcium clearance time constant τ_{Ca}, where SFR = 91.1 * $\tau_{Ca}^{2.66}$. Spontaneous rates and proportions associated with low, medium and high spontaneous rates found in guinea pigs were used (Tsuji and Liberman, 1997; Bourien et al., 2014).

Cochlear nucleus circuit implementation

Cochlear nucleus and higher-order brainstem neurons were simulated as point neurons, where neural responses are computed using an integrate-and-fire implementation (MacGregor, 1987). Two classes of neurons were implemented: narrowly-tuned primary-like neurons, representing spherical bushy cells (Blackburn and Sachs, 1989; Winter and Palmer, 1990b), and wideband onset neurons, which

represent d-stellate neurons (Winter and Palmer, 1995; Arnott et al., 2004; Campagnola and Manis, 2014). 10x ANFs were simulated for each CN neuron, while 10x CN neurons were simulated for each second-level neuron (Meddis, 2006). Each neuron received ANF timestamps, that was convolved with a double-exponential alpha-function to simulate auditory nerve current release (Meddis, 2006; Clark et al., 2012). Bushy cells receive four ANF inputs from a single BF, while onset neurons receive input from one ANF at each BF. Bushy cells received sharply-tuned alpha-function input with a large amplitude, representing fast ANF dynamics at the bushy-cell endbulb. Onset neurons received broadly-tuned alpha-function input with a smaller amplitude, representing weaker input onto d-stellate neurons (Pressnitzer et al., 2001; Meddis, 2006).

In the MAP model (Meddis, 2006), neuron membrane voltage, ***E(t)***, is calculated as a deviation from resting potential E_{rest}:

$$\frac{dE(t)}{dt} = -\frac{E(t)}{\tau_m} + \alpha_m * I_{BF}(t) - G_k(t) * [E_k - E(t)] + G_{dend} * E_{dend}(t) + G_{wb} * [E(t) - E_{wb}(t)]$$

where τ_m is the membrane time constant, α_m is the cell-ANF coupling, and $I_{BF}(t)$ is the auditory nerve current from an ANF. $G_k(t)$ represents the inhibitory potassium conductance:

$$\frac{dG_k(t)}{dt} = -\frac{G_k(t)}{\tau_{G_k}}$$

τ_{G_k} is the potassium conductance time constant and E_k is the potassium reversal potential. $E_{dend}(t)$ represents non-auditory dendritic input coupled to the neuron through G_{dend}, and is computed as a rectified Gaussian-distributed noise (mean=5mV,

standard deviation=1mV). In this simulation, non-auditory input was assumed to be uncorrelated with auditory input during simulations. G_{wb} is the coupling between simulated bushy cells and wide-frequency auditory input from onset responses. Onset response neuron voltage ($E_{wb}(t)$) was computed following the bushy-cell framework, with onset-unit generating parameters and with G_{dend}, G_{wb} set to 0. For each neuron type, action potentials occur when $E(t) > E_{thresh}$, after which $G_k(t)$ and $E(t)$ are reset to their respective resting potentials and timestamps are recorded. Model equations were solved using a forward-Euler approach.

Hearing loss, putatively resulting in synaptopathy, appears to be a necessary but insufficient condition for tinnitus (Wu et al., 2016) and potentially hyperacusis (Sheldrake et al., 2015). Synaptopathy was simulated by scaling τ_{Ca} for ANF channels with BFs above 8 kHz and low SFR, creating a sloping pattern consistent with our noise-overexposure (Heeringa et al., 2018c). Each channel was reduced from its baseline value at 8 kHz up to X% at 32 kHz:

$$\tau_{Ca}(BF)_{new} = \tau_{Ca}(BF) * (1 - X(BF)\%)$$

To simulate potential bushy-cell mechanisms that could underlie hyperacusis-like neural firing patterns, three parameters were varied, where each parameter represents a different mechanism linked to bushy-cell overexcitation. For each parameter, simulations were performed over a range of values, and a value that resulted in significant changes from default was used. In the first case, ANF input current is related to bushy-cell membrane voltage through double-exponential alpha functions and scaled with α_m. $\alpha_m$was set to 1.0 in the control condition and set to 1.75 in the overexcited case to simulate increased AMPAR counts seen after auditory deprivation (Clarkson et

al., 2016). In the second case, excitatory input from non-auditory sources, reflecting bushy-cell dendritic input, was added to the model. Additional sub-threshold excitatory input will bring bushy-cell membrane voltage closer to threshold, reducing the ANF input required to elicit spiking. G_{dend} was set to 0 in the control condition and set to 1.0 in the overexcited condition, reflecting putative increases in non-auditory glutamatergic activity seen following noise-overexposure (Heeringa et al., 2018c). In the third case, G_{wb}, the coupling between simulated wideband inhibitory neurons and bushy cells, was set to 0.001 in the default case and reduced by half in the disinhibitory case. Reduced inhibitory input should allow the bushy cell membrane to charge faster and fire more often. For each simulation, all other model parameters were held constant, and the over-excited simulation results were compared to the control simulation results.

Auditory Brainstem Response Simulations

To simulate ABR responses, a previously proposed modelling paradigm was used (Schaette and McAlpine, 2011). Tone pips were generated and fed into the model (0.5 ms cos^2 rise/fall times, 5 ms duration, 20 repetitions, 40 dB SPL to 90 dB SPL in 10 dB steps). Frequencies from animal experiments were used. ANF and bushy-cell timestamps were generated in response to these tone pips. An action potential from a simulated Hodgkin-Huxley-parameterized neuron was convolved with the timestamps to simulate volume conduction. The voltage was then summed across all channels and band-pass filtered. Model responses to each tone pip were temporally aligned to the start of each stimulus and averaged. ABR waves 1 and 2 amplitudes and latencies were

manually picked. Root-mean square of the whole ABR waveform was computed using MATLAB *rms* function.

Hyperacusis Index

A Hyperacusis Index (**HI**) was computed for each neuron (simulated and in vivo) as the geometric mean of the unit's 1) average RIF slope at intensities greater than 40 dB SPL and less than 90 dB SPL (MATLAB least-square's fit) and 2) peak RIF value at best frequency from 40 dB SPL to 90 dB SPL.

$$HI = \sqrt{(\ RIF\ Slope * Max(Firing\ Rate))}$$

Statistical Analysis

RIF and LIF slope differences were tested for statistical significance using Analysis of Covariance (MATLAB *aoctool*), with alpha = 0.05. Exponential and linear polynomial fits were calculated using the least-squares algorithm (MATLAB *fit*).

Results

Establishing a baseline model of cochlear output and bushy cell firing

The default Meddis Matlab Auditory Pathway (MAP) model was expanded to include wideband inhibitory d-stellate interneurons (Pressnitzer et al., 2001), non-auditory axo-dendritic input (Heeringa et al., 2018a), and coded using guinea-pig model

parameters (Sumner et al., 2003) (**Fig. 4.1A**). Simulated baseline results were then verified with *in vivo* recordings to establish model accuracy. Simulated bushy cells show the expected primary-like peri-stimulus time histogram (PSTHs) (inset in **Fig. 4.1B**) with a sharp onset firing and fast exponential decay to steady-state, consistent with *in vivo* bushy-cell recordings (inset in **Fig. 4.1C**). Simulated bushy cells show Type-1 and Type-1/3 receptive fields (Shofner and Young, 1985), with strong responses to tones at a best-frequency (heatmap in **Fig. 4.1B**), which is also consistent with *in vivo* recordings (heatmap in **Fig. 4.1C**). Simulated bushy cells exhibit increasing rate-intensity functions (RIFs) to both noise (filled markers; dashed orange lines in **Figs. 4.1E, F**) and BF tones (filled markers; dashed black lines in **Figs. 4.1E, F**), as well as decreasing latency-intensity functions (LIFs) to noise (open markers; solid orange line in **Figs. 4.1E, F**) and BF tone (open markers; solid black lines in **Figs. 4.1E, F**), consistent with *in vivo* recordings.

Simulating putative bushy-cell mechanisms underlying hyperacusis-like neural firing patterns

Following noise-overexposure, bushy cells can show hyperacusis-like neural firing patterns (Chapter III). These neural firing patterns consist of greater-and-steeper RIFs to BF-tones (**Fig. 4.2A**; filled symbols; ANOCOVA; T=18.54, p=1.21e-75) and broadband noise (**Fig. 4.2B**; filled symbols; ANOCOVA; T=15.69, p=1.62e-54) compared to non-exposed controls. Bushy cells in noise-overexposed animals also showed reduced-yet-steeper LIFs to BF-tones (**Fig. 4.2A**; open symbols; ANOCOVA; T=-35.3, p<1.18e-257) and broadband noise (**Fig. 4.2B**; open symbols; ANOCOVA; T=-

27.46, p<2.76e-154) compared to controls. To further quantify bushy-cell excitability, firing rate (FR) was plotted against first-spike latency (FSL), normalized by the peak firing rate, and fit with an exponential function:

$$FR = \alpha * \exp(-\beta * FSL)$$

Excitability is reflected by the steepness of the slope: more excitable neurons will have steeper FR-vs-FSL slopes, which are quantified by an increased value of β. We found that bushy-cells in noise-overexposed animals, when compared to controls, demonstrated steeper FR-vs-FSL fits for BF-tone (mean+/-95%CI: beta[exposed]=0.12+/-0.006, beta[control]=0.09+/-0.012; **Fig. 4.2C**) and broadband noise (mean+/-95%CI: beta[exposed]=0.096+/-0.0049, beta[control]=0.081+/-0.0095; **Fig. 4.2D;** Chapter III). To explain these results, we considered how synaptopathy might influence bushy-cell firing patterns, as well as three potential mechanisms that could result in increased bushy cell excitability *in vivo*.

Synaptopathy appears to be a necessary but insufficient condition for tinnitus (Wu et al., 2016) and potentially hyperacusis (Sheldrake et al., 2015). To simulate synaptopathy, ANF τCa, which regulates spiking threshold, was reduced for low SFR fibers with BFs>=8 kHz, consistent with the pattern demonstrated in guinea pigs following our noise-overexposure paradigm (Heeringa et al., 2018c). The synaptopathy slope from 8 kHz to 32 kHz was increased from 0% in the control condition to 100% in the maximum condition. Slight increases in bushy-cell excitability were seen with synaptopathy losses <=50% (**Fig. 4.3A, B**). However, bushy-cell excitability was significantly reduced with synaptopathy losses greater than 50%. Reductions in bushy-cell excitability at elevated synaptopathy-levels resulted in firing rates and first-spike

latencies far less than seen with *in vivo* data (Chapter III; Winter and Palmer, 1990a). However, as it is unclear how synaptopathy might relate to each potential hyperacusis hypothesis, further simulations did not feature synaptopathy. Moreover, synaptopathy and hearing loss generally occur without hyperacusis or tinnitus (Roberts et al., 2010), suggesting that pathological neural firing is responsible for each condition. Nevertheless, synaptopathy should have a meaningful contribution to eliciting homeostatic processes that underlie tinnitus and/or hyperacusis *in vivo*.

Hypothesis One (H1): bushy cells become more sensitive to auditory-nerve input through increased ANF-soma coupling. Following auditory deprivation, bushy-cell post-synaptic-density (PSD) AMPA receptor counts increase (Clarkson et al., 2016), increasing bushy-cell conductance, thereby leading to faster depolarization and increased bushy-cell firing. To test this hypothesis, the coupling between the simulated ANF and bushy-cell membrane was strengthened relative to the default model. FR-vs-FSL was fit and normalized to its maximum value for a range of BC-to-ANF coupling values (**Fig. 4.4A**), and beta measured for each coupling value (**Fig. 4.4B**). Excitability increased linearly over the range of assessed coupling strengths. In our test simulation, we found that overexcited bushy cells showed steeper RIFs and LIFs in response to BF-tones (**Fig. 4.4C**) and broadband noise (**Fig. 4.4D**), as well as steeper FR vs FSL curves in response to BF-tones (mean+/-95%CI: beta[excite]=0.096+/-0.0038, beta[control]=0.061+/-0.0024; **Fig. 4.4E**) and broadband noise (mean+/-95%CI: beta[excite]=0.098+/-0.0035, beta[control]=0.067+/-0.0027; **Fig. 4.4F**). These findings suggest that enhanced ANF-to-BC coupling contributes the expected neural profile of hyperacusis.

Hypothesis Two (H2): bushy cells become more sensitive to auditory-nerve input through increases in dendritic excitability. Bushy cells receive glutamatergic somatosensory input on their dendrites (Heeringa et al., 2018c; Wu and Shore, 2018), which can modulate bushy-cell firing sensitivity. Following noise-exposure and synaptopathy, the VCN receives increased glutamatergic innervation from non-auditory structures (Heeringa et al., 2018c). Increased glutamatergic somatosensory synapses (Zhou et al., 2007) on bushy-cell dendrites (Heeringa et al., 2018a) could increase bushy-cell firing by increasing sub-threshold temporal summation. To test this hypothesis, excitatory non-auditory dendritic input was added to model bushy-cell neurons. FR-vs-FSL was fit and normalized for a range of somatosensory amplitude values (**Fig. 4.5A**), and beta measured for each coupling value (**Fig. 4.5B**). Bushy-cell excitability increased with increasing amplitude values, but then tended to level off with higher values. In this simulation, we found that compared to controls, over-excited bushy cells showed elevated and steeper RIFs, and reduced but steeper LIFs to BF-tones (**Fig. 4.5C**) and broadband noise (**Fig. 4.5D**). Moreover, consistent with the *in vivo* results, this simulation resulted in steeper firing-rate vs FSL curves in response to BF-tone (mean+/-95%CI: beta[excite]=0.073+/-0.0023, beta[control]=0.063+/-0.0022; **Fig. 4.5E**) and to broadband noise (mean+/-95%CI: beta[excite]=0.078+/-0.0026, beta[control]=0.068+/-0.0031; **Fig. 4.5F**), when compared to controls. These findings suggest that increased non-auditory dendritic input to bushy cells can produce firing patterns consistent with the *in vivo* hyperacusis-like neural pattern.

Hypothesis Three (H3): disinhibition of bushy cells by reduced sound-evoked inhibitory input. Bushy cells receive inhibitory interneuron input, including wideband

inhibition from VCN d-stellate neurons (Wickesberg and Oertel, 1990; Nelken and Young, 1994; Arnott et al., 2004). Noise-overexposure can result in VCN disinhibition, and thus increase evoked firing rates from putative bushy cells (Boettcher and Salvi, 1993). To simulate disinhibitory effects on bushy-cell firing patterns, we reduced the coupling strength from model d-stellate neurons to bushy cells. FR-vs-FSL curves were simulated (**Fig. 4.6A**) and beta-parameter fits were computed for each simulation value (**Fig. 4.6B**). We found an inverse relationship between excitability and the inhibitory coupling strength between d-stellate and bushy cells. In this simulation, we found that disinhibited bushy cells showed elevated-and-steeper RIFs, along with reduced-and-steeper LIFs to BF-tones (**Fig. 4.6C**) and broadband noise (**Fig. 4.6D**). Like H1 and H2, this simulation also resulted in steeper FR-vs-FSL curves in response to BF-tone (mean+/-95%CI: beta[excite]=0.085+/-0.0036, beta[control]=0.063+/-0.0026; **Fig. 4.6E**) and to broadband noise (mean+/-95%CI: beta[excite]=0.087+/-0.0032, beta[control]=0.07+/-0.0034; **Fig. 4.6F**), consistent with the hyperacusis-like neural patterns seen *in vivo* (Chapter III). Interestingly, in contrast to H1 and H2, H3 predicts bushy-cell changes that are smaller in magnitude and restricted to sound intensities greater than ~40 dB SPL.

Reconciling animal and model data

We then quantified the hyperacusis-likeness of bushy-cell evoked firing rate patterns using a neural “Hyperacusis Index” (HI) for each neuron. The HI is equal to the geometric mean of 1) the RIF slope in response to sounds from 40 dB SPL to 90 dB SPL and 2) the peak firing rate of the RIF. We have previously shown that bushy-cell HI

is increased in noise-exposed animals (Chapter III). The *in vivo* recordings show that bushy cells with increased HIs can be further clustered into two groups, those with increased SFR ("cluster 1") or without increased SFR ("cluster 2") (**Fig. 4.7A**). With the model, we simulated the relationship between HI and SFR for each putative hyperacusis mechanism. We found that no individual hypothesis was able to generate both HI-SFR clusters seen *in vivo*. Instead, H1 (increased bushy-cell ANF coupling; **Fig. 4.7B**) and H2 (increased non-auditory input; **Fig. 4.7C**) predict concurrent increases in HI and SFR, consistent with "cluster 1". However, only H3 (representing bushy-cell disinhibition; **Fig. 4.7D**), predicts that HI can increase without increases in SFR, explaining "cluster 2" seen *in vivo*. Taken together, the present results suggest that multiple mechanisms of bushy-cell hyperexcitability are required to reconcile the HI and SFR patterns seen *in vivo.*

Auditory brainstem response alterations in a simulated hyperacusis model

In addition to their putative role in hyperacusis, bushy cells are also the major generators of the auditory brainstem response (ABR). As bushy cells show steepened RIFs and LIFs in the *in vivo* bushy-cell-hyperacusis model, we reasoned that ABRs should likewise be altered in animals with neural hyperacusis patterns. Thus, ABRs should show increased wave-2-5 amplitudes and shorter latencies in noise-exposed animals with neural patterns of hyperacusis. Since ABR W1 amplitudes did not show statistically significant differences between normal and noise-exposed groups and time points (**Fig. 4.8A**), ABR amplitude-intensity functions (AIFs) over all tested frequencies were pooled. We found that mean W2 AIF slopes were elevated in noise-exposed

animals compared to controls (**Fig. 4.8B**; filled markers; ANOCOVA; p=5.01e-9, T=5.96). Furthermore, we found that ABR W2 peak latency (P2)-intensity functions (LIFs) were steeper in noise-exposed animals compared to controls (**Fig. 4.8B**; open markers; ANOCOVA; p=6.44e-38, T=-13.91). To control for sources of variation in ABR recordings, we computed the root-mean-square (RMS) of each ABR waveform, as the RMS is an objective calculation and unambiguous measure of total signal power and is more resistant to filter parameters that can influence ABR-wave amplitude (Boston, 1983). Moreover, the RMS allows us to measure evoked activity from the targets of the bushy cells, which are expected to also show increased excitability in the hyperacusis model. We found that noise-exposed animals show significantly elevated ABR-RMS input-output slopes compared to controls (**Fig. 4.8C**; ANOCOVA; p=8.04e-8, T=5.44).

Reconciling ABR data from animals with bushy-cell simulations

To predict how bushy-cell changes that result in hyperacusis-like neural firing patterns relate to ABR changes, we simulated ABRs using the MAP model following a previously-established framework (Schaette and McAlpine, 2011). The model was configured to simulate H1, H2 and H3 and presented tone-pip ABR stimuli used in animal experiments. Simulated ABR waves 1, 2 amplitudes and latencies, as well as the RMS of the waveform, were measured from 40 to 90 dB SPL in 10 dB steps. We found that H1 (reflecting enhanced ANF-to-BC coupling) predicts slight decreases in W1 amplitude at higher intensities (**Fig. 4.9A**), along with increases in W2 amplitude and large decreases P2 (**Fig. 4.9B**), as well as increases in RMS at all intensities (**Fig. 4.9C**), compared to the control simulation. Similarly, we found that H2 (representing

increased non-auditory input on bushy cells) produced ABRs with slightly reduced W1 (**Fig. 4.10A**) compared to control simulations, steeper W2 AIFs and LIFs compared to simulated controls (**Fig. 4.10B**), and increased RMS at all sound intensities (**Fig. 4.10C**). However, H3 (reflecting disinhibition from wideband d-stellates) does not predict ABR changes seen in noise-exposed animals (**Fig. 4.11**).

Bushy cells show higher sound-evoked firing rates, reduced FSLs, and steeper FR-vs-FSL curves following noise over-exposure compared to controls (Chapter III). We hypothesized that the animals showing the hyperacusis-like neural firing patterns would likewise demonstrate a steeper relationship between W2 amplitude and P2 latency. Consistent with this hypothesis, we found a significant inverse correlation between the W2:W1 amplitude ratio and P2 latency for noise-overexposed animals (**Fig. 4.12A**; Pearson's correlation; r=-0.12, p=0.018) but not for control animals (Pearson's correlation; r=-0.0085, p=0.94). We then simulated these same ABR values in the model. We found that compared to the control simulation, H1 (reflecting enhanced ANF-to-BC coupling) predicted a steeper relationship between W2:W1 amplitude ratio and P2 latency (**Fig. 4.12B**). Similarly, H2 (reflecting increased non-auditory input to the bushy-cell) showed steeper W2:W1 amplitude versus P2 latency slopes compared to control simulations (**Fig. 4.12C**). However, H3 (reflecting disinhibition from d-stellates) did not show steeper W2:W1 amplitude versus P2 latency slope compared to the control simulation (**Fig. 4.12D**).

Figures

Figure 4.1: Comparison of simulated bushy cell responses to *in vivo* recordings. A) Meddis MATLAB Auditory Pathway ventral-cochlear-nucleus circuit schematic, with simulated spherical bushy cells (green) that receive somatic wideband inhibitory input from d-stellate neurons (red), non-auditory dendritic input (gold), and excitatory input from auditory nerve fibers (blue). **B)** Simulated bushy cell receptive field (PSTH insert). **C)** *In vivo* bushy cell receptive field from guinea pig (PSTH insert). **D)** Simulated bushy-cell rate-intensity functions (RIFs; solid lines with filled markers) and latency-intensity functions (LIFs; dashed lines with open markers) in response to broadband noise (orange) and BF tones (black). **E)** *In vivo* guinea pig bushy-cell RIFs and LIFs in response to broadband noise and BF-tones.

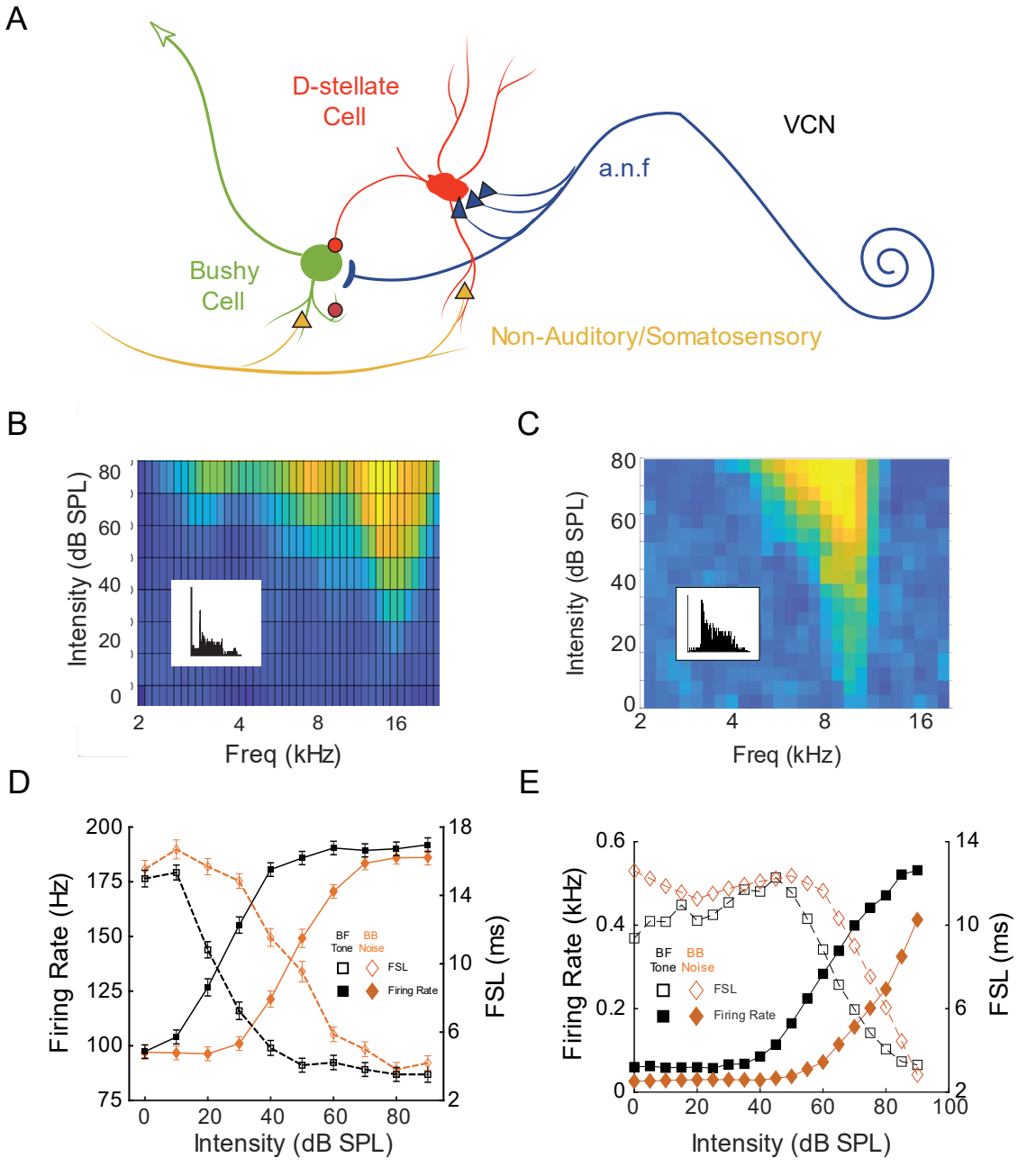

Figure 4.2: Bushy cells *in vivo* exhibit hyperacusis-like neural firing patterns. RIFs (filled symbols; left axis) and LIFs (open symbols; right axis) from bushy cells in noise-exposed animals (purple squares with dashed lines) and non-exposed controls (black diamonds with solid lines) in response to **A)** tones at unit BF and **B)** broadband noise. Firing rate (FR) versus first-spike latency (FSL) and fit exponential functions in response to **C)** BF tones and **D)** broadband noise.

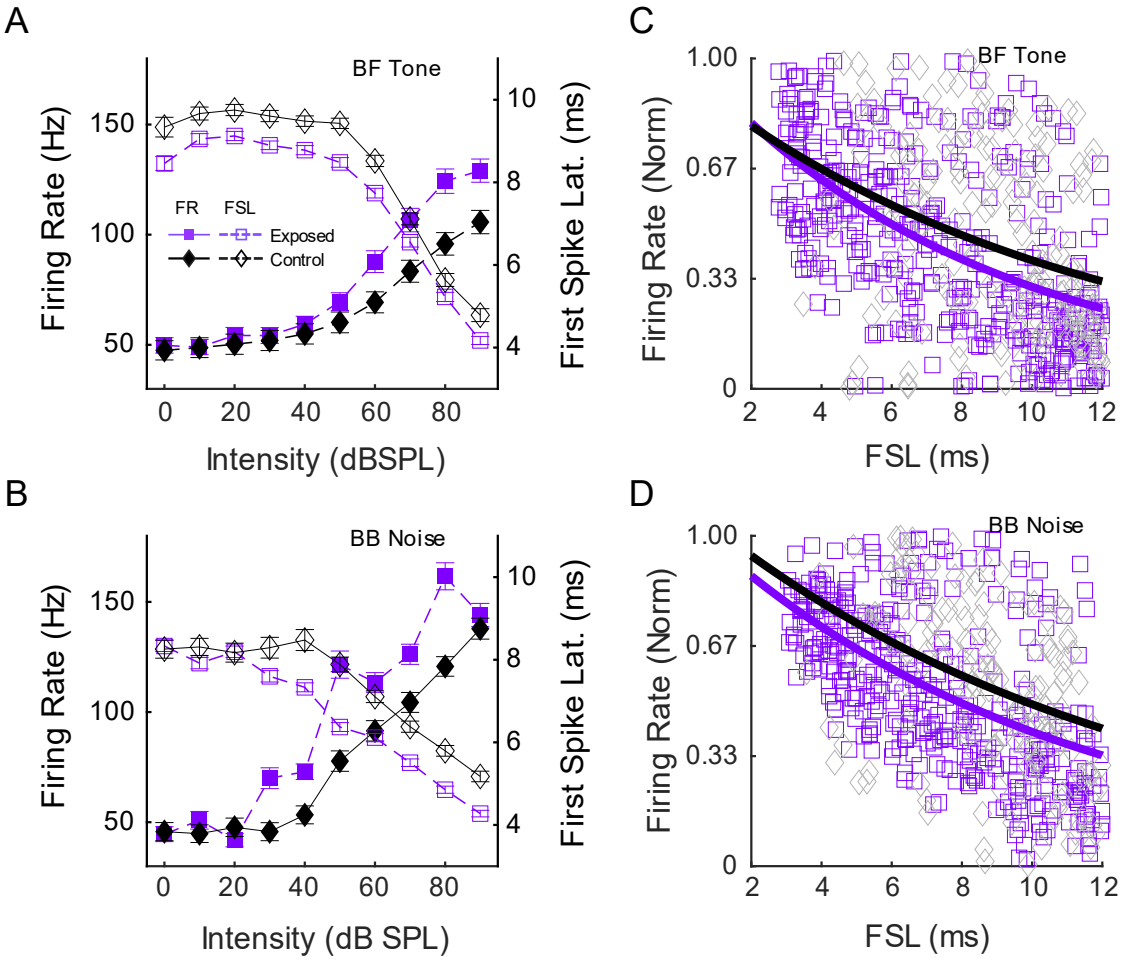

Figure 4.3: Simulated synaptopathy has non-linear effect on bushy-cell excitability. A) FR vs FSL was computed for each synaptopathy value from low SFR units with BFs greater than 8 kHz, where 0 (dark blue open circle) represents no synaptopathy while 1 (gold open circles) represents a gradual synapse loss from 0% at 8 kHz to 100% at 32 kHz. Dashed lines are exponential fits to data. **B)** Beta (mean+/-95%CI), representing bushy-cell excitability, was computed for each BC-to-ANF coupling value.

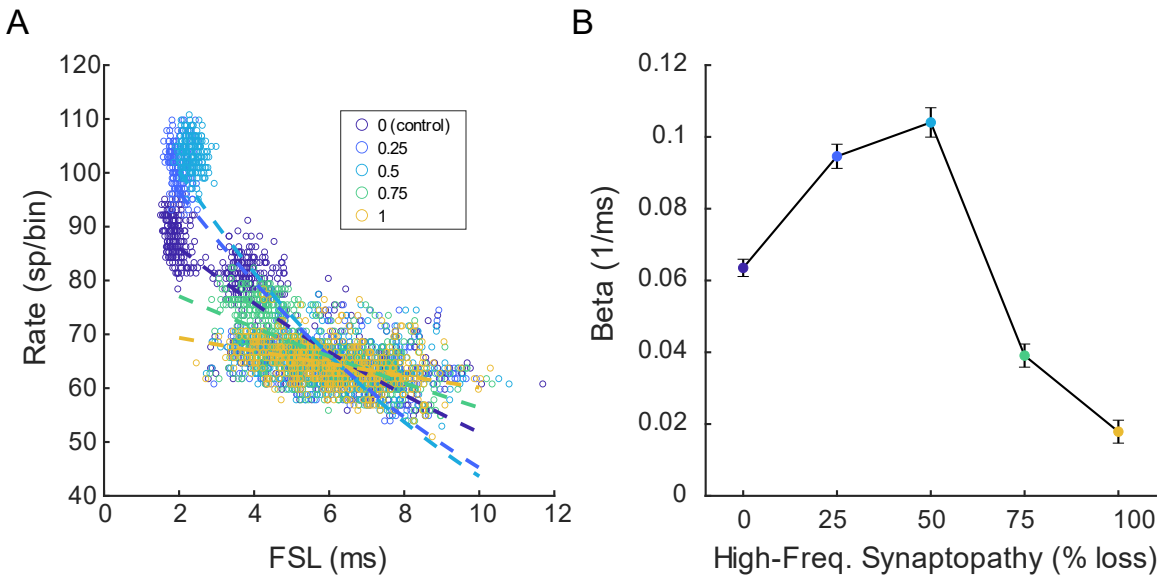

Figure 4.4: Simulating increased ANF-to-BC coupling strength predicts hyperacusis-like bushy-cell firing patterns consistent with *in vivo* results. A) FR and FSL were computed from bushy cells for a range of BC-to-ANF coupling values, where each set of simulation results is represented through a different color (0.5 in dark blue; 2.0 in gold). Trend lines are exponential fits to data. **B)** Beta (mean+/-95%CI), representing bushy-cell excitability, was computed for each BC-to-ANF coupling value. **C)** RIFs (solid lines; filled markers) and LIFs (dashed lines; open markers) to tone for default (black) and over-excited (purple) simulations. **D)** RIFs and LIFs for broadband noise. **E)** FR vs FSL for BF tones, normalized to each simulation's maximum. **F)** FR vs FSL for broadband noise.

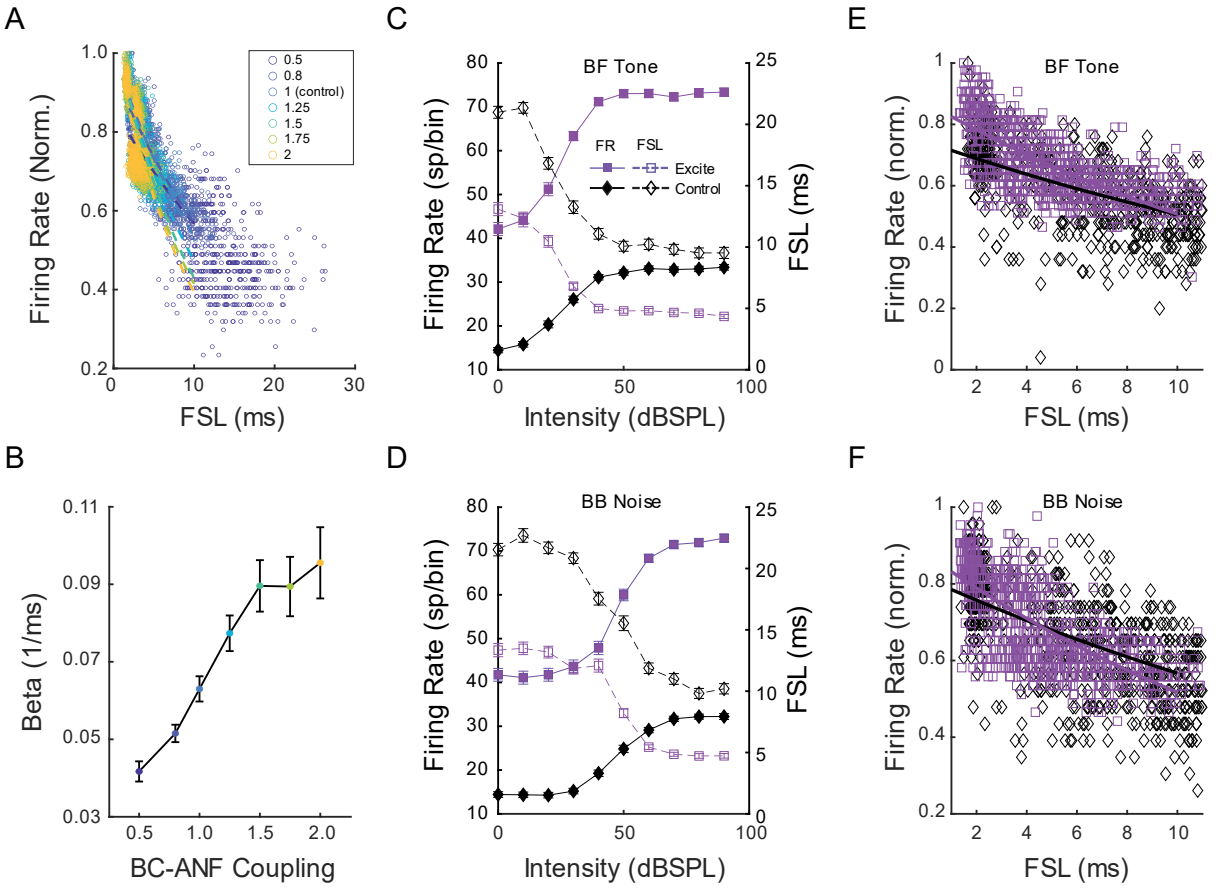

Figure 4.5: Simulating increased non-auditory excitatory input predicts hyperacusis-like bushy-cell firing patterns. A) FR vs FSL and exponential fits from simulated bushy cells for a range of non-auditory dendritic amplitude values. **B)** Beta (mean+/-95%CI) for each simulation value. **C)** RIFs and LIFs to BF tone. **D)** RIFs and LIFs for broadband noise. **E)** FR vs FSL for BF tones. **F)** FR vs FSL for broadband noise.

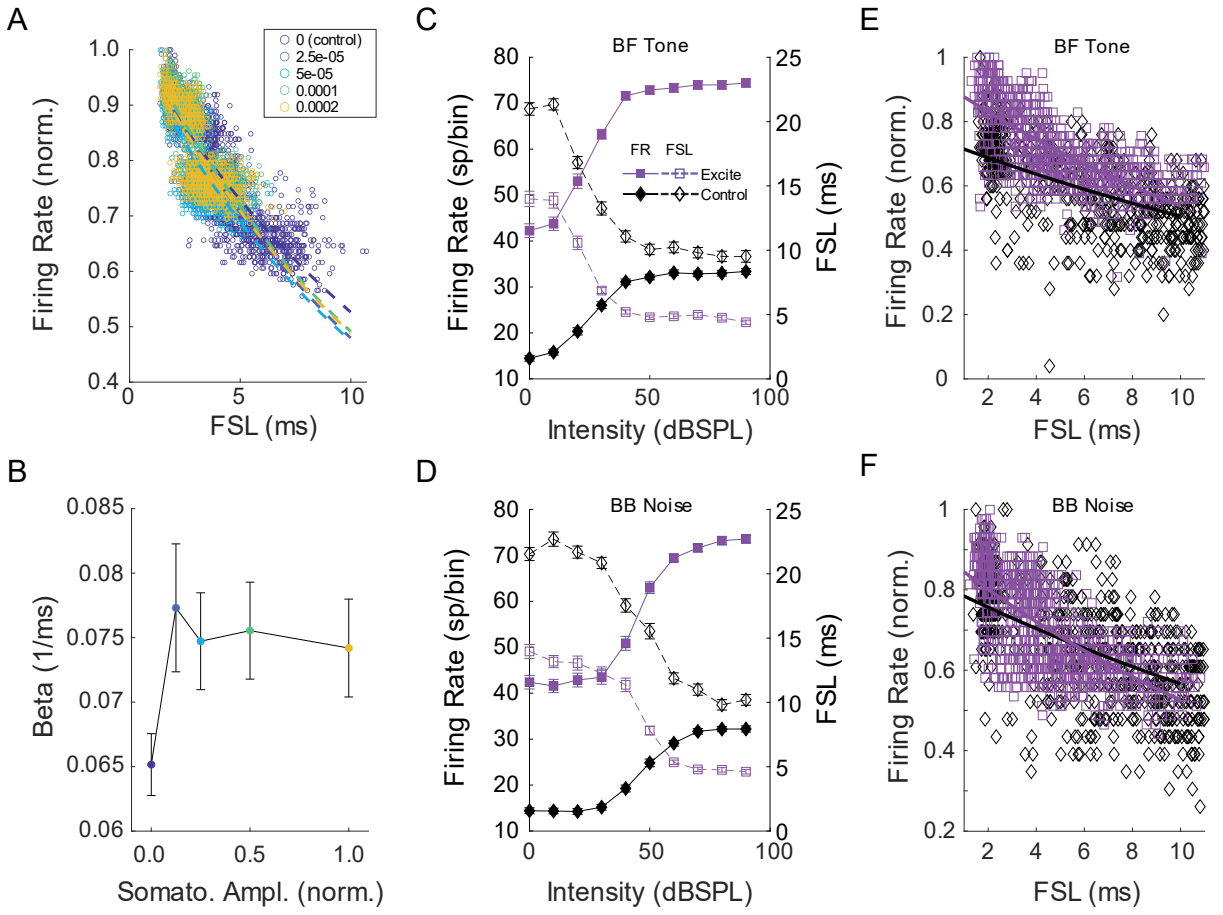

Figure 4.6: Simulating wideband disinhibition predicts hyperacusis-like bushy-cell firing patterns. A) FR vs FSL and exponential fits from bushy cells for a range of wideband inhibition coupling values **B)** Beta (mean+/-95%CI) for each simulation value. **C)** RIFs and LIFs to BF tone. **D)** RIFs and LIFs for broadband noise. **E)** FR vs FSL for BF tones. **F)** FR vs FSL for broadband noise.

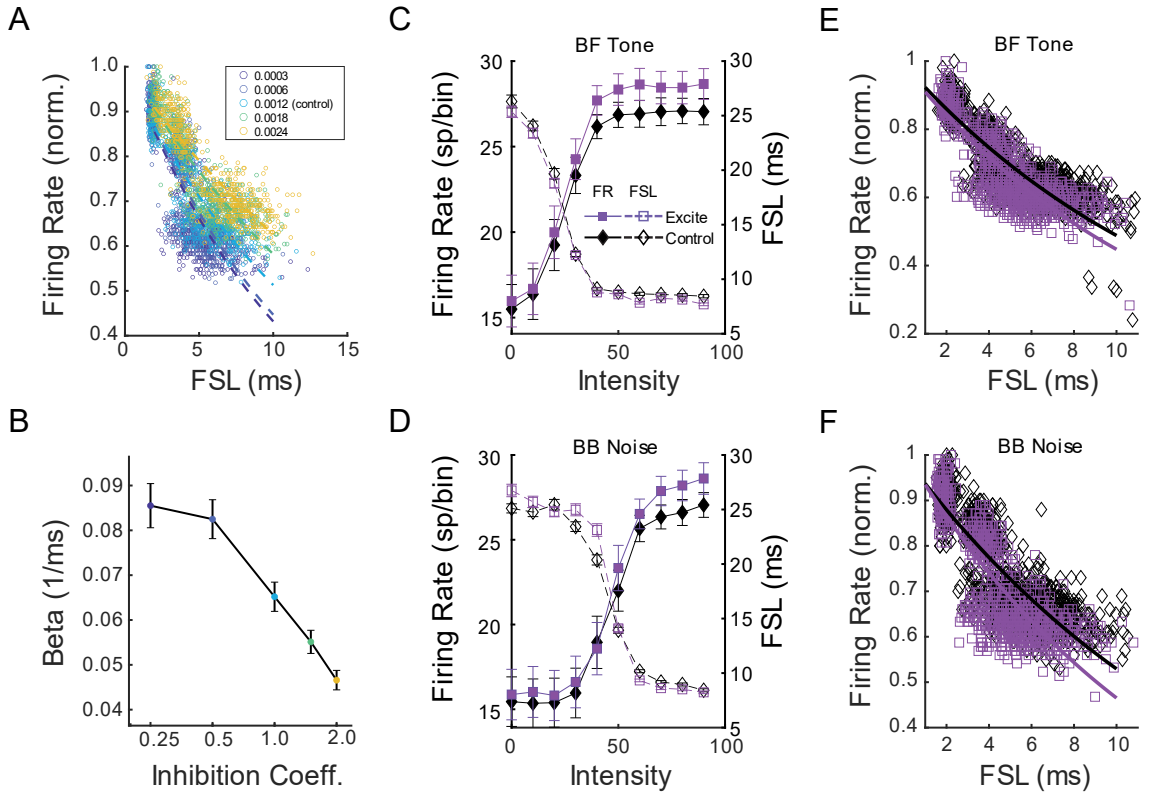

Figure 4.7: Multiple simulated mechanisms required to explain *in vivo* hyperacusis-like firing patterns. A) Bushy cells *in vivo* show distinct clusters of HI and SFR, one with increases in HI and the other with increases in HI and SFR. **B)** H1 (reflecting increased ANF-to-BC coupling strength) predicts correlated increases in SFR and HI, compared to default. **C)** H2 (reflecting increased non-auditory input) predicts correlated increases in SFR and HI. **D)** H3 (reflecting wideband disinhibition) predicts increases in HI without increases in SFR compared to the default case. For all figures, orange line indicates the HI-derived hyperacusis threshold.

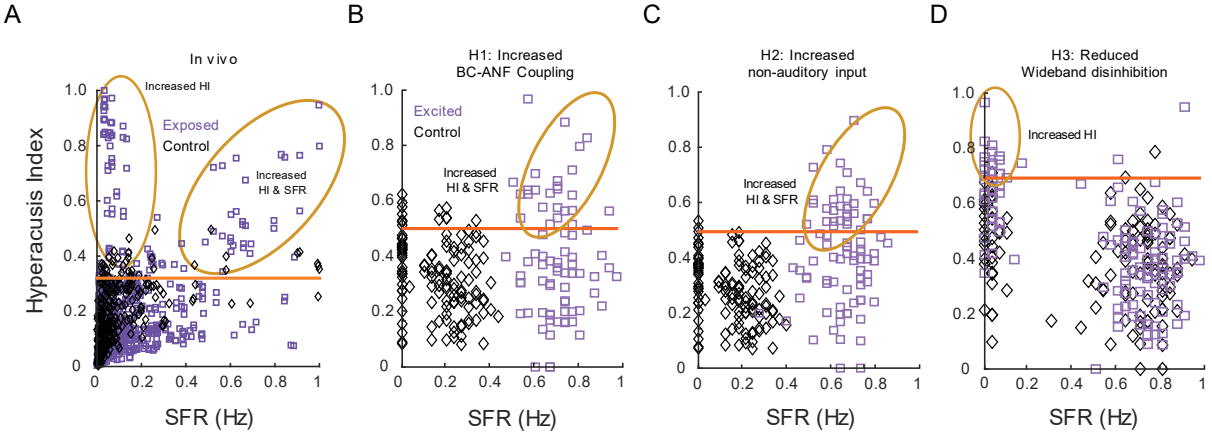

Figure 4.8: Noise-overexposed animals show ABR-Wave-2 changes reflecting hyperexcitable bushy-cells. A) W2 amplitude-intensity functions (AIFs; filled markers) and latency-intensity functions (LIFs; open markers) for noise-exposed (purple dashed lines) and control (black solid lines) animals. **B)** Noise-overexposed animals show greater-and-steeper W2 AIFs as well as lower-and-steeper P2 LIFs compared to controls. **C)** Slope of the root-mean-square (RMS) of the ABR AIF is significantly greater in exposed animals than controls. Data shown are mean+/-SEM.

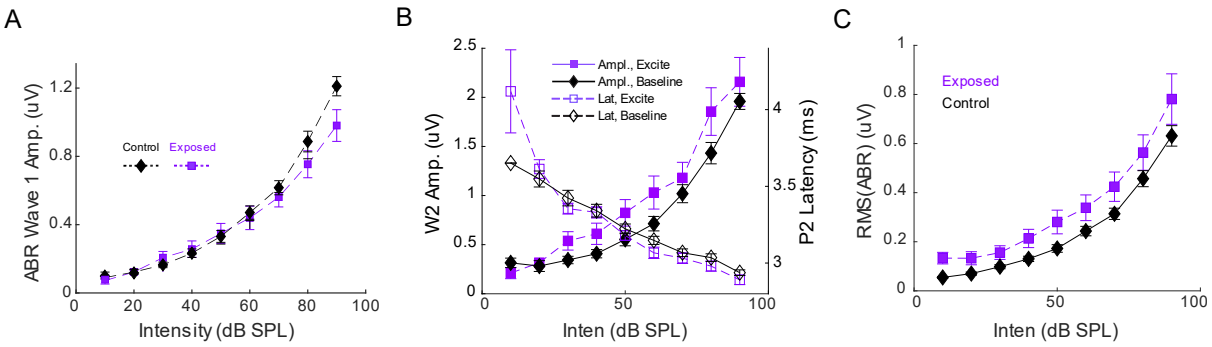

Figure 4.9: Increased ANF-to-BC coupling strength simulation produces ABRs consistent with those from noise-overexposed animals. A) Wave 1 amplitude (solid lines; filled markers) as a function of sound intensity for the over-excited case (purple) compared to controls (black). **B)** Wave 2 amplitude (solid lines; filled markers) and latency (dashed lines; open markers) as a function of intensity for the over-excited case (purple) compared to the controls case (black). **C)** ABR RMS as a function of intensity for the over-excited case (purple) compared to the controls case (black).

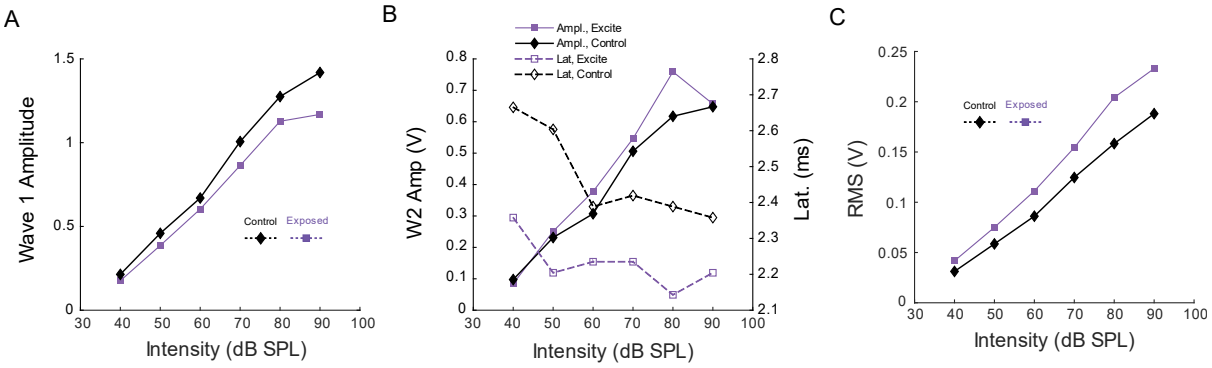

Figure 4.10: Increased non-auditory activation simulation produces ABRs consistent with ABRs from noise-overexposed animals. A) Wave 1 amplitude (solid lines; filled markers) as a function of sound intensity for the over-excited case (purple) compared to controls (black). **B)** Wave 2 amplitude (solid lines; filled markers) and latency (dashed lines; open markers) as a function of intensity for the over-excited case (purple) compared to the controls (black). **C)** ABR RMS as a function of intensity for the over-excited simulation (purple) compared to the control simulation (black).

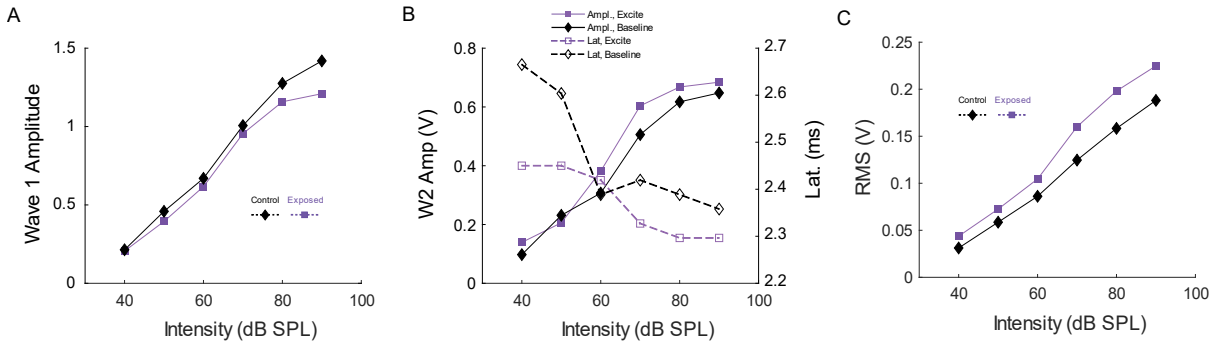

Figure 4.11: Wideband disinhibition simulation does not produce ABRs consistent with those from noise-overexposed animals. A) Wave 1 amplitude (solid lines; filled markers) as a function of sound intensity for the over-excited case (purple) compared to controls (black). **B)** Wave 2 amplitude (solid lines; filled markers) and latency (dashed lines; open markers) as a function of intensity for the over-excited case (purple) compared to the controls (black). **C)** ABR RMS as a function of intensity for the over-excited simulation (purple) compared to the control simulation (black).

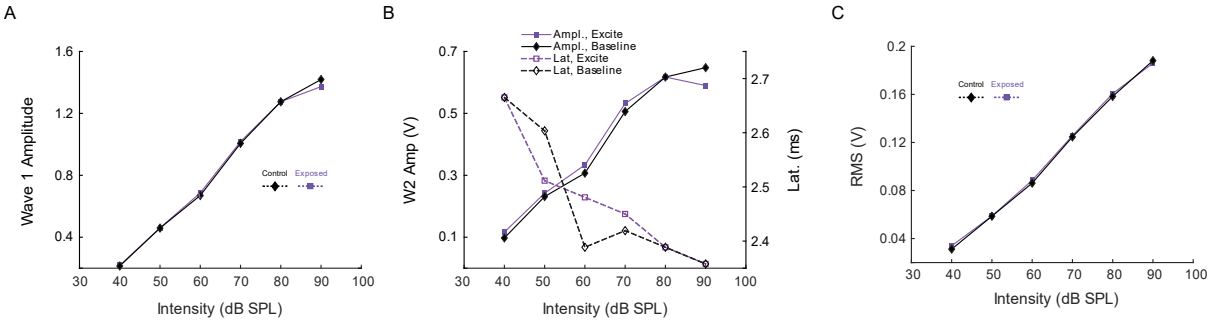

Figure 4.12: ABR W2:W1 amplitude versus P2 latency reflects bushy-cell excitation. A) W2:W1 amplitude ratio plotted against P2 latency is significantly steeper for noise-overexposed animals (purple) than for non-exposed controls (black). **B)** H1 (reflecting increased ANF-to-BC coupling strength) predicts that ABRs will show increased W2:W1 amplitude versus P2 latency slopes (purple) compared to controls (black). **C)** H2 (reflecting increased non-auditory dendritic input) predicts that ABRs will show increased W2:W1 amplitude versus P2 latency slopes (purple) compared to controls (black). **D)** H3 (reflecting wideband disinhibition) predicts that ABRs will show similar W2:W1 amplitude versus P2 latency slopes (purple) compared to controls (black).

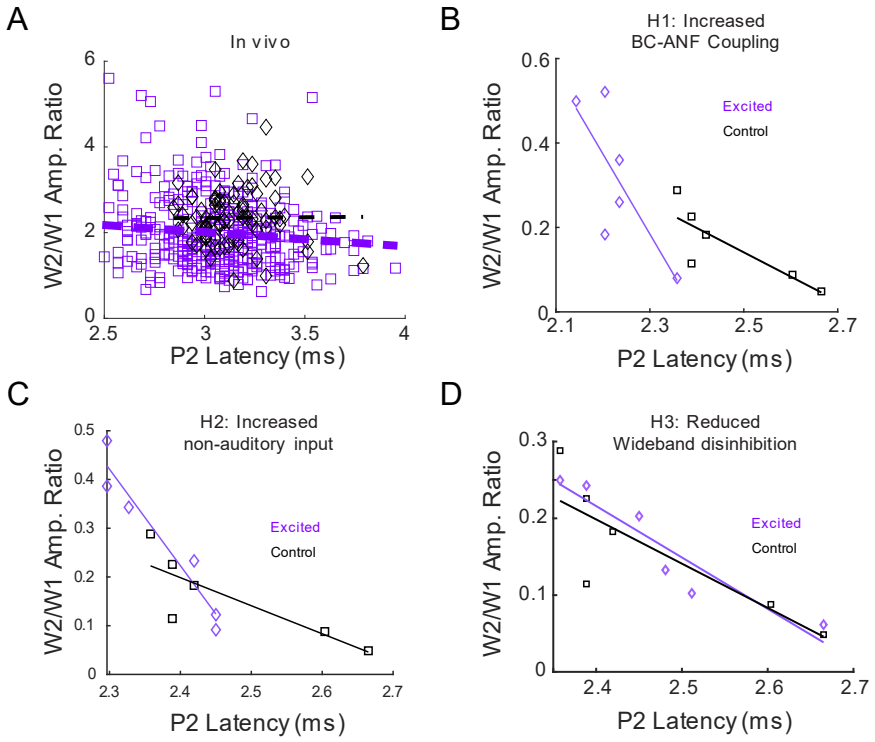

Discussion

In this study, we tested several competing hypotheses that could underlie hyperacusis-like neural firing patterns found in VCN bushy cells. We found that glutamatergic excitation and glycinergic disinhibition independently result in elevated-and-steeper RIFs, reduced-and-steeper LIFs, and steeper FR-vs-FSL curves,

consistent with the *in vivo* results. However, no single hypothesis predicted elevated HI with and without increased SFR. Instead, multiple mechanisms of increased bushy-cell excitation were required to explain the *in vivo* findings. Moreover, we found that noise-overexposure produces ABR-wave amplitude and latency enhancements in animals also showing increases in bushy-cell excitability. Interestingly, the glycinergic disinhibition hypothesis (H3) predicted neither enhanced ABR amplitudes nor reduced latencies, while the glutamatergic excitation hypotheses (H1, H2) did.

Mechanisms underlying increased bushy-cell excitability

In H1, bushy-cell excitability driven by ANF input was enhanced through increased coupling between the auditory nerve fibers and the bushy cell. In this simulation, ANF input depolarized the bushy-cell membrane faster, leading to more spiking and reduced first-spike-latencies, consistent with *in vivo* RIFs and LIFs. H1 also predicted that bushy-cells will show increased sensitivity to spontaneous firing from ANFs, leading to increased SFR, consistent with the simulated results and *in vivo* cluster 1. Moreover, H1 produced ABRs consistent with the *in vivo* ABRs, which showed increased W2 amplitudes, lower P2 latencies and increased RMS values.

Unlike in H1, in H2, bushy-cell excitability was not directly increased, but instead increased indirectly through non-auditory excitatory dendritic input. We found that additional depolarizing input, though uncorrelated with auditory input, increased the probability of bushy-cell spiking by raising the bushy-cell's membrane potential. Raising the membrane potential effectively lowered the spike threshold, allowing pre-synaptic

auditory input to more readily depolarize the bushy cell, for both spontaneous and sound-driven activity. As a result, H2 predicted increases in both HI and SFR, thereby explaining the first HI-SFR cluster seen *in vivo*. This model simulation suggested that sufficiently-strong, non-auditory input arising from the somatosensory projections to bushy cells, could depolarize the bushy cell independently of auditory activity. Previous studies have shown that unimodal electrical stimulation of the spinal trigeminal nucleus can elicit bushy-cell spiking (Heeringa et al., 2018a), which in principle is consistent with the present model simulation. Moreover, if somatosensory stimulation were to reliably precede sound-driven activity, the bushy cell would respond more to the sound stimulation. Indeed, electrical stimulation preceding sound-stimulation has been shown to enhance bushy-cell phase-locking to amplitude-modulated stimuli (Heeringa et al., 2018a). The present simulation suggested that somatosensory stimulation, when in-phase with an auditory stimulus, would enhance bushy-cell firing. Moreover, this simulation predicts that electrical stimulation presented out-of-phase relative to sound simulation should result in reduced phase-locking; future studies are required to verify this prediction.

In H3, bushy-cell excitability was predicted to be increased by reducing glycine-driven inhibition from wideband d-stellate neurons. While this simulation produced hyperacusis-like neural firing patterns in bushy cells, it was the only simulation that could predict increases in HI without corresponding increases in SFR, thereby explaining the second HI-SFR cluster shown *in vivo.* In this simulation, increased bushy-cell excitability was predicted to occur in response to sound-intensities above 40 dB SPL. This finding is consistent with previous studies on bushy-cell inhibition by d-stellate

cells, which suggest that the threshold for sound-evoked inhibition is ~20 dB SPL, with stronger inhibition occurring at increased sound intensities (Kuenzel et al., 2011). Moreover, synaptic delays between bushy cells and d-stellate neurons suggest that sound-evoked inhibition is unlikely to affect the bushy cell onset response, but instead would have a stronger influence on the steady-state response, consistent with previously published studies on bushy-cell inhibition (Xie and Manis, 2013). Thus, this hypothesis predicted that ABRs will be unaffected in subjects with disinhibition-driven hyperacusis. However, not all humans with hyperacusis and/or tinnitus necessarily show ABR wave amplitude enhancements (Gu et al., 2012). The results of H3 simulations suggest a potential mechanism for hyperacusis without ABR wave amplitude enhancements. Given that inhibition should have a greater effect on the steady-state bushy-cell response, responses to stimuli with a longer duration than those used to generate the ABR, would likely be enhanced in this hyperacusis hypothesis. Continuous amplitude-modulated signals can evoke frequency-following responses (FFR), which could be another electrical potential to investigate in this regard, as FFR measurements average out transient signals like the ABR.

Hyperacusis subtypes

Hyperacusis-like neural firing patterns were divided into two clusters, those with, or without, increases in SFR. These clusters were explained by two classes of mechanisms, one arising from increases in glutamate-driven excitability (H1, H2) and the other arising from reductions in glycine-driven inhibition (H3). Each class of mechanisms resulted in separate patterns of ABR alterations. ABR enhancements,

consisting of W2 amplitude increases, P2 latency reductions and RMS increases, were predicted by hypotheses relating to glutamate-driven increased excitation, and not glycine-driven disinhibition. We propose that this distinction could result in hyperacusis subtypes. The first subtype, hyperacusis-with-ABR-enhancements, arises from increases in glutamate-driven excitation, while the second subtype, hyperacusis-without-ABR-enhancements, arises from glycine-driven disinhibition. Further, we predict that these subtypes of hyperacusis would respond to different therapies. Excitatory hyperacusis could be treated with drugs that dampen excitatory activity, while disinhibition hyperacusis is more likely to respond to drugs that enhance inhibitory activity. We also predict that the hyperacusis-subtypes will be accompanied by different disorders. H1 (reflecting increases in bushy-cell ANF coupling) and H2 (reflecting increased non-auditory excitatory input) predict that bushy cells will show increases in sound-evoked activity and SFR, which may result in more or worse tinnitus. Indeed, other studies have shown that subjects with hyperacusis-and-tinnitus report worse tinnitus than subjects with only tinnitus (Hebert et al., 2013; Schecklmann et al., 2014).

Future studies

The proposed hyperacusis hypotheses were derived from previously-published studies on bushy cells following hearing loss. However, no studies to date have examined bushy-cell firing in animals with behaviorally-verified hyperacusis. We predict that bushy cells in animals with behaviorally-verified hyperacusis will exhibit the neural firing patterns demonstrated in these studies. In animals with hyperacusis, *in vitro* recordings could be used to measure bushy-cell membrane resistance, time constants

and spiking thresholds, while *in vivo* recordings could examine d-stellate inhibition relative to bushy-cell firing patterns. Moreover, future studies could measure AMPA-receptor counts, or glycinergic and glutamatergic changes in animals with hyperacusis, and relate changes to ABR wave amplitudes.

In humans with hyperacusis, we predict that future studies will demonstrate the existence of hyperacusis subtypes. Moreover, bushy-cells are the principal relay neurons involved in signaling interaural time and level differences (ITD, ILD) (Brand et al., 2002; Park et al., 2004; Grothe et al., 2010), which are essential for computing the location of a sound-source in the horizontal plane. Thus, humans with hyperacusis may show ITD and ILD differences, which could be used to develop an objective diagnostic tool for hyperacusis.

Limitations

Concurrent bushy-cell and ABR recordings, which could directly relate bushy-cell firing to the ABR (Melcher and Kiang, 1996), were not performed, nor were recordings from other cochlear nucleus cell types. Furthermore, not all cochlear nucleus cell types are incorporated into the model. For example, the default model bushy-cell parameterization most accurately reflects the spherical type, which have morphological and cellular differences compared to globular bushy cells that may result in ABR waveform alterations (Melcher et al., 1996; Melcher and Kiang, 1996). Bushy-cell dendritic electrophysiology is not well characterized in the literature, so more *in vitro* studies are required before this mechanism can be fully characterized. Moreover, the

MAP model bushy-cells do not incorporate multiple types of inhibitory channels. Particularly, Kv1.1 low-voltage-gated, rapid-acting potassium channels found in bushy cells can have a strong modulatory influence on membrane summation (Oertel et al., 2008) and are essential for encoding microsecond-range temporal precision (Gittelman and Tempel, 2006). Finally, parameter values in the simulation were varied one-at-a-time. We anticipate that multiple parameters interacting with each other also could produce some of the results seen here, though at differing value ranges or with non-linear effects.

BIBLIOGRAPHY

Altman NS (1992) An introduction to kernel and nearest-neighbor nonparametric regression. The American Statistician 46:10.

Anderson H, Wedenberg E (1965) A new Method for Hearing Tests in the Guinea Pig. Acta Oto-Laryngologica 60.

Arnott RH, Wallace MN, Shackleton TM, Palmer AR (2004) Onset neurones in the anteroventral cochlear nucleus project to the dorsal cochlear nucleus. J Assoc Res Otolaryngol 5:153-170.

Axelsson A, Ringdahl A (1989) Tinnitus—a study of its prevalence and characteristics. British journal of audiology 23:53-62.

Baguley DM (2003) Hyperacusis. J R Soc Med 96:582-585.

Basura GJ, Koehler SD, Shore SE (2015) Bimodal stimulus timing-dependent plasticity in primary auditory cortex is altered after noise exposure with and without tinnitus. J Neurophysiol 114:3064-3075.

Bauer CA, Brozoski TJ, Rojas R, Boley J, Wyder M (1999) Behavioral model of chronic tinnitus in rats. Otolaryngol Head Neck Surg 121:457-462.

Bauer CA, Turner JG, Caspary DM, Myers KS, Brozoski TJ (2008) Tinnitus and inferior colliculus activity in chinchillas related to three distinct patterns of cochlear trauma. J Neurosci Res 86:2564-2578.

Berger JI, Coomber B, Shackleton TM, Palmer AR, Wallace MN (2013) A novel behavioural approach to detecting tinnitus in the guinea pig. J Neurosci Methods 213:188-195.

Bi GQ, Poo MM (1998) Synaptic modifications in cultured hippocampal neurons: dependence on spike timing, synaptic strength, and postsynaptic cell type. J Neurosci 18:10464-10472.

Biederlack J, Castelo-Branco M, Neuenschwander S, Wheeler DW, Singer W, Nikolic D (2006) Brightness induction: rate enhancement and neuronal synchronization as complementary codes. Neuron 52:1073-1083.

Blackburn CC, Sachs MB (1989) Classification of unit types in the anteroventral cochlear nucleus: PST histograms and regularity analysis. J Neurophysiol 62:1303-1329.

Bledsoe SC, Jr., Koehler S, Tucci DL, Zhou J, Le Prell C, Shore SE (2009) Ventral cochlear nucleus responses to contralateral sound are mediated by commissural and olivocochlear pathways. J Neurophysiol 102:886-900.

Boettcher FA, Salvi RJ (1993) Functional changes in the ventral cochlear nucleus following acute acoustic overstimulation. J Acoust Soc Am 94:2123-2134.

Boston JR (1983) Effects of Digital Filtering on the Waveform and Peak Parameters of the Auditory Brainstem Response. Journal of Clinical Engineering 8.

Bourien J, Tang Y, Batrel C, Huet A, Lenoir M, Ladrech S, Desmadryl G, Nouvian R, Puel JL, Wang J (2014) Contribution of auditory nerve fibers to compound action potential of the auditory nerve. J Neurophysiol 112:1025-1039.

Bourk TR (1976) Electrical responses of neural units in the anteroventral cochlear nucleus of the cat.

Brand A, Behrend O, Marquardt T, McAlpine D, Grothe B (2002) Precise inhibition is essential for microsecond interaural time difference coding. Nature 417:543-547.
Brotherton H, Plack CJ, Maslin M, Schaette R, Munro KJ (2015) Pump up the volume: could excessive neural gain explain tinnitus and hyperacusis? Audiol Neurootol 20:273-282.
Brown GJ, Ferry RT, Meddis R (2010) A computer model of auditory efferent suppression: implications for the recognition of speech in noise. J Acoust Soc Am 127:943-954.
Brozoski TJ, Bauer CA (2016) Animal models of tinnitus. Hear Res 338:88-97.
Campagnola L, Manis PB (2014) A map of functional synaptic connectivity in the mouse anteroventral cochlear nucleus. J Neurosci 34:2214-2230.
Caspary DM, Backoff PM, Finlayson PG, Palombi PS (1994) Inhibitory inputs modulate discharge rate within frequency receptive fields of anteroventral cochlear nucleus neurons. J Neurophysiol 72:2124-2133.
Cazals Y, Horner KC, Huang ZW (1998) Alterations in average spectrum of cochleoneural activity by long-term salicylate treatment in the guinea pig: a plausible index of tinnitus. J Neurophysiol 80:2113-2120.
Chen G, Lee C, Sandridge SA, Butler HM, Manzoor NF, Kaltenbach JA (2013) Behavioral evidence for possible simultaneous induction of hyperacusis and tinnitus following intense sound exposure. J Assoc Res Otolaryngol 14:413-424.
Chen GD, Jastreboff PJ (1995) Salicylate-induced abnormal activity in the inferior colliculus of rats. Hear Res 82:158-178.
Clark NR, Brown GJ, Jurgens T, Meddis R (2012) A frequency-selective feedback model of auditory efferent suppression and its implications for the recognition of speech in noise. J Acoust Soc Am 132:1535-1541.
Clarkson C, Antunes FM, Rubio ME (2016) Conductive Hearing Loss Has Long-Lasting Structural and Molecular Effects on Presynaptic and Postsynaptic Structures of Auditory Nerve Synapses in the Cochlear Nucleus. J Neurosci 36:10214-10227.
Crifo S, Antonelli M (1972) [Ig G,A,M in the nasal secretion in cystic fibrosis]. Folia Allergol (Roma) 19:126-128.
Dau T, Wegner O, Mellert V, Kollmeier B (2000) Auditory brainstem responses with optimized chirp signals compensating basilar-membrane dispersion. J Acoust Soc Am 107:1530-1540.
Dehmel S, Eisinger D, Shore SE (2012a) Gap prepulse inhibition and auditory brainstem-evoked potentials as objective measures for tinnitus in guinea pigs. Front Syst Neurosci 6:42.
Dehmel S, Pradhan S, Koehler S, Bledsoe S, Shore S (2012b) Noise overexposure alters long-term somatosensory-auditory processing in the dorsal cochlear nucleus--possible basis for tinnitus-related hyperactivity? J Neurosci 32:1660-1671.
Doucet JR, Ryugo DK (2006) Structural and functional classes of multipolar cells in the ventral cochlear nucleus. The anatomical record Part A, Discoveries in molecular, cellular, and evolutionary biology 288:331-344.
Doucet JR, Ross AT, Gillespie MB, Ryugo DK (1999) Glycine immunoreactivity of multipolar neurons in the ventral cochlear nucleus which project to the dorsal cochlear nucleus. J Comp Neurol 408:515-531.
Eggermont JJ, Roberts LE (2015) Tinnitus: animal models and findings in humans. Cell Tissue Res 361:311-336.
Engel AK, Singer W (2001) Temporal binding and the neural correlates of sensory awareness. Trends Cogn Sci 5:16-25.
Engineer ND, Riley JR, Seale JD, Vrana WA, Shetake JA, Sudanagunta SP, Borland MS, Kilgard MP (2011) Reversing pathological neural activity using targeted plasticity. Nature 470:101-104.

Fendt M, Li L, Yeomans JS (2001) Brain stem circuits mediating prepulse inhibition of the startle reflex. Psychopharmacology (Berl) 156:216-224.
Fournier P, Hebert S (2013) Gap detection deficits in humans with tinnitus as assessed with the acoustic startle paradigm: does tinnitus fill in the gap? Hear Res 295:16-23.
Francis HW, Manis PB (2000) Effects of deafferentation on the electrophysiology of ventral cochlear nucleus neurons. Hear Res 149:91-105.
Friedman JH, Bentely, Jon L., Finkel, Raphael A. (1977) An algorithm for finding best matches in logarithmic expected time. ACM Transactions on Mathematical Software 3:209-226.
Galazyuk A, Hebert S (2015) Gap-Prepulse Inhibition of the Acoustic Startle Reflex (GPIAS) for Tinnitus Assessment: Current Status and Future Directions. Front Neurol 6:88.
Gittelman JX, Tempel BL (2006) Kv1.1-containing channels are critical for temporal precision during spike initiation. J Neurophysiol 96:1203-1214.
Gomez-Nieto R, Rubio ME (2009) A bushy cell network in the rat ventral cochlear nucleus. J Comp Neurol 516:241-263.
Gomez-Nieto R, Rubio ME (2011) Ultrastructure, synaptic organization, and molecular components of bushy cell networks in the anteroventral cochlear nucleus of the rhesus monkey. Neuroscience 179:188-207.
Grothe B, Pecka M, McAlpine D (2010) Mechanisms of sound localization in mammals. Physiological reviews 90:983-1012.
Gu JW, Herrmann BS, Levine RA, Melcher JR (2012) Brainstem auditory evoked potentials suggest a role for the ventral cochlear nucleus in tinnitus. J Assoc Res Otolaryngol 13:819-833.
Gu JW, Halpin CF, Nam EC, Levine RA, Melcher JR (2010) Tinnitus, diminished sound-level tolerance, and elevated auditory activity in humans with clinically normal hearing sensitivity. J Neurophysiol 104:3361-3370.
Guitton MJ, Caston J, Ruel J, Johnson RM, Pujol R, Puel JL (2003) Salicylate induces tinnitus through activation of cochlear NMDA receptors. J Neurosci 23:3944-3952.
Haenggeli CA, Pongstaporn T, Doucet JR, Ryugo DK (2005) Projections from the spinal trigeminal nucleus to the cochlear nucleus in the rat. J Comp Neurol 484:191-205.
Han VZ, Grant K, Bell CC (2000) Reversible associative depression and nonassociative potentiation at a parallel fiber synapse. Neuron 27:611-622.
Hayes SH, Radziwon KE, Stolzberg DJ, Salvi RJ (2014) Behavioral models of tinnitus and hyperacusis in animals. Front Neurol 5:179.
Hebert S, Fournier P, Norena A (2013) The auditory sensitivity is increased in tinnitus ears. J Neurosci 33:2356-2364.
Heeringa AN, Wu C, Shore SE (2018a) Multisensory Integration Enhances Temporal Coding in Ventral Cochlear Nucleus Bushy Cells. J Neurosci 38:2832-2843.
Heeringa AN, Wu C, Shore SE (2018b) Multisensory Integration Enhances Temporal Coding in Ventral Cochlear Nucleus Bushy Cells. J Neurosci.
Heeringa AN, Wu C, Chung C, West M, Martel D, Liberman L, Liberman MC, Shore SE (2018c) Glutamatergic Projections to the Cochlear Nucleus are Redistributed in Tinnitus. Neuroscience 391:91-103.
Hickox AE, Liberman MC (2014) Is noise-induced cochlear neuropathy key to the generation of hyperacusis or tinnitus? J Neurophysiol 111:552-564.
Holt GR, Koch C (1999) Electrical interactions via the extracellular potential near cell bodies. J Comput Neurosci 6:169-184.
Ingham NJ, Itatani N, Bleeck S, Winter IM (2016) Enhancement of forward suppression begins in the ventral cochlear nucleus. Brain Res 1639:13-27.

Itoh K, Kamiya H, Mitani A, Yasui Y, Takada M, Mizuno N (1987) Direct projections from the dorsal column nuclei and the spinal trigeminal nuclei to the cochlear nuclei in the cat. Brain Res 400:145-150.
Jastreboff PJ, Brennan JF, Coleman JK, Sasaki CT (1988) Phantom auditory sensation in rats: an animal model for tinnitus. Behav Neurosci 102:811-822.
Jin YM, Godfrey DA (2006) Effects of cochlear ablation on muscarinic acetylcholine receptor binding in the rat cochlear nucleus. J Neurosci Res 83:157-166.
Jin YM, Godfrey DA, Wang J, Kaltenbach JA (2006) Effects of intense tone exposure on choline acetyltransferase activity in the hamster cochlear nucleus. Hear Res 216-217:168-175.
Kalappa BI, Brozoski TJ, Turner JG, Caspary DM (2014a) Single unit hyperactivity and bursting in the auditory thalamus of awake rats directly correlates with behavioural evidence of tinnitus. J Physiol 592:5065-5078.
Kalappa BI, Brozoski TJ, Turner JG, Caspary DM (2014b) Single unit hyperactivity and bursting in the auditory thalamus of awake rats directly correlates with behavioural evidence of tinnitus. J Physiol 592:5065-5078.
Kanold PO, Young ED (2001) Proprioceptive information from the pinna provides somatosensory input to cat dorsal cochlear nucleus. J Neurosci 21:7848-7858.
Kanold PO, Manis PB (2005) Encoding the timing of inhibitory inputs. J Neurophysiol 93:2887-2897.
Keine C, Rubsamen R (2015) Inhibition shapes acoustic responsiveness in spherical bushy cells. J Neurosci 35:8579-8592.
Keine C, Rubsamen R, Englitz B (2017) Signal integration at spherical bushy cells enhances representation of temporal structure but limits its range. eLife 6.
Knudson IM, Melcher JR (2016) Elevated Acoustic Startle Responses in Humans: Relationship to Reduced Loudness Discomfort Level, but not Self-Report of Hyperacusis. J Assoc Res Otolaryngol 17:223-235.
Koehler S, Shore S (2013a) Stimulus Timing-Dependent Plasticity in Dorsal Cochlear Nuclues is altered in tinnitus. Journal of Neuroscience 33(50):19647-19656.
Koehler SD, Shore SE (2013b) Stimulus-timing dependent multisensory plasticity in the guinea pig dorsal cochlear nucleus. PLoS One 8:e59828.
Koehler SD, Shore SE (2013c) Stimulus timing-dependent plasticity in dorsal cochlear nucleus is altered in tinnitus. J Neurosci 33:19647-19656.
Kraus KS, Ding D, Zhou Y, Salvi RJ (2009) Central auditory plasticity after carboplatin-induced unilateral inner ear damage in the chinchilla: up-regulation of GAP-43 in the ventral cochlear nucleus. Hear Res 255:33-43.
Kuenzel T, Borst JG, van der Heijden M (2011) Factors controlling the input-output relationship of spherical bushy cells in the gerbil cochlear nucleus. J Neurosci 31:4260-4273.
Lauer AM, Dooling RJ (2007) Evidence of Hyperacusis in Canaries with Permanent Hereditary High-Frequency Hearing Loss. Semin Hear 28.
Lecluyse W, Tan CM, McFerran D, Meddis R (2013) Acquisition of auditory profiles for good and impaired hearing. Int J Audiol 52:596-605.
Li S, Choi V, Tzounopoulos T (2013) Pathogenic plasticity of Kv7.2/3 channel activity is essential for the induction of tinnitus. Proc Natl Acad Sci U S A 110:9980-9985.
Li S, Kalappa BI, Tzounopoulos T (2015) Noise-induced plasticity of KCNQ2/3 and HCN channels underlies vulnerability and resilience to tinnitus. eLife 4.
Liberman MC (1993) Central projections of auditory nerve fibers of differing spontaneous rate, II: Posteroventral and dorsal cochlear nuclei. J Comp Neurol 327:17-36.
Lomakin O, Davis KA (2008) On the role of the wideband inhibitor in the dorsal cochlear nucleus: a computational modeling study. J Assoc Res Otolaryngol 9:506-520.

Lu YG, Tang ZQ, Ye ZY, Wang HT, Huang YN, Zhou KQ, Zhang M, Xu TL, Chen L (2009) Salicylate, an aspirin metabolite, specifically inhibits the current mediated by glycine receptors containing alpha1-subunits. Br J Pharmacol 157:1514-1522.
MacGregor RJ (1987) Neural and Brain Modelling.
Magee JC, Johnston D (1997) A synaptically controlled, associative signal for Hebbian plasticity in hippocampal neurons. Science 275:209-213.
Marks KL, Martel DT, Wu C, Basura GJ, Roberts LE, Schvartz-Leyzac KC, Shore SE (2018) Auditory-somatosensory bimodal stimulation desynchronizes brain circuitry to reduce tinnitus in guinea pigs and humans. Sci Transl Med 10.
Martel DT, Pardo-Garcia TR, Shore SE (2019) Dorsal Cochlear Nucleus Fusiform-cell Plasticity is Altered in Salicylate-induced Tinnitus. Neuroscience 407:170-181.
May BJ (2000) Role of the dorsal cochlear nucleus in the sound localization behavior of cats. Hear Res 148:74-87.
McLachlan GJ, Chang SU (2004) Mixture modelling for cluster analysis. Stat Methods Med Res 13:347-361.
Meddis R (2006) Auditory-nerve first-spike latency and auditory absolute threshold: a computer model. J Acoust Soc Am 119:406-417.
Meddis R, Lecluyse W, Clark NR, Jurgens T, Tan CM, Panda MR, Brown GJ (2013) A computer model of the auditory periphery and its application to the study of hearing. Adv Exp Med Biol 787:11-19; discussion 19-20.
Melcher JR, Kiang NY (1996) Generators of the brainstem auditory evoked potential in cat. III: Identified cell populations. Hear Res 93:52-71.
Melcher JR, Guinan JJ, Jr., Knudson IM, Kiang NY (1996) Generators of the brainstem auditory evoked potential in cat. II. Correlating lesion sites with waveform changes. Hear Res 93:28-51.
Middleton JW, Kiritani T, Pedersen C, Turner JG, Shepherd GM, Tzounopoulos T (2011) Mice with behavioral evidence of tinnitus exhibit dorsal cochlear nucleus hyperactivity because of decreased GABAergic inhibition. Proc Natl Acad Sci U S A 108:7601-7606.
Mugnaini E, Warr WB, Osen KK (1980) Distribution and light microscopic features of granule cells in the cochlear nuclei of cat, rat, and mouse. J Comp Neurol 191:581-606.
Muller M, Klinke R, Arnold W, Oestreicher E (2003) Auditory nerve fibre responses to salicylate revisited. Hear Res 183:37-43.
Nelken I, Young ED (1994) Two separate inhibitory mechanisms shape the responses of dorsal cochlear nucleus type IV units to narrowband and wideband stimuli. J Neurophysiol 71:2446-2462.
Nerlich J, Kuenzel T, Keine C, Korenic A, Rubsamen R, Milenkovic I (2014) Dynamic fidelity control to the central auditory system: synergistic glycine/GABAergic inhibition in the cochlear nucleus. J Neurosci 34:11604-11620.
Norena AJ, Eggermont JJ (2003) Changes in spontaneous neural activity immediately after an acoustic trauma: implications for neural correlates of tinnitus. Hear Res 183:137-153.
Norena AJ, Moffat G, Blanc JL, Pezard L, Cazals Y (2010) Neural changes in the auditory cortex of awake guinea pigs after two tinnitus inducers: salicylate and acoustic trauma. Neuroscience 166:1194-1209.
Oertel D, Young ED (2004) What's a cerebellar circuit doing in the auditory system? Trends Neurosci 27:104-110.
Oertel D, Shatadal S, Cao XJ (2008) In the ventral cochlear nucleus Kv1.1 and subunits of HCN1 are colocalized at surfaces of neurons that have low-voltage-activated and hyperpolarization-activated conductances. Neuroscience 154:77-86.
Osen KK (1969) Cytoarchitecture of the cochlear nuclei in the cat. J Comp Neurol 136:453-484.

Osen KK, Storm-Mathisen J, Ottersen OP, Dihle B (1995) Glutamate is concentrated in and released from parallel fiber terminals in the dorsal cochlear nucleus: a quantitative immunocytochemical analysis in guinea pig. J Comp Neurol 357:482-500.
Park TJ, Klug A, Holinstat M, Grothe B (2004) Interaural level difference processing in the lateral superior olive and the inferior colliculus. J Neurophysiol 92:289-301.
Pfeiffer RR (1966) Classification of response patterns of spike discharges for units in the cochlear nucleus: tone-burst stimulation. Exp Brain Res 1:220-235.
Pilati N, Large C, Forsythe ID, Hamann M (2012) Acoustic over-exposure triggers burst firing in dorsal cochlear nucleus fusiform cells. Hear Res 283:98-106.
Pressnitzer D, Meddis R, Delahaye R, Winter IM (2001) Physiological correlates of comodulation masking release in the mammalian ventral cochlear nucleus. J Neurosci 21:6377-6386.
Radziwon K, Holfoth D, Lindner J, Kaier-Green Z, Bowler R, Urban M, Salvi R (2017) Salicylate-induced hyperacusis in rats: Dose- and frequency-dependent effects. Hear Res 350:133-138.
Ralli M, Lobarinas E, Fetoni AR, Stolzberg D, Paludetti G, Salvi R (2010) Comparison of salicylate- and quinine-induced tinnitus in rats: development, time course, and evaluation of audiologic correlates. Otol Neurotol 31:823-831.
Rhode WS (1999) Vertical cell responses to sound in cat dorsal cochlear nucleus. J Neurophysiol 82:1019-1032.
Roberts LE, Moffat G, Bosnyak DJ (2006) Residual inhibition functions in relation to tinnitus spectra and auditory threshold shift. Acta Otolaryngol Suppl:27-33.
Roberts LE, Moffat G, Baumann M, Ward LM, Bosnyak DJ (2008) Residual inhibition functions overlap tinnitus spectra and the region of auditory threshold shift. J Assoc Res Otolaryngol 9:417-435.
Roberts LE, Eggermont JJ, Caspary DM, Shore SE, Melcher JR, Kaltenbach JA (2010) Ringing ears: the neuroscience of tinnitus. J Neurosci 30:14972-14979.
Rubio ME, Fukazawa Y, Kamasawa N, Clarkson C, Molnar E, Shigemoto R (2014) Target- and input-dependent organization of AMPA and NMDA receptors in synaptic connections of the cochlear nucleus. J Comp Neurol 522:4023-4042.
Ruttiger L, Ciuffani J, Zenner HP, Knipper M (2003) A behavioral paradigm to judge acute sodium salicylate-induced sound experience in rats: a new approach for an animal model on tinnitus. Hear Res 180:39-50.
Ryugo DK, Haenggeli CA, Doucet JR (2003) Multimodal inputs to the granule cell domain of the cochlear nucleus. Exp Brain Res 153:477-485.
Salloum RH, Yurosko C, Santiago L, Sandridge SA, Kaltenbach JA (2014) Induction of enhanced acoustic startle response by noise exposure: dependence on exposure conditions and testing parameters and possible relevance to hyperacusis. PLoS One 9:e111747.
Schaette R, McAlpine D (2011) Tinnitus with a normal audiogram: physiological evidence for hidden hearing loss and computational model. J Neurosci 31:13452-13457.
Schecklmann M, Landgrebe M, Langguth B, Group TRIDS (2014) Phenotypic characteristics of hyperacusis in tinnitus. PLoS One 9:e86944.
Schrode KM, Muniak MA, Kim YH, Lauer AM (2018) Central Compensation in Auditory Brainstem after Damaging Noise Exposure. eNeuro 5.
Sheldrake J, Diehl PU, Schaette R (2015) Audiometric characteristics of hyperacusis patients. Front Neurol 6:105.
Sheppard A, Hayes SH, Chen GD, Ralli M, Salvi R (2014) Review of salicylate-induced hearing loss, neurotoxicity, tinnitus and neuropathophysiology. Acta Otorhinolaryngol Ital 34:79-93.
Shofner WP, Young ED (1985) Excitatory/inhibitory response types in the cochlear nucleus: relationships to discharge patterns and responses to electrical stimulation of the auditory nerve. J Neurophysiol 54:917-939.

Shore SE, Wu C (2019) Mechanisms of Noise-Induced Tinnitus: Insights from Cellular Studies. Neuron 103:8-20.
Shore SE, El Kashlan H, Lu J (2003) Effects of trigeminal ganglion stimulation on unit activity of ventral cochlear nucleus neurons. Neuroscience 119:1085-1101.
Shore SE, Roberts LE, Langguth B (2016a) Maladaptive plasticity in tinnitus - triggers, mechanisms and treatment. Nat Rev Neurol 12:150-160.
Shore SE, Roberts LE, Langguth B (2016b) Maladaptive plasticity in tinnitus--triggers, mechanisms and treatment. Nat Rev Neurol 12:150-160.
Shore SE, Koehler S, Oldakowski M, Hughes LF, Syed S (2008) Dorsal cochlear nucleus responses to somatosensory stimulation are enhanced after noise-induced hearing loss. Eur J Neurosci 27:155-168.
Singer W (1999) Neuronal synchrony: a versatile code for the definition of relations? Neuron 24:49-65, 111-125.
Singla S, Dempsey C, Warren R, Enikolopov AG, Sawtell NB (2017) A cerebellum-like circuit in the auditory system cancels responses to self-generated sounds. Nat Neurosci 20:943-950.
Spirou GA, Brownell WE, Zidanic M (1990) Recordings from cat trapezoid body and HRP labeling of globular bushy cell axons. J Neurophysiol 63:1169-1190.
Stabler SE, Palmer AR, Winter IM (1996) Temporal and mean rate discharge patterns of single units in the dorsal cochlear nucleus of the anesthetized guinea pig. J Neurophysiol 76:1667-1688.
Stefanescu RA, Shore SE (2015) NMDA Receptors Mediate Stimulus-Timing-Dependent Plasticity and Neural Synchrony in the Dorsal Cochlear Nucleus. Frontiers in neural circuits 9:75.
Stefanescu RA, Koehler SD, Shore SE (2015) Stimulus-timing-dependent modifications of rate-level functions in animals with and without tinnitus. J Neurophysiol 113:956-970.
Stolzberg D, Salvi RJ, Allman BL (2012) Salicylate toxicity model of tinnitus. Front Syst Neurosci 6:28.
Stolzberg D, Hayes SH, Kashanian N, Radziwon K, Salvi RJ, Allman BL (2013) A novel behavioral assay for the assessment of acute tinnitus in rats optimized for simultaneous recording of oscillatory neural activity. J Neurosci Methods 219:224-232.
Sumner CJ, Tucci DL, Shore SE (2005) Responses of ventral cochlear nucleus neurons to contralateral sound after conductive hearing loss. J Neurophysiol 94:4234-4243.
Sumner CJ, Lopez-Poveda EA, O'Mard LP, Meddis R (2002) A revised model of the inner-hair cell and auditory-nerve complex. J Acoust Soc Am 111:2178-2188.
Sumner CJ, O'Mard LP, Lopez-Poveda EA, Meddis R (2003) A nonlinear filter-bank model of the guinea-pig cochlear nerve: rate responses. J Acoust Soc Am 113:3264-3274.
Sutherland DP, Masterton RB, Glendenning KK (1998a) Role of acoustic striae in hearing: reflexive responses to elevated sound-sources. Behavioural brain research 97:1-12.
Sutherland DP, Glendenning KK, Masterton RB (1998b) Role of acoustic striae in hearing: discrimination of sound-source elevation. Hear Res 120:86-108.
Tan J, Ruttiger L, Panford-Walsh R, Singer W, Schulze H, Kilian SB, Hadjab S, Zimmermann U, Kopschall I, Rohbock K, Knipper M (2007) Tinnitus behavior and hearing function correlate with the reciprocal expression patterns of BDNF and Arg3.1/arc in auditory neurons following acoustic trauma. Neuroscience 145:715-726.
Tao HW, Zhang LI, Engert F, Poo M (2001) Emergence of input specificity of ltp during development of retinotectal connections in vivo. Neuron 31:569-580.
Tsuji J, Liberman MC (1997) Intracellular labeling of auditory nerve fibers in guinea pig: central and peripheral projections. J Comp Neurol 381:188-202.
Turner JG, Parrish J (2008) Gap detection methods for assessing salicylate-induced tinnitus and hyperacusis in rats. American journal of audiology 17:S185-192.

Turner JG, Brozoski TJ, Bauer CA, Parrish JL, Myers K, Hughes LF, Caspary DM (2006) Gap detection deficits in rats with tinnitus: a potential novel screening tool. Behav Neurosci 120:188-195.
Tyler RS, Pienkowski M, Roncancio ER, Jun HJ, Brozoski T, Dauman N, Dauman N, Andersson G, Keiner AJ, Cacace AT, Martin N, Moore BC (2014) A review of hyperacusis and future directions: part I. Definitions and manifestations. American journal of audiology 23:402-419.
Tzounopoulos T, Kim Y, Oertel D, Trussell LO (2004) Cell-specific, spike timing-dependent plasticities in the dorsal cochlear nucleus. Nat Neurosci 7:719-725.
Uhlhaas PJ, Singer W (2006) Neural synchrony in brain disorders: relevance for cognitive dysfunctions and pathophysiology. Neuron 52:155-168.
Uhlhaas PJ, Pipa G, Lima B, Melloni L, Neuenschwander S, Nikolic D, Singer W (2009) Neural synchrony in cortical networks: history, concept and current status. Front Integr Neurosci 3:17.
Vogler DP, Robertson D, Mulders WH (2011) Hyperactivity in the ventral cochlear nucleus after cochlear trauma. J Neurosci 31:6639-6645.
Voigt HF, Young ED (1990) Cross-correlation analysis of inhibitory interactions in dorsal cochlear nucleus. J Neurophysiol 64:1590-1610.
Wagner E, Florentine M, Buus S, McCormack J (2004) Spectral loudness summation and simple reaction time. J Acoust Soc Am 116:1681-1686.
Wang H, Brozoski TJ, Turner JG, Ling L, Parrish JL, Hughes LF, Caspary DM (2009) Plasticity at glycinergic synapses in dorsal cochlear nucleus of rats with behavioral evidence of tinnitus. Neuroscience 164:747-759.
Wei L, Ding D, Sun W, Xu-Friedman MA, Salvi R (2010) Effects of sodium salicylate on spontaneous and evoked spike rate in the dorsal cochlear nucleus. Hear Res 267:54-60.
Wickesberg RE, Oertel D (1990) Delayed, frequency-specific inhibition in the cochlear nuclei of mice: a mechanism for monaural echo suppression. J Neurosci 10:1762-1768.
Winter IM, Palmer AR (1990a) Responses of single units in the anteroventral cochlear nucleus of the guinea pig. Hear Res 44:161-178.
Winter IM, Palmer AR (1990b) Temporal responses of primarylike anteroventral cochlear nucleus units to the steady-state vowel /i. J Acoust Soc Am 88:1437-1441.
Winter IM, Palmer AR (1995) Level dependence of cochlear nucleus onset unit responses and facilitation by second tones or broadband noise. J Neurophysiol 73:141-159.
Womelsdorf T, Schoffelen JM, Oostenveld R, Singer W, Desimone R, Engel AK, Fries P (2007) Modulation of neuronal interactions through neuronal synchronization. Science 316:1609-1612.
Wu C, Shore SE (2018) Multisensory activation of ventral cochlear nucleus D-stellate cells modulates dorsal cochlear nucleus principal cell spatial coding. J Physiol 596:4537-4548.
Wu C, Martel DT, Shore SE (2015) Transcutaneous induction of stimulus-timing-dependent plasticity in dorsal cochlear nucleus. Front Syst Neurosci.
Wu C, Martel DT, Shore SE (2016) Increased Synchrony and Bursting of Dorsal Cochlear Nucleus Fusiform Cells Correlate with Tinnitus. J Neurosci 36:2068-2073.
Xie R, Manis PB (2013) Target-specific IPSC kinetics promote temporal processing in auditory parallel pathways. J Neurosci 33:1598-1614.
Yang G, Lobarinas E, Zhang L, Turner J, Stolzberg D, Salvi R, Sun W (2007) Salicylate induced tinnitus: behavioral measures and neural activity in auditory cortex of awake rats. Hear Res 226:244-253.
Yang S, Weiner BD, Zhang LS, Cho SJ, Bao S (2011) Homeostatic plasticity drives tinnitus perception in an animal model. Proc Natl Acad Sci U S A 108:14974-14979.
Young ED, Voigt HF (1982) Response properties of type II and type III units in dorsal cochlear nucleus. Hear Res 6:153-169.

Zeng C, Nannapaneni N, Zhou J, Hughes LF, Shore S (2009) Cochlear damage changes the distribution of vesicular glutamate transporters associated with auditory and nonauditory inputs to the cochlear nucleus. J Neurosci 29:4210-4217.
Zeng FG (2013) An active loudness model suggesting tinnitus as increased central noise and hyperacusis as increased nonlinear gain. Hear Res 295:172-179.
Zhang C, Flowers E, Li JX, Wang Q, Sun W (2014) Loudness perception affected by high doses of salicylate--a behavioral model of hyperacusis. Behavioural brain research 271:16-22.
Zhou J, Shore S (2004) Projections from the trigeminal nuclear complex to the cochlear nuclei: a retrograde and anterograde tracing study in the guinea pig. J Neurosci Res 78:901-907.
Zhou J, Shore S (2006) Convergence of spinal trigeminal and cochlear nucleus projections in the inferior colliculus of the guinea pig. J Comp Neurol 495:100-112.
Zhou J, Nannapaneni N, Shore S (2007) Vessicular glutamate transporters 1 and 2 are differentially associated with auditory nerve and spinal trigeminal inputs to the cochlear nucleus. J Comp Neurol 500:777-787.